UNIVERSIDADE DA BEIRA INTERIOR
Ciências da Saúde

Novas abordagens terapêuticas para regeneração óssea

Kevin Domingos de Sá

Dissertação para obtenção do Grau de Mestre em
Ciências Biomédicas
(2º ciclo de estudos)

Orientador: Professor Doutor Ilídio Joaquim Sobreira Correia
Co-orientadores: Mestre Sónia Alexandra Pereira Miguel
Mestre Tiago Ruivo Correia

Covilhã, junho de 2016

List of publications

Article published in a peer reviewed international journal:

- Fradique, R., Correia, T. R., Miguel, S. P., *de Sá, K. D.*, Figueira, D. R., Mendonça, A. G., & Correia, I. J. (2016). Production of new 3D scaffolds for bone tissue regeneration by rapid prototyping. *Journal of Materials Science: Materials in Medicine*, *27*(4), 1-14. doi: 10.1007/s10856-016-5681-x.

- Correia, T. R., Figueira, D. R., *de Sá, K. D.*, Miguel, S. P., Fradique, R., Mendonça, A. G., & Correia, I. J. (2016). 3D printed scaffolds with bactericidal activity aimed for bone tissue regeneration. International Journal of Biological Macromolecules. In press.

"When the aerials are down, and your spirit is covered with snows of cynicism and the ice of pessimism, then you are grown old, even at 20, but as long as your aerials are up, to catch waves of optimism, there is hope you may die young at 80."

Samuel Ullman

Para os meus pais, com amor.

Acknowledgments

Firstly, I would like to thank to my supervisor professor Ilídio Correia for the opportunity to develop the theme of my master's thesis with him. For all the dedication and time spent in carrying out the whole of this project. I also thank him for the confidence deposited on me and for the opportunities he provided me during this year.

To professor Abílio Silva, for all availability to perform the mechanical characterization of the scaffolds.

To my co-supervisors and friends Sónia and Tiago, for the lunches, soccer games, daily help, and for the acquisition of the scanning electron microscopic images.

To my work group, in special to Elisabete and Marco, for all the patience and good vibes.

To my best friend and little fellow in life, Daniela. Thank you for always being on my side, for all the love, confidence and support. Thank you for everything, my darling. *Now, it's time that we began* ♪**.**

Finally, to my extraordinary parents, Rosa and António. A very special word of recognition for them, for all the love, patience and support who gave me during all these years.

Resumo

A capacidade limitada que o osso apresenta para reparar os defeitos críticos na sua totalidade requer o desenvolvimento de novos implantes capazes de melhorar o processo de recuperação. Neste contexto, têm sido desenvolvidas novas abordagens terapêuticas de forma a promover o processo de regeneração óssea, assim como evitar o surgimento de diferentes problemas associadas às terapias convencionais. Uma destas abordagens envolve o desenvolvimento de matrizes tridimensionais também designadas de *scaffolds*, que atuam como suportes temporários e que promovem a adesão e proliferação celular fornecendo ainda suporte mecânico durante o processo de regeneração óssea. Neste estudo desenvolveram-se *scaffolds* híbridos compostos por Tricalcio Fosfato/Ácido Alginico com recurso a prototipagem rápida (Fab@Home). Posteriormente, as superfícies destas estruturas foram funcionalizadas com membranas nanofibrosas produzidas pela técnica de electrofiação. Nestes revestimentos, compostos por Policaprolactona e Gelatina, foram ainda incorporados dois agentes antimicrobianos diferentes, nanoparticulas de Prata e Ácido Salicílico. Os resultados obtidos revelaram que os *scaffolds* produzidos apresentaram propriedades mecânicas, capacidade de absorção de água, porosidade, biodegradabilidade e biomineralização, compatíveis com a sua aplicação na área de engenharia de tecidos. Além disso, a presença da malha nanofibrosa na superfície do *scaffolds* melhorou a adesão e proliferação de células eucariótcas em contacto com estas estruturas tridimensionais. Por outro lado, a funcionalização da superfície dos *scaffolds* permitiu evitar a formação de biofilmes na superfície dos *scaffolds*, durante pelo menos 5 dias. Estes dados experimentais evidenciam o grande potencial destas estruturas para aplicação na regeneração do tecido ósseo.

Palavras-Chave

Ácido Salicílico; Atividade Bactericida; Electrofiação; Nanopartículas de Prata; Prototipagem Rápida; Regeneração Óssea;

Resumo alargado

O osso é um tecido altamente dinâmico e vascularizado responsável por conferir suporte ao corpo humano. Além disso, é responsável por permitir a locomoção do corpo atuando como escudo protetor dos principais órgãos vitais. A sua estrutura é formada por matriz orgânica (maioritariamente colagénio), matriz inorgânica (hidroxiapatita), células (osteoblastos, osteócitos e osteoclastos) e água. Apesar da elevada capacidade de auto-regeneração deste tecido, esta não é suficiente para reparar defeitos críticos que surgem com o envelhecimento, doenças ou traumas. Atualmente, o tratamento destes defeitos ósseos pode ser realizado através de autoenxertos, aloenxertos ou xenoenxertos. No entanto, a disponibilidade limitada, a frequente ocorrência de infeções e rejeições imunológicas por parte do hospedeiro podem comprometer o sucesso destas alternativas.

Neste contexto, a engenharia de tecidos tem vindo a desenvolver novas abordagens de forma a promover o processo de regeneração óssea. A engenharia de tecidos é um ramo interdisciplinar que aplica os princípios da biologia e engenharia, visando o desenvolvimento de substitutos biológicos que restaurem, mantenham ou melhorem as funcionalidades de tecidos humanos que tenham sido lesados ou comprometidos. Desta forma, têm-se desenvolvido matrizes tridimensionais (3D), também designadas por *scaffolds*, as quais atuam como suportes temporários no processo de formação do novo tecido ósseo. Além disso, a sua superfície deve ser capaz de mimetizar a matriz extracelular do local de implantação de forma a promover a adesão e proliferação celular. Na atualidade os *scaffolds* são produzidos através de uma grande variedade de técnicas, onde são usados diferentes materiais, nomeadamente polímeros, cerâmicas e metais.

O presente estudo descreve a produção e caracterização das propriedades químicas, mecânicas e biológicas de *scaffolds* 3D híbridos compostos por Tricalcio Fosfato/Ácido Alginico (TCP/AA). Estas estruturas foram produzidas por prototipagem rápida usando uma impressora 3D (Fab@Home), sendo posteriormente revestidas com dois tipos diferentes de matrizes nanofibrosas obtidas por eletrofiação de forma a melhorar o seu comportamento biológico. Estes revestimentos, tinham na sua composição Policaprolactona (PCL) e Gelatina (GEL). Por outro lado, de forma a conferir propriedades antimicrobianas aos *scaffolds*, estes foram funcionalizados com dois agentes antimicrobianos diferentes, nanopartículas de Prata (AgNPs) e Ácido Salicílico (SA).

As propriedades físico-químicas dos diferentes *scaffolds* produzidos (TCP/AA, TCP/AA_AgNPs e TCP/AA_SA) foram caracterizadas por Espectroscopia de Infravermelho por Transformada de Fourier, Espectroscopia de Energia Dispersiva e Microscopia Eletrónica de Varrimento. Os resultados revelaram que nenhum dos componentes sofreu qualquer tipo de alteração química

durante o processo de manufatura dos *scaffolds*. Além disso foi ainda possível observar a presença de uma densa malha nanofibrosa na superfície dos *scaffolds* TCP/AA_AgNPs e TCP/AA_SA. Este revestimento melhorou a aptidão dos *scaffolds* para suportar adesão e proliferação celular, em comparação com o grupo sem revestimento (TCP/AA). A porosidade e resistência mecânica apresentadas por todas as estruturas produzidas foram semelhantes às do osso trabecular. Os ensaios de citotoxicidade realizados *in vitro* revelaram que todas as formulações são biocompatíveis durante pelo menos 7 dias. Por outro lado, as imagens de microscopia eletrónica de varrimento revelaram que as formulações previamente revestidas (TCP/AA_AgNPs e TCP/AA_SA) apresentaram um maior número de células aderidas na sua superfície. Tal deve-se sobretudo às propriedades bioadesivas que o revestimento de nanofibras conferiu à superfície dos *scaffolds*. Por fim, a capacidade antimicrobiana dos materiais foi analisada através do método de *Kirby-Bauer*. Os resultados obtidos revelaram que os *scaffolds* TCP/AA_AgNPs e TCP/AA_SA são capazes de inibir o crescimento bacteriano, um facto constatado através da formação de halos inibitórios após incubação destes *scaffolds* com *S. Aureus*. A formação de biofilmes na superfície dos materiais, foi ainda caracterizada por microscopia eletrónica de varrimento sendo que os resultados confirmaram as propriedades antimicrobianas dos *scaffolds*.

Em suma, os resultados obtidos no presente estudo revelaram que os *scaffolds* 3D produzidos apresentam propriedades químicas, biológicas e mecânicas, que são compatíveis com a sua aplicação futura na regeneração de tecido ósseo.

Abstract

Bone limited capacity to fully repair large defects demands the development of new implants that are able to improve the healing process. In this context, new approaches for promoting bone regeneration process and also to avoid side effects associated with the therapeutics in use, are currently being studied. Herein 3D tricalcium phosphate/alginic acid scaffolds were produced using a Fab@Home and then coated with an electrospun mesh (composed by polycaprolactone and gelatin) loaded with two different antibacterial agents (silver nanoparticles and salicylic acid). The obtained results show that the produced scaffolds presented mechanical properties, swelling, macro/microporosity, biodegradation and biomineralization capacity, that are compatible with their application for bone tissue engineering purposes. Moreover, the presence of a nanofibrous mesh at the surface of produced 3D constructs enhanced cellular adhesion/proliferation and also avoided biofilm formation at scaffolds' surface, for at least 5 days. Such results emphasize that the 3D hybrid scaffolds produced herein have the required properties for being used in the proposed biomedical application.

Keywords

Bactericidal activity; Bone regeneration; Electrospinning; Rapid prototyping; Salicylic acid; Silver nanoparticles.

Contents

List of figures

Acronyms

3D	Three-Dimensional
AA	Alginic Acid
AgNPs	Silver Nanoparticles
ATR-FTIR	Attenuated Total Reflectance-Fourier Transform Infrared Spectroscopy
BMP	Bone Morphogenic Proteins
ß -TCP	ß -Tricalcium Phosphate
CAD	Computer-Aided-Design
CFU	Colony Forming Units
COX	Cyclooxygenase
DLS	Dynamic Light Scattering
DMEM-F12	Dulbecco's Modified Eagle's Medium
DNA	Deoxyribonucleic Acid
ECM	Extracellular Matrix
EDS	Energy Dispersive Spectroscopic
EDTA	Ethylenediaminetetraacetic Acid
ES	Electrospinning
EtOH	Ethanol
FBS	Fetal Bovine Serum
GEL	Gelatin
GPa	Gigapascal
HA	Hydroxyapatite
HOB	Human Osteoblast
IGF-1	Insulin Growth Factor-1
IGF-2	Insulin Growth Factor-2
IL-6	Interleukin-6
M-CSF	Macrophage Colony-Stimulating Factor
MPa	Megapascal
MTT	3-(4,5-dimethylthiazol-2-yl)-2,5-diphenyltetrazolium bromide
NCP	Noncollagenous Proteins
PBS	Phosphate-Buffered Saline Solution
PCL	Polycaprolactone
PTH	Parathyroid Hormone
PVP	Polyvinylpyrrolidone
RANK	Receptor Activator of Nuclear
RANKL	Receptor Activator of Nuclear Ligand
RGD	Arginine-Glycine-Aspartic Acid

RP	Rapid Prototyping
RT	Room Temperature
SA	Salicylic Acid
SBF	Simulated Body Fluid
SEM	Scanning Electron Microscopy
TCP	Tricalcium Phosphate
TE	Tissue Engineering
TEM	Transmission Electron Microscopy
TFE	Trifluoroethanol
TGF- ß	Transforming Growth Factors-ß
Ti	Titanium
TNF–α	Tumor Necrosis Factor-α
UV	Ultraviolet

Chapter I - Introduction

1. Introduction

1.1. Bone Tissue

Bone is a specialized and dynamic connective tissue that serves as the main component of the human skeleton [1-3]. Bone functions include locomotion, protection of the internal organs (brain, spinal cord, heart and lungs), hematopoiesis and mechanical support of diaphragm [3, 4]. Furthermore, it also acts as a reservoir of minerals, namely calcium and phosphorus, and promotes the attachment for muscles, ligaments and tendons [4, 5]. Bone tissue is in constant remodeling in order to be able to support biomechanical forces and remove old and micro damaged bone [3, 6].

Bone tissue possesses a complex architecture and its cells (osteoblasts, osteocytes and osteoclasts) are involved in bone maintenance and remodeling [1, 3, 4]. These cells are embedded in the bone extracellular matrix (ECM), that is composed by a mineral and an organic phase [3, 4, 7]. A more detailed description of the structural organization of the human bone is given in the following sections.

1.2. Bone Anatomy

According to their shape, bones can be classified as long, short, flat or irregular [8]. Long bones, such as clavicles, femurs and tibiae, present a cylindrical shape and great mechanical strength. Bones can be divided in three physiologic sections: the diaphysis, that composes the bulk bone, the epiphysis, located at the ends of the bone and the epiphyseal plate, located where new bone is formed during growth [8, 9]. On the other hand, short bones, just as patellae, sesamoid bones, carpal and tarsal bones, have a cubic or spherical geometry. Flat bones (e.g. mandible, skull, sternum and ribs) present thin, curved or flat shapes whereas irregular bones (e.g. vertebrae, coccyx, scrum and hyoid bone) have complex shapes that are not included in the above mentioned ones [8].

The schematic structure of the internal structure and organization of bone tissue is presented in figure 1. Morphologically, bone tissue is classified as cortical or as cancellous [4-6]. Cortical bone is almost solid with only 10% of porosity and account's for 80% of the mass of a mature human skeleton [4, 10]. It has high mechanical strength, since it consists of closely packed cortical osteons, called Haversian systems, that form a solid and consistent mass [1, 5]. The Haversian systems have a central canal, known as Haversian canal, that is surrounded by concentric rings of matrix [5]. The outer surface of cortical bone is covered by a bi-layered connective tissue membrane, known as the periosteum [5, 11]. In turn, the outer layer of the periosteum, known as fibrous layer, is made of irregular collagenous tissue containing blood vessels and nerves, while the inner layer is composed by a single layer of bone cells [12]. These features facilitate the

fixation of tendons or ligaments to the bone. In contrast, cancellous bone is highly porous (50-90%) and has a compressive strength almost 20 times inferior to that displayed by cortical bone. It is strongly associated with metabolic activities, since its pores are interconnected and filled with bone marrow [11]. Cancellous bone is arranged in a sponge-like form, with a honeycomb of branching plates and rods of various sizes called trabeculae [5].

Cortical bone is present in the diaphysis of the long bones. Flat, short and irregular bone usually present a cancellous interior filled with marrow surrounded by two layers of cortical bone [8].

Microscopically, bone can be further classified as woven or lamellar, according to the collagen fibers orientation [5]. Cortical and trabecular bone are usually formed by a lamellar pattern, in which collagen fibrils are laid down in randomly orientations [6, 11]. In contrast, woven bone consists of collagen fibers lying parallel to each other. Due to that, woven bone is weaker than lamellar bone. Woven bone is, in fact, characteristic of embryonic and fetal development, but it is also found in the healthy adult skeleton at ligament and tendon insertions and under pathologic conditions (e.g. Paget's disease) [8].

The schematic structure of the internal structure and organization of bone tissue is presented in figure 1.

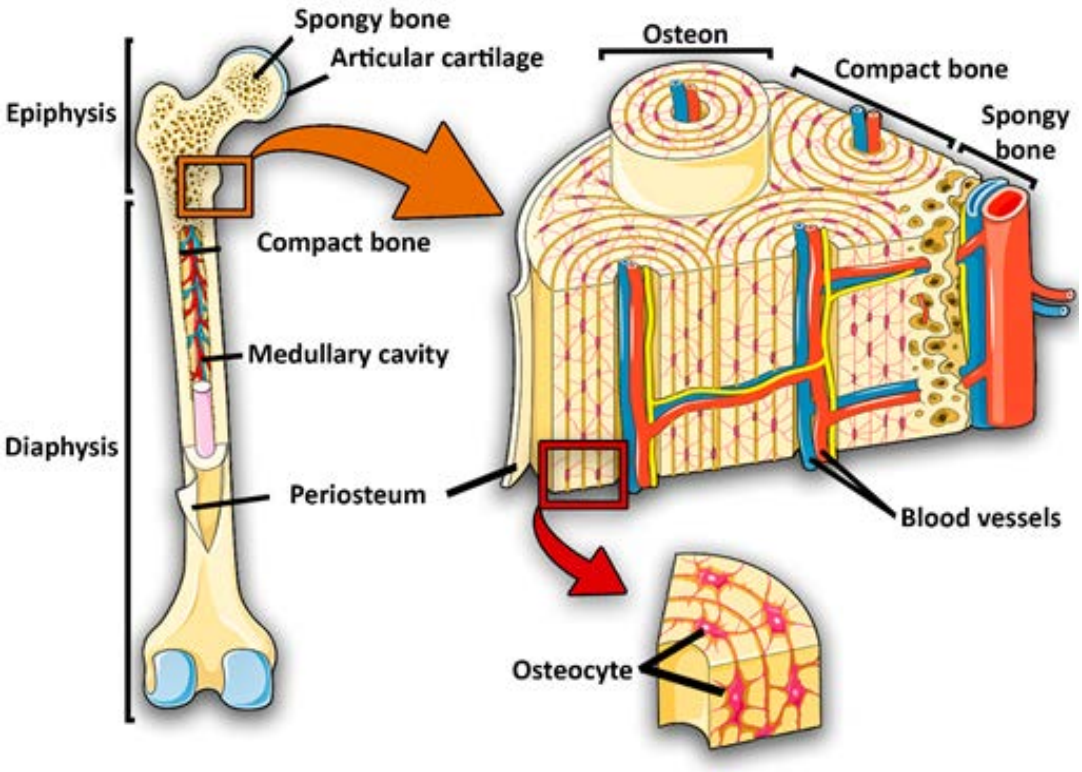

Figure 1. Schematic representation of the internal structure and organization of bone.

1.3. Bone histology

1.3.1. Bone matrix

Bone matrix is a composite of organic and mineral compounds displayed in a ratio of 35/65%, which together contribute to the strength and flexibility of the human skeleton [4, 13, 14]. The organic phase is composed of fibrillary proteins (mainly collagen type I), proteoglycans and a variety of noncollagenous proteins (NCP), whereas the mineral phase is mainly constituted by hydroxyapatite crystals [1, 4].

Collagen is the most abundant component of the organic bone matrix and is responsible for providing toughness to the bone matrix [4, 15-17]. In addition to collagen, bone matrix contains about 200 NCP that can be divided in two major groups [16, 18]. One group plays a structural and mechanical role and the other modulates the function of different bone cells by interacting with their cell-surface receptors, proteases, hormones and other biomolecules. The structural NCPs include fibronectin, osteocalcin, osteopontin, osteonectin, bone sialoprotein II, decorin and biglycan [1, 3, 4]. The second group of NCPs include transforming growth factors-ß (TGF-ß1, TGF-ß2, and TGF-ß3), insulin-like growth factors (IGFs), and bone morphogenic proteins (BMPs) [4, 16]. On the other hand, the mineral phase of bone matrix is mainly constituted by crystalline mineral salts in the form of hydroxyapatite. Although, tricalcium phosphate, calcium carbonate and fluoride derivatives are also found in this matrix. The mineral component of the bone provides tensile yield strength and also preforms important physiological functions related to the storage of ions [14, 15]. It is estimated that the bones contain 99% of the calcium, 85% of the phosphorus and 40-60% of the sodium and magnesium found in the human body [4, 15]. Physiological functions, like nerve conduction and muscle contraction depend on the ions present on this organic matrix[4].

The organic and mineral phases of bone matrix must be present in a balanced way [3-5, 13]. In fact, when the mineral component is diminished, the bone becomes more flexible due to the increase of collagen [5, 14]. Otherwise, if the collagen is absent, the bone becomes very brittle due to the high mineral fraction. Besides that, bone matrix composition can also suffer variations with age, namely an increase in mineralization degree and a decrease in bone collagen content [5].

1.3.2. Bone cells

Osteoblasts, osteocytes and osteoclasts play different functions in bone maintenance and remodeling processes (see figure 2 for further details) [3, 4, 9, 19, 20].

Osteoblasts cells are derived from mesenchymal stem cells (osteogenic cells), which are essentially located in bone marrow and periosteum [4, 7, 9, 21]. Osteoblast functions include the synthesis and organization of bone ECM, its subsequent mineralization and the downregulation of osteoclasts [3, 7]. Morphologically, they display a cuboidal shape and present enlarged organelles, such as nucleus, Golgi and endoplasmic reticulum apparatus [1, 3, 15]. Furthermore,

osteoblasts are highly dependent on anchorage and they maintain extensive cell–matrix and cell–cell interactions through a variety of trans-membranous proteins (integrins, connexins, cadherins) and receptors (cytokines, hormones, growth factors) in order to maintain their cellular functions and responsiveness to metabolic and mechanical stimuli [3, 4, 7]. The lifespan of osteoblast is about 8 weeks in humans [1]. It is noteworthy to stress that osteoblasts after being differentiated may have three fates: revert back to bone lining phenotype; differentiate into osteocytes or undergo apoptosis [3, 15].

Osteocytes are formed through the differentiation of osteoblasts and are the most abundant cell type in bone [5, 15, 20]. The primary function of osteocytes is to maintain the bone structure since they act as mechanosensors capable of transduce musculoskeletal stress signals [4, 9, 20]. In terms of morphology, these cells are smaller than osteoblasts and have lost many of their cytoplasmic organelles [15]. Moreover, they possess a higher number of filopodia, i.e. cytoplasmatic extensions, that form an extensive connecting syncytial network, which are used for exchange of nutrients or waste products [1, 7, 15]. In order to convert the mechanical stimuli into intracellular signal, some authors suggest that nitric oxide, Wnt and cadherin-mediated signaling pathways are activated by osteoclasts [20]. However, the precise mechanisms of stimulus and response remain unclear.

Osteoclasts derive from hematopoietic stem cells and are responsible to resorb fully mineralized bone [1, 3, 4]. During the motile state they migrate from the bone marrow to their resorptive site whereas in the resorptive phase they break down bone tissue in a process named bone resorption [4, 7, 22]. In each state the osteoclasts display morphological variations. Motile osteoclasts are flattened, non-polarized cells, that are characterized by the presence of membrane protrusions, called lamellipodia, and podosome complexes containing actin [3, 7, 15]. When they reach the resorptive site, osteoclasts become polarized, through cytoskeletal reorganization. This process leads to the formation of specific membrane domains, such as sealing zone, that separates the acidic resorptive environment from the rest of the cell, forming an organelle free area [1, 3, 5, 22]. During resorption, osteoclasts are dome-shaped and lack lamellipodia [15]. An activated osteoclast is able to resorb 200,000 μm^3/day of bone matrix [1] and they have an average lifespan of 15–20 days [1].

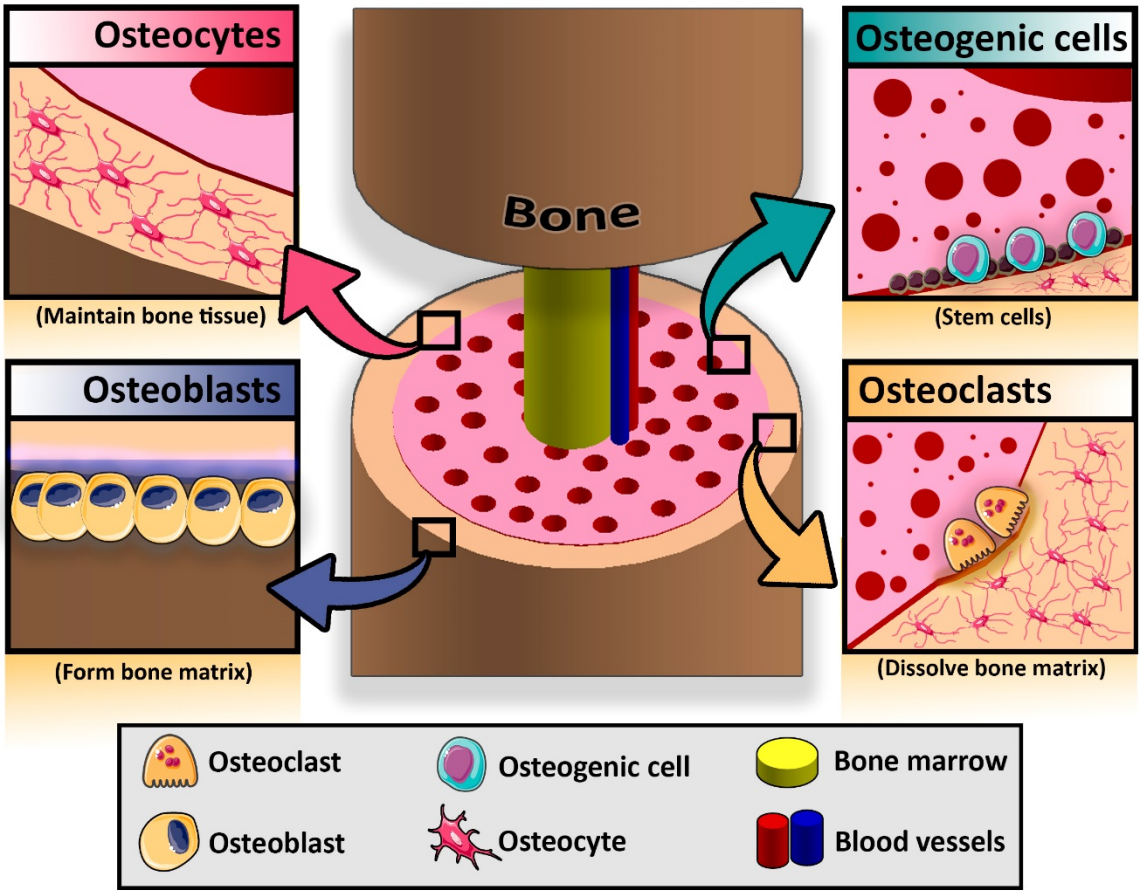

Figure 2. Schematic representation of the cells present in bone tissue. Osteoblasts, derived from osteogenic cells, are involved in bone formation; Osteocytes are responsible for the maintenance of integrity of bone tissue; Osteoclasts are involved in bone resorption.

1.3.3. Bone remodeling

Bone tissue is constantly being remodeled in order to maintain its strength and mineral homeostasis. The remodeling process consists in resorption of old bone and formation of new bone in order to prevent the accumulation of bone micro damages, and thus assure the integrity of the skeleton [4, 5, 23]. As can be observed in figure 3, there are four main phases in bone remodeling process (activation, resorption, reversal and formation stages) and the process takes about 3-6 months to be completed in humans [24]. Moreover, remodeling is not only required to replace dead or damaged tissue, but it also gives bone the capacity to adapt to changes in loading and to respond to nutritional and metabolic changes [1, 4, 24, 25].

- Activation phase

The first stage of bone remodeling involves the detection of an initiating remodeling signal, that can be a physical or a hormonal stimulus [20, 24]. In case of structural damage, insulin growth factor-I (IGF-I), tumor necrosis factor-α (TNF-α), parathyroid hormone (PTH) and interleukin-6 (IL-6) promote the activation of bone lining cells present on bone surface [7, 14, 23, 24]. At the same

time, the damage results in osteocyte apoptosis, decreased TGF-β levels and, as a consequence, the deletion of inhibitory osteoclastogenesis signals [7, 20]. Therefore, osteoclastogenesis process begins in bone marrow, and subsequently partially differentiated mononuclear preosteoclasts migrate through the blood stream and become attach to the bone matrix [24]. On the other hand, responding to osteoclastogenic stimulus, pre-osteoblasts secrete macrophage colony-stimulating factor (M-CSF), that induce the expression of Receptor Activator of Nuclear κB (RANK) by osteoclasts [7]. Receptor Activator of Nuclear κB ligand (RANKL)/RANK interaction triggers pre-osteoclasts fusion and differentiation toward mature osteoclasts [23, 24].

Another osteoclast activation signal can be induced by hormones. PTH is an endocrine remodeling signal produced to maintain calcium homeostasis. This hormone is secreted by the parathyroid glands in response to low serum calcium levels. When in contact with the bone tissue, PTH activates the PTH receptor, (a G-protein-coupled receptor, on the surface of osteoblasts) [7]. This binding activates protein kinase A, protein kinase C, and calcium intracellular signaling pathways in these cells and induces several transcriptional responses that produce/modulate the secretion of molecules that recruit osteoclast precursors, induce osteoclast differentiation and activation, processes that are crucial for bone resorption [14, 23].

- Resorption phase

The resorption phase, which has an average duration of 30–40 days, consists in the attachment of differentiated osteoclasts to depressions or resorptive bays, known as Howship lacunae, present in bone matrix [23, 24]. Osteoclast anchorage to bone surfaces occurs through anchoring proteins such as integrins (e.g. $\alpha_v\beta_3$) [14]. Subsequently, osteoclasts promote the bone demineralization process [24]. This process is performed in two steps: i) acidification of the bone matrix to dissolve its mineral component, and ii) release of lysosomal (e.g. cathepins K), and non-lysosomal (e.g. collagenase) enzymes, that are responsible for the degradation of the organic component of bone [14, 23]. When the cavity reaches a depth of about 60 µm from the surface in trabecular bone and about 100 µm in cortical bone, osteoclasts undergo to apoptosis [25]. This is a physiological consequence required to avoid an excessive bone resorption [24].

- Reversal phase

Reversal phase represents the transition from osteoclastic to osteoblastic activity and lasts approximately 9 days [7, 24]. At this stage, mononuclear cells of osteoblastic lineage remove the remaining undigested demineralized collagen present in the Howship lacunae and prepare the bone surface for the subsequent osteoblast-mediated bone formation [7, 23]. This phase is also characterized by the activation of factors that stimulate osteoblast precursors to proliferate, including IGF-2 and TGF-β [1, 23, 24].

- Formation phase

At this stage, differentiated osteoblasts synthesize new organic matrix and release vesicles that contain calcium, phosphate and enzymes that destroy the mineralization inhibitors, such as pyrophosphate or proteoglycans [1, 7, 23, 24]. The remodeling cycle is concluded when all reabsorbed bone is replaced.

At the end of the process, osteoblasts may enter in apoptosis, revert back to bone lining phenotype, or differentiate into osteocytes within the matrix [7, 25].

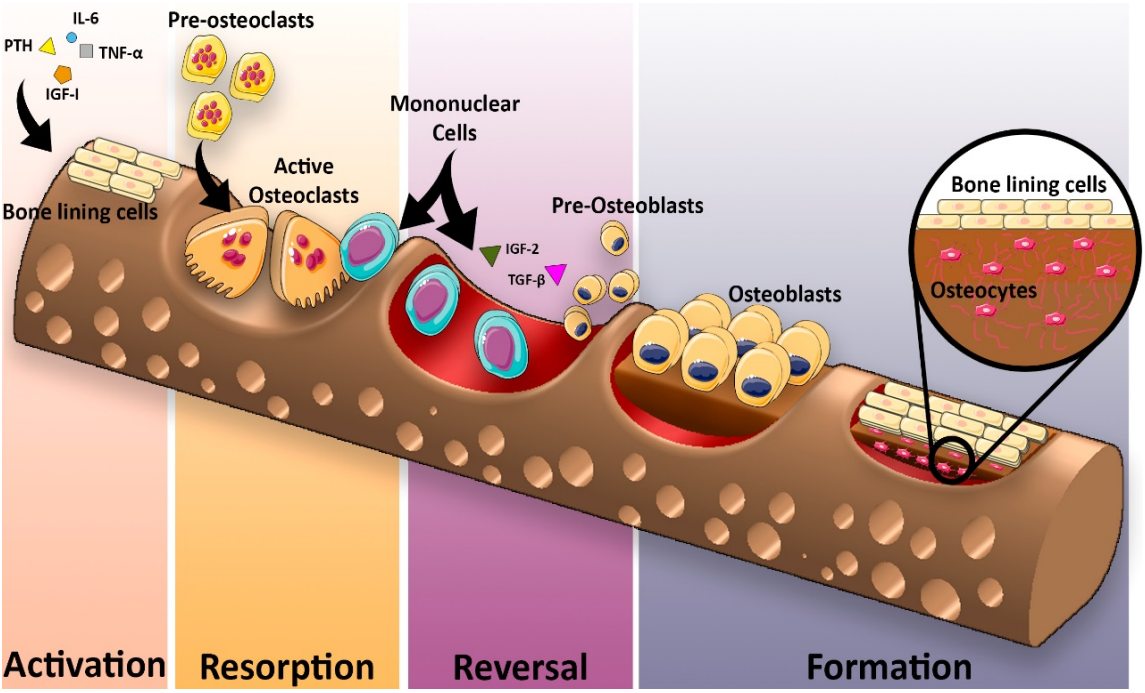

Figure 3. Schematic representation of the different phases of the bone remodeling process.

1.4. Bone disorders

Even though the bone remodeling process is one of the most reliable in the body, there are circumstances where it fails. In fact, the pathologies inherent to bone disorders are almost always related to this cycle [22, 26]. Abnormal growth can cause gigantism or dwarfism, while abnormal collagen contents can lead to osteogenesis imperfecta. Mineral and vitamin deficiencies cause rickets and bacterial infections can cause osteomyelitis [7, 27]. Figure 4 presents an overview of the pathologies associated with some bone disorders.

1.4.1. Osteoporosis

Osteoporosis is a common musculoskeletal disease characterized by an increased bone resorption and, as consequence, decreased bone mineral density [7, 15, 26, 28]. It is believed that sex steroid hormones, either directly or indirectly, regulate the production of the cytokines (e.g. M-CSF) that promote the production of osteoclasts [26, 29]. Therefore, this disease affects

mainly the elderly population, especially woman beyond the age of 50 years due to menopausal estrogen deficiencies that increase the bone resorption [22]. Contrariwise, male population have a more gradual decrease in sex steroid hormonal levels with aging, which may account for a less severe decrease in bone strength [7, 15, 30]. The most common osteoporotic fractures involve the hip, vertebral column, and forearm and may result in morbidity or in severe cases the death of patient [22, 31]. Unhealthy diet (low calcium or vitamin D intake, alcohol abuse, and high caffeine intake), sedentary lifestyle, nulliparity, aging, smoking, and low body weight are also risk factors that may trigger the development of osteoporosis [15].

1.4.2. Paget's disease

Paget's disease is the second most common metabolic bone disease after osteoporosis [7]. This disease is characterized by focal areas of excessive bone resorption alternated with areas of increased bone formation, leading to the formation of abnormal bone, pain, pathologic fractures, deafness and nerve compression syndromes [22, 32, 33]. Paget's disease has an increased prevalence in population with an age over 40 years, affecting about 5% of women and 8% of men at age of 80 [22, 32, 33]. In this disease, the osteoclast precursors from the bone marrow show increased sensitivity to factors that stimulate bone resorption including RANKL [7, 28]. Genetic factors and gene mutations have also an important role in this disease [33]. Nevertheless, sedentary lifestyle and deficient nutrition are also factors that may be involved in the Paget's disease arising.

1.4.3. Osteomyelitis

Osteomyelitis is defined as an inflammation of bone tissue accompanied by its destruction that occurs due to a microbial infection [27, 28, 34]. Furthermore, it can also be triggered by fractures that occur due to trauma or other diseases [28]. Mast *et al* reported that osteomyelitis incidence after severe open fractures is higher than 44% [34]. Moreover *Staphylococcus aureus* (*S. aureus*) is the most common pathogen responsible for the emerge of this disease [27]. This microorganism develops a range of extracellular and cell-associated factors, that promote its colonization capacity and virulence [27].

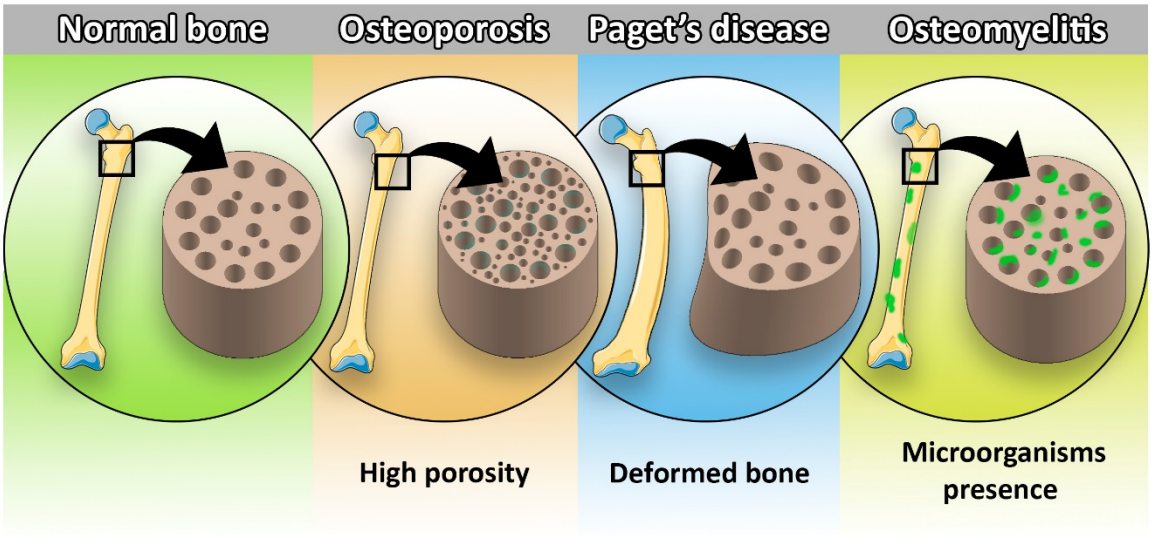

Figure 4. Schematic representation of the main human bone disorders. Osteoporosis is mainly characterized by bones with high porosity; Paget´s disease is characterized by the creation of deformed bone; Osteomyelitis is characterized by the fungal presence on bone tissue.

1.5. Bone grafts

Nowadays, autografts (figure 5A) remain as the most common therapy used for the treatment of osseous defects [21, 35, 36]. This procedure involves the transplantation of bone tissue from another part of the patient's body (usually trabecular bone from iliac crest) to the bone-damaged site [19]. Although it has a good rate of success, the number of cases in which this procedure can be used is restricted, due to the limited amount of available tissue and also by the induction of morbidity at the donor site [19, 21, 37]. Consequently, allograft and xenografts (figure 5B and C) (bone from human and non-human cadavers, respectively), are an alternative that in some cases is used by surgeons [36, 37]. However, these procedures cannot be seen as efficient therapeutic alternatives to autografts since they present risks of immune rejection, viral transmission and their use is dependent on stocks available on bank tissues [19, 21, 36].

Hence, in the last years, the limitations associated with the current clinical approaches lead to the development of alternative bone repair techniques based on Tissue Engineering (TE) [38].

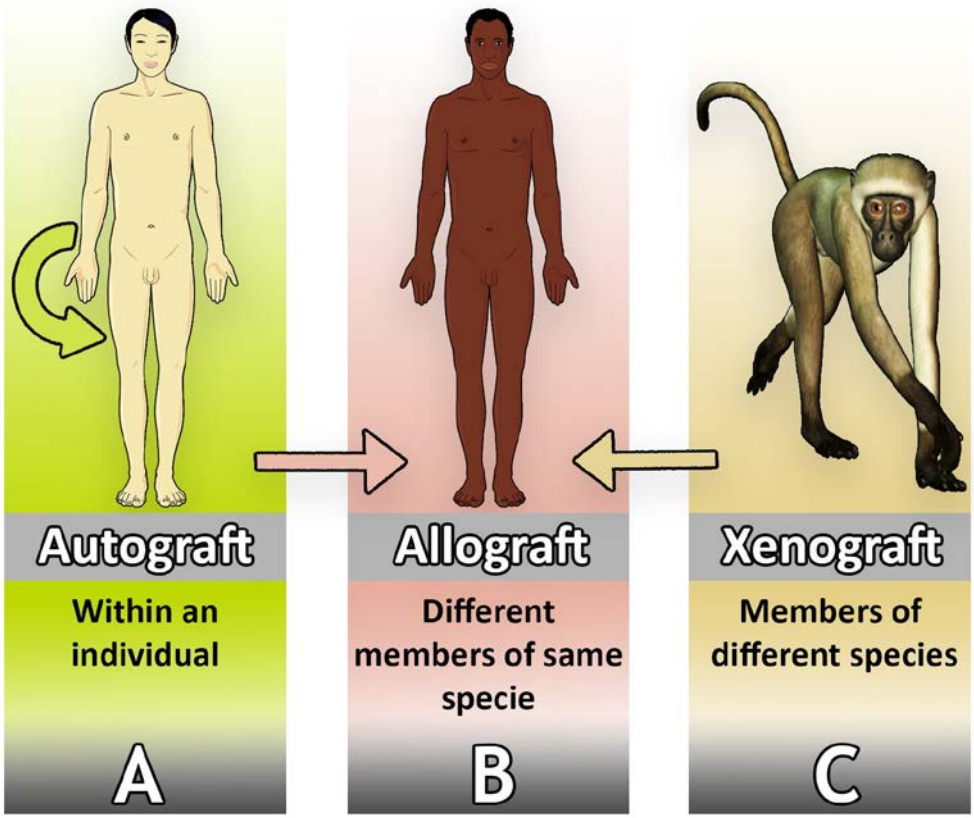

Figure 5. Schematic representation of the main types of bone grafts used in the clinic. Autografts are obtained from the patient's body (A); Allografts are obtained from individuals of the same species (B); Xenografts are obtained from organisms of other species (C).

1.6. Tissue engineering

TE is an interdisciplinary field of research that applies the principles of engineering and life sciences towards the development of biological substitutes that restore, maintain, or improve damaged tissue functions [19, 36, 39]. Recently, this research area emerged as a new and promising approach for bone repair and regeneration [3]. The main strategy of TE involves the functionalization of supporting three-dimensional (3D) structures with cells that can be isolated from healthy humans, nanoparticles, growth factors or other bioactive molecules, in order promote the re-establishment of the structure and functions of the different tissues (figure 6) [3, 35, 38-41].

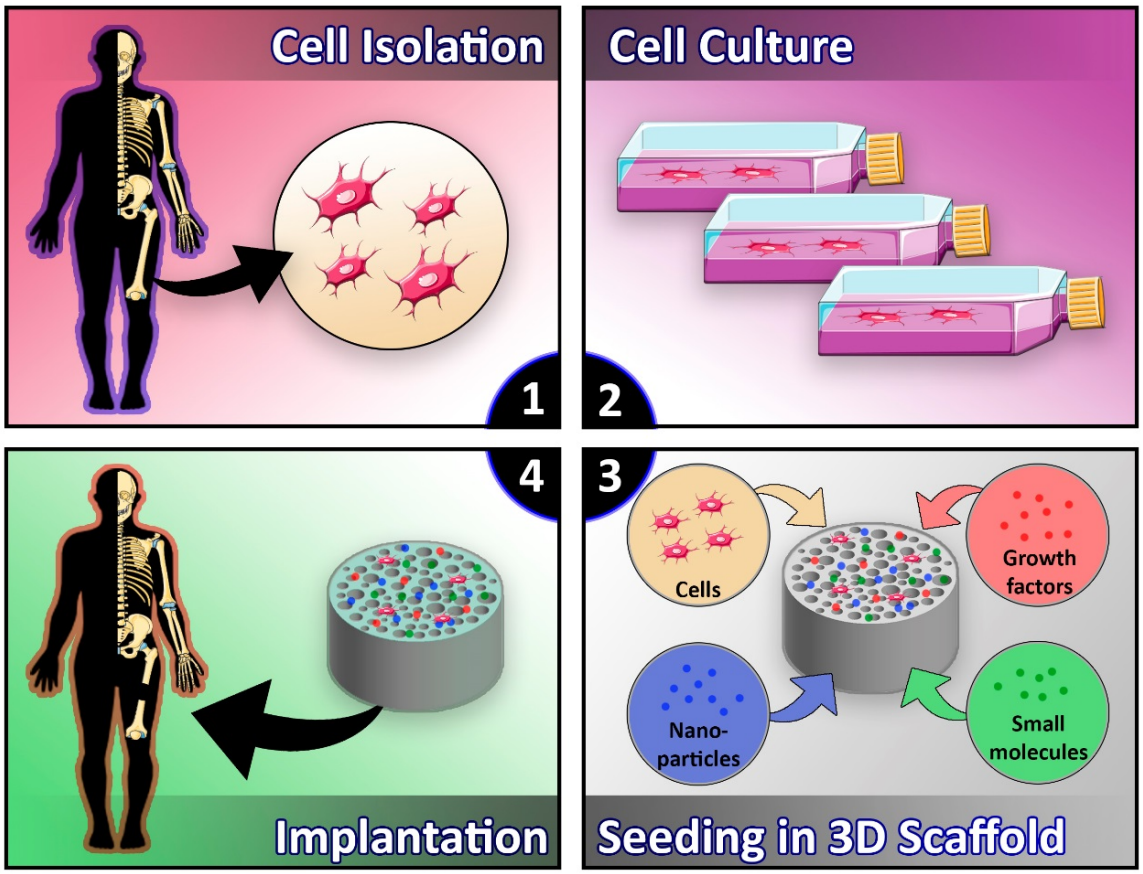

Figure 6. Representation of tissue engineering approach used for bone regeneration. Cell isolation from healthy human (1); Cell culture (2); Incorporation of cells, growth factors, nanoparticles or other molecules within scaffolds (3); Implantation of the scaffold on the injured patient (4).

1.6.1. 3D scaffolds

In particular, bone TE revolutionized the therapeutic approaches used for bone reconstruction due to the development of 3D scaffolds [38]. The aim of these scaffolds is to restore the structure and functions of native bone tissue by acting as a temporary support for cell proliferation and extracellular matrix deposition [19, 38, 39].

An ideal scaffold should meet a number of key requirements, which determine their suitability for tissue engineering purposes:

- Biocompatibility

Biocompatibility represents the ability of a material to support normal cellular activity including adhesion, proliferation and differentiation without eliciting any local or systemic immune response [38, 40, 42]. Generally, scaffolds should be fabricated from materials that do not trigger the immunogenic reactions. Furthermore, the degradation products of the scaffolds must also be biocompatible and easily eliminated from the body [42, 43]. This property is directly related

with interactions between blood, scaffold surface, and degradation products, which are released from the scaffold [39, 42, 44].

- Biodegradability

An ideal 3D scaffold should be degraded at a rate that iscompatible with the rate of bone growth [38, 39, 43]. In addition, the degradation products of the scaffolds must not elicit any adverse effect on the host [40]. Therefore, the degradation profile of the scaffold should be regarded in order to fulfil the requirements of the patient (i.e. age and type of injured bone) [42].

- Surface properties, osteocondutivity and osteoinductivity

Surface properties (i.e. charge, roughness, hydrophilicity and chemical composition) are determinant for controlling cellular adhesion and proliferation [3, 42, 43]. These properties are directly related with the osteoconductive and osteoinductive capacity of the 3D scaffold [36]. Osteoconduction is a process by which bone cells migrate to the surface of the scaffold through a fibrin clot, that is formed immediately after the material be implanted [19, 36, 40]. On the other hand, osteoinduction is a process by which the osteoprogenitor cells are stimulated to undergo through an osteogenic differentiation process [42]. Therefore, the use of osteoconductive and osteoinductive materials in bone tissue engineering is required to accomplish an effective bone regeneration process [36]. Osteoconduction is promoted by rough and positively charged surfaces that create a matrix compatible with cell adhesion and proliferation [3, 39, 40, 42, 45]. The scaffolds may also release osteoinductive signals through the action of growth factors or other bioactive molecules that induce differentiation of bone cells [19, 36, 42].

- Antimicrobial activity

Bacterial infections are currently regarded as the most severe and devastating complications associated with the implantation of biomaterials in the human body [46, 47]. Nowadays, it is estimated that 65-80% of bacterial infections are caused by organisms that form biofilms on implants' surface compromising their successful application [46, 48]. Furthermore, it is estimated that *S. aureus* strain is responsible for 30% of all implant infections [46]. In order to reduce this problem, many efficient strategies can be adopted, namely by avoiding bacterial adhesion or the release of antimicrobial agents [47]. Commonly antibacterial agents incorporated in bone scaffolds include metallic nanoparticles, antibiotics, antimicrobial polymers, among others [47, 49].

- Porosity

Porosity is defined as the percentage of void space available in scaffolds. An ideal 3D scaffold should have a suitable interconnected porosity (higher than 90%) in order to ensure support for cellular penetration, differentiation, and consequently improve new bone tissue formation [37,

[38, 40]. Regarding the pore size, it must be between 100-300 μm, for allowing a successful diffusion of essential nutrients, oxygen, cellular metabolites and eventual blood vessels in-growth [13, 43, 45]. However, scaffolds with an excessive porosity present compromised mechanical properties [38, 42, 43]. Furthermore, the porosity also influences the rate of degradation [43]. In fact, a high porosity area enhances the interaction of scaffold with host tissue, which results in materials degradation [13, 38].

- Mechanical properties

Bone scaffolds are responsible for providing mechanical integrity at the lesion site until the new bone is fully matured [38, 39, 42]. The mechanical properties of the scaffold should be similar to that displayed by native bone tissue in order to support the handling during implantation and contraction forces that occur during bone regeneration. Mechanical properties of bone vary widely from cancellous to cortical bone [5, 42]. Young's modulus of cortical bone is comprised between 15-20 GPa while for cancellous bone it is between 0.1-2 GPa [40]. In turn, the compressive strength is comprehended between 100-200 MPa for cortical bone, and 2-20 MPa for cancellous bone [40]. In order to achieve optimal results, it is necessary to carefully optimize the mechanical properties of a scaffold with its degradation kinetics [39]. In fact, a scaffold material needs to degrade at a controlled rate, that allows the maintenance of scaffold's integrity along the healing process [39, 42].

1.6.2. Biomaterials used for scaffold production

The selection of the most appropriate biomaterial for the production of scaffolds aimed for bone tissue engineering applications is a crucial step since its properties will determine the final properties of the scaffold [21, 42, 50]. Various materials have been used, so far, for the production of scaffolds that meet the requirements mentioned above [39, 50]. Generally, due to their chemical composition the materials can be divided in to four main groups: ceramics, polymers, metals and composites [21].

1.6.2.1. Ceramics

Ceramic scaffolds are typically characterized by their high mechanical stiffness, very low elasticity and a hard surface [36]. Generally, bone ceramic scaffolds are produced with materials containing calcium, such as hydroxyapatite (HA) and tricalcium phosphate (TCP) [13, 21, 36, 50]. These ceramics are valuable options for bone tissue engineering since they exhibit excellent biodegradability and biocompatibility behavior, due to their chemical and structural resemblance to the mineral phase of native bone [21, 42, 51]. Moreover, ceramics can promote interactions with osteogenic cells, enhancing osteoblasts differentiation, proliferation and consequently improve the bone healing process [13, 52]. In addition, it is described that these bioactive ceramics are capable of inducing mineralization at the surface of the scaffolds, increase their biointegration, and consequently the bone regeneration process [13, 42]. However,

their clinical applications for tissue engineering purposes has been limited due to their brittleness and shape related issues [50].

1.6.2.2. Polymers

Polymers are macromolecules composed of many repeated subunits, that present bioactivity, biodegradability and flexibility properties that are fundamental for their use in bone tissue engineering [3, 38, 42, 50, 53]. According to their source, polymers can be categorized as natural and synthetic [45, 50].

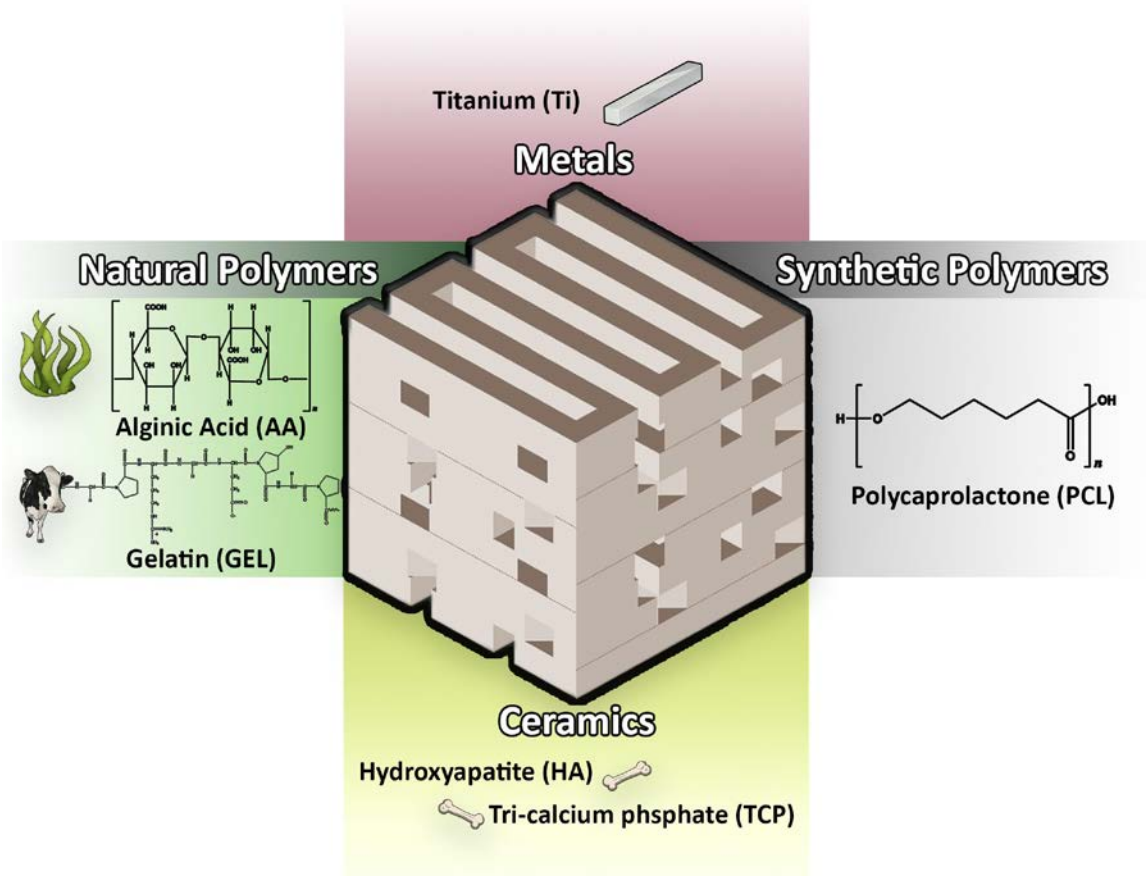

Figure 7. Schematic representation of materials used in bone tissue engineering.

- Natural polymers

Natural polymers (e.g. alginic acid (AA), cellulose, chitosan, collagen, gelatin (GEL), hyaluronic acid and silk) are obtained from natural sources, such as plants and animals [3, 54, 55]. These materials present as main advantages their low immunogenic potential and biocompatible behavior [45, 50, 54]. On the other hand, the limitations of naturally derived polymers include weak mechanical behaviour, fast degradation rates as well as hard processing and purification [45, 53, 54].

AA is an example of a natural polymer extracted from cell walls of brown algae [56, 57]. This polymer is a polyanion composed of two repeated monomer units: ß-d-mannuronate (M) and α-l-guluronate (G) [56]. Physical and mechanical properties of AA are highly related to the chain length and properties of the guluronate present on its composition [56, 58]. Alginate, with a high content of G residues becomes stiff and stable, whereas AA with a low content of G residues is more elastic and less stable [58, 59].

Additionally, GEL is obtained from collagen denaturation, which is gathered from animals [38, 53]. This negatively charged protein contains sequences composed of Arginine, Glycine, and Aspartic Acid (RGD), that improve cell interaction with the biomaterial and, as consequence, enhances the deposition of new bone tissue [45, 53 53].

- Synthetic polymers

Synthetic polymers are chemically synthetized polymers that are widely used in the bone tissue engineering field, due to their high versatility and reproducibility [38, 40, 42, 45]. In comparison to natural polymers, they are generally less biocompatible and more resistant. One of the most common polymers used for bone regeneration is Polycaprolactone (PCL) [3, 13]. PCL is an aliphatic linear polyester, that is synthesized through ring-opening polymerization of ε-caprolactone. It is characterized by being biocompatible, bioresorbable and inexpensive [3, 50]. PCL degrades through of hydrolysis of its ester linkages in physiological conditions and, therefore, has been used as a valuable material for tissue engineering applications [38, 40]. However, the use of PCL in tissue engineering is compromised by its hydrophobic nature, resulting in limited cellular adhesion and uncontrolled biological interaction [40].

1.6.2.3. Metals

Metals are characterized by presenting a great compressive strength and fatigue resistance [54]. The most common metal used in scaffolds production is titanium (Ti) [40]. Ti implants are widely used due to their mechanical properties. However, several complications have been associated with these type of implants, such as infections or excess of fatigue loading. Moreover, the use of metallic implants can release toxic ions or particles through corrosion causing inflammation, tissue loss and in severe cases patients dead [40, 60].

1.6.2.4. Composites

Composite scaffolds have in their constitution different materials, like ceramics and polymers [13, 40, 51]. These combinations are carried out in order to overcome the disadvantages of single material [43]. This combination allows a creation of structures with an excellent balance between strength and toughness [13, 43, 51, 52]. Specifically, to overcome the brittleness of the ceramics, they are combined with polymers in order to increase the flexibility of the composite materials, making them more suitable for bone tissue engineering applications [43, 52, 61].

1.6.3. Antimicrobial functionalization of scaffolds

As described above, bacterial colonization of scaffold's surface is one of the worst possible events, that can occur when materials are implanted in the human body, leading to an obligatory implant removal from the body [46, 47]. *S. Aureus* is usually responsible for this type of complications [46].

In order to surpass these drawbacks, the development of scaffolds endowed with antimicrobial activity is fundamental to avoid infections related to biomaterials implantation [47]. Many approaches have already been adopted in order to confer antimicrobial properties to tissue engineering constructs, such as modification of surface charge, incorporation of metallic nanoparticles, quaternary ammonium compounds, halogens, antibiotics or drugs [47, 49, 62].

1.6.3.1. Salicylic acid (SA)

SA is a phenolic compound produced by plants *Nicotiana tabacum*, *Cucumis sativus*, and *Arabidopsis thaliana* [63, 64]. This non-steroidal anti-inflammatory drug plays an important role in several physiological processes, such as the induction of plant defense responses against pathogen attacks [63]. SA owns anti-inflammatory, analgesic, antipyretic, and antimicrobial properties that can promote bone regeneration [49, 63]. Despite of their attractive properties, SA is not yet widely used in bone tissue engineering applications. Recently, Griffin and collaborators produced SA-derived poly(anhydride-ester) electrospun fibers for the regeneration of the peripheral nervous system. The authors concluded that SA-based polyanhydride fibers may offer great number of advantages not only for nerve regeneration but also for a variety of biomedical applications [65].

1.6.3.2. Silver nanoparticles (AgNPs)

AgNPs are the most studied metallic nanoparticles for the prevention of implant-based infections [66, 67]. The antimicrobial activity of AgNPs have been attributed mainly to its oxidized form (Ag+), which is able to anchor to the bacterial cell wall and to penetrate through it, thereby causing the disruption of cell membrane [66]. This metallic compound can also interact with the thiol groups of many vital enzymes and, subsequently, inactivate them [67]. Moreover, silver ions act on the sulfur and phosphorus components of DNA leading to inhibition of DNA replication [66]. Due to their high surface area to volume ratio, AgNPs present enhanced reactivity against a range of different bacterial strains that have clinical relevance [67].

1.6.4. Techniques used for scaffolds production

To fabricate scaffolds aimed for bone tissue engineering, various approaches can be used [3, 38, 45]. Generally, conventional fabrication techniques such as, salt leaching, gas forming, phase separation and freeze-drying do not enable the precise control of internal scaffold architecture or the fabrication of complex architectures [3, 38, 40, 45, 50]. Rapid prototyping (RP) approaches

comprise 3D printing, elective laser sintering, stereolithography, and fused deposition modeling that allow the production of scaffolds with interconnected pores [38, 50]. These techniques have also a better design repeatability and allow a creation of scaffolds with good mechanical requirements [40, 50].

1.6.4.1. 3D printing using a Fab@Home printer

3D printing is one of the most used RP technique in the area of tissue engineering. In particular, 3D printing using a Fab@Home printer (Figure 8) allows the use of a wide range of materials, such as composites compromising ceramics and polymers [38, 50]. The deposition of successive layers to produce the final 3D model, enables a better control of pore sizes, morphology, and overall matrix porosity in comparison to other fabrication methods. During the fabrication process, the syringe content is compressed in order to extrude the 3D structure onto a platform, according to the CAD (computer-aided design) file [40]. This feasible, cheap and reproducible technique allows the creation of complex 3D structures with high resolution and with a controlled internal architecture [50, 51]. Moreover, structures produced by 3D printing present regular morphology and improved mechanical properties according to the demands of the damaged bone [50, 51].

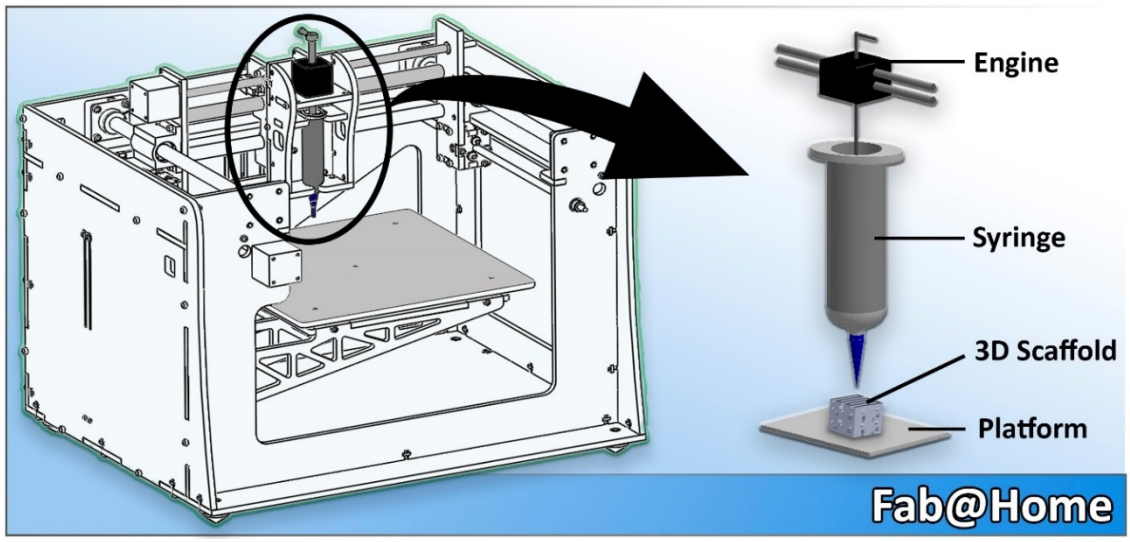

Figure 8. Schematic representation of the Fab@Home printer used to produce 3D scaffolds used in this study.

However, this technique possesses limitations like other techniques. The scaffolds produced by 3D printing are not fully capable of reproducing the ECM of bone tissue, thus compromising the bone healing process [68].

1.6.4.2. Electrospinning (ES)

In order to mimic the ECM and enhance the bone healing process, ES arise as a feasible alternative. The term ES was proposed by Reneker and co-workers in the 1990s based on the

earlier used term, 'electrostatic spinning' [69-71]. A basic ES system (Figure 9) is usually composed by four main components, namely, a syringe pump (responsible to control the flow rate of polymers), a voltage power supply (provides the force to stretch the charged polymer solution into fibers), a needle (which shifts the solution into the high electric field) and a collector (where electrospun nanofibers are collected) [45, 71]. During the ES process, the syringe pump is used to force the content through a needle attached to the syringe with a controlled flow rate [69, 72]. When a high voltage is applied at the tip of the capillary needle, it induces repulsive electrical forces on the droplet surface. The charge causes the elongation of the droplet into a cone, known as the Taylor Cone [69]. Once the voltage reaches a critical value the repulsive electrostatic forces overcome the surface tension forces and a liquid jet emerges from Taylor Cone, reaching the collector in few nanoseconds [70]. While the jet moves toward the collector, the solvent evaporates and ultra-thin dry fibers are collected on the metallic collector [70].

The fabrication of the nanofibers is dependent on specific apparatus parameters such as the precursor solution (e.g. conductivity, surface tension, viscosity and solvent selection), processing variables, and ambient conditions [69, 70]. This cost-effective and versatile technique employs electrostatic that allows the production of electrospun meshes, with diameters ranging a few microns down to tens of nanometers, that can be used to deliver specific bioactive molecules (e.g. cells, vitamins, growth factors, drugs) [3, 45]. Moreover, the area-to-volume ratio of the nanofibers is also important to enhance cell adhesion and proliferation [3, 13, 45]. However, these nanofibers structures display very weak mechanical properties when compared with trabecular bone.

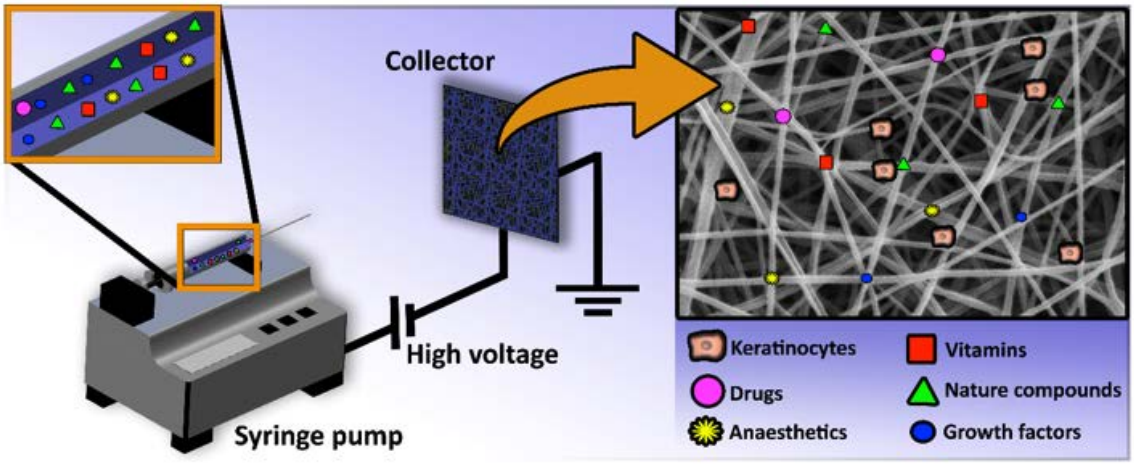

Figure 9. Schematic representation of the electrospinning apparatus used for the production of nanofibrous meshes that coated the 3D scaffolds.

To surpass such constraint, researchers are currently developing new 3D structures that combine different production methods, like 3D Printing and ES, in order to produce constructs that can be used in bone tissue engineering. Recently, Yeo and Kim fabricated PCL/β-TCP composite scaffolds by 3D printing and coated them with collagen/hydroxyapatite nanofibrous meshes [73].

The hybrid scaffolds produced in this study showed improved mechanical properties and enhanced cell adhesion and proliferation, features that are crucial for a faster and effective bone repair process be attained [73].

1.7. Aims

The overall aim of the present thesis was to develop and characterize new 3D hybrid scaffolds coated with nanofibers containing antimicrobial agents that can be used in bone tissue engineering.

The specific aims of this study were:

● Optimization of the viscosity of the solutions

● Design and production of 3D hybrid scaffolds

● Study the antimicrobial activity of the 3D hybrid scaffolds produced

● Evaluation of the mechanical, physicochemical and biological properties of the produced 3D hybrid scaffolds

Chapter II - Materials and Methods

2. Materials and Methods

2.1. Materials

3-(4,5-dimethylthiazol-2-yl)-2,5-diphenyltetrazolium bromide (MTT) was purchased from Alfa Aesar (Ward Hill, USA). Trifluoroethanol (TFE) was purchased from Acros Organics (New Jersey, USA). Alginic acid (AA), Amphotericin B, Calcium Chloride ($CaCl_2$), Dulbecco's modified Eagle's medium (DMEM-F12), Ethylenediaminetetraacetic acid (EDTA), Gelatin 180 bloom (GEL), gentamicin, kanamycin, LB Broth, Phosphate-buffered saline solution (PBS), Polycaprolactone (PCL) (molecular weight 80,000 g mol^{-1}), Sodium borohydride ($NaBH_4$) and Trypsin were purchased from Sigma-Aldrich (Sintra, Portugal). Dimethyl sulfoxide 99.9% (DMSO) was obtained from Thermo Fisher Scientific (Rockford, IL,USA). Fetal bovine serum (FBS) (free from any antibiotic) was acquired from Biochrom AG (Berlin, Germany). Normal human osteoblast (hOB) (406-05f) cryopreserved cells were purchased from Cell Applications, Inc. (San Diego, USA). Polyvinylpyrrolidone (PVP) (molecular weight 44,000 g mol^{-1}) was obtained from BDH Chemicals Ltd (Poole, UK). Silver nitrate ($AgNO_3$), Sodium hydrogen carbonate ($NaHCO_3$) and Tricalcium phosphate (TCP) were bought from Panreac (Barcelona, Spain).

2.2. Methods

2.2.1. Preparation of TCP/AA based scaffolds

To produce 3D scaffolds with a proportion of 50/50 (w/w) of TCP/AA, a 15% (w/v) of AA solution was prepared by dissolving the polymer in double deionized and filtered water (obtained using a Milli-Q Advantage A10 ultrapure Water Purification System, resistivity=18.2 MΩ/cm, at 25°C) with overnight agitation. The solution was then homogenized using a X10/25 Ultra-turrax® (Ystral, Germany) for 30 min. Then, TCP powder was added to the AA solution in a 50/50 ratio followed by homogenization. After the dissolution of all the components, 5% (w/w) $CaCl_2$ (crosslinking agent) was added to the composite mixture until a ratio of 1:2 of $CaCl_2$:AA was obtained. Alginate polymer chains got crosslinked (calcium ions replace the sodium ions of AA) leading to an increase of the solution's viscosity that is fundamental for scaffolds production. Lastly, a syringe (10 cc Luer Lock) was filled with the $CaCl_2$:AA solution in order to proceed to solution extrusion using a Fab@Home (see figure 1A for further details). After their production, the scaffolds were immersed in a 5% $CaCl_2$ solution for 24 h to achieve a complete crosslinking of the printed structure and clear-cut. Afterward, scaffolds were air-dried at room temperature (RT) for 48 h.

2.2.2. Production and characterization of silver nanoparticles

AgNPs were produced by performing the chemical reduction of silver, as previously described by Silva and colleagues [74]. Briefly, AgNPs were produced using $AgNO_3$ as a metal precursor and $NaBH_4$ as reducing agent. Initially, 5 mL of $AgNO_3$ solution (4 mM) were added dropwise to 30 mL of $NaBH_4$ solution (4 mM), under constant stirring at RT, until an $AgNO_3$:$NaBH_4$ molar ratio of 1:5 was achieved. The production of AgNPs was confirmed by the change in the solution color (from colorless to yellow). Subsequently, 5 mL of 0.2 % PVP solution, one of the most commonly used metal stabilizers, were added to the AgNPs already produced in order to avoid nanoparticles aggregation [74]. All procedures were performed in the dark in order to prevent the photodecomposition of $AgNO_3$.

The hydrodynamic diameter of the produced nanoparticles was determined by dynamic light scattering (DLS) analysis, using a Zetasizer Nano ZS particle analyzer (Malvern Instruments, Worcestershire, UK).

2.2.3. Production of the electrospun nanofibers meshes

Different polymeric solutions composed of GEL/PCL loaded with AgNPs and GEL/PCL loaded with SA were produced. Briefly, 8% GEL and 6% PCL (combined at 1:1 w/w ratio) were dissolved in 80% TFE (w/v). After the dissolution, AgNPs (0.04 M) (w/v) were added to the polymeric blend. For GEL/PCL loaded with SA production, 8% GEL, 6% PCL and 8% SA (combined at 1:1:1 w/w ratio) were dissolved in TFE 80 % (w/v). Each solution was then electrospun at constant flow rate of 2.8 mL/h for 20 min, at 18 kV, with 15% humidity, and at a temperature of 26°C in order to coat TCP/AA scaffold' surface using a rotative collector (Figure 10). The system setup was comprised of a high voltage source (Spellman CZE1000R, 0–30 kV), a syringe pump (KDS-100), a plastic syringe with a stainless steel needle (21 Gauge) and an aluminum disk connected to a copper collector, placed at a working distance of 10 cm.

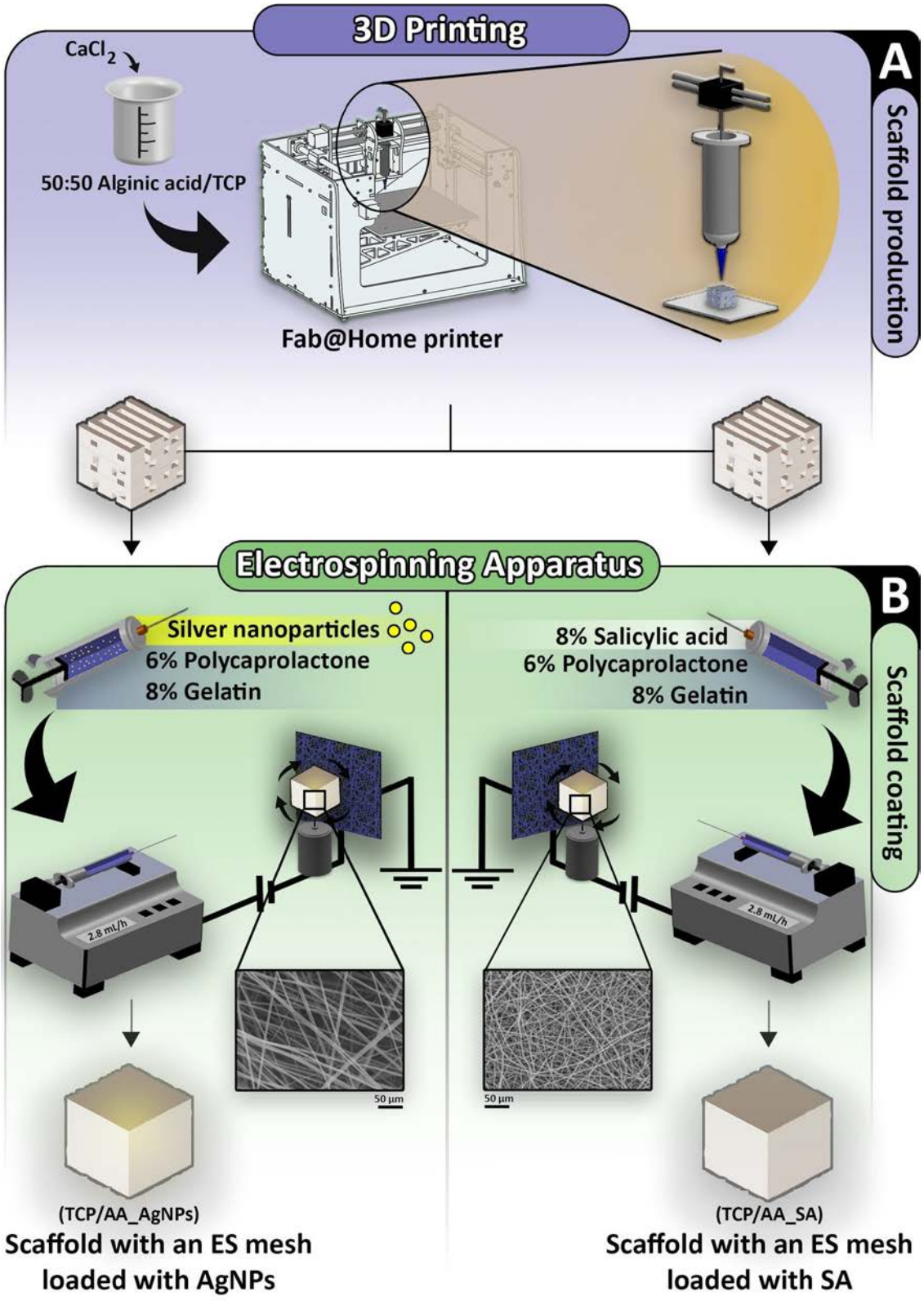

Figure 10. Schematic representation of the process used to produce 3D hybrid scaffolds. Scaffolds were initially produced using a RP technique (A) and subsequently coated with an electrospun mesh loaded with AgNPs or SA, respectively (B).

2.2.4 Physicochemical and morphological characterization of the scaffolds

2.2.4.1. Attenuated Total Reflectance-Fourier Transform Infrared Spectroscopy analysis

To characterize the composition of the produced scaffolds, Attenuated Total Reflectance-Fourier Transform Infrared Spectroscopy (ATR-FTIR) analysis was performed. The spectra acquired for the different samples represent an average of 128 scans, between 400 and 4000 cm^{-1}, with a spectral resolution of 4 cm^{-1}. All the samples were crushed to powder, before being analyzed, mounted on a diamond window, and the spectra were recorded using a Nicolet iS10 FTIR spectrophotometer (Thermo Scientific, Waltham, MA, USA). Moreover, all raw materials used for scaffold and nanofibrous mesh production were analyzed, in order to compare the spectra of individual components with those of the produced scaffolds [51, 75, 76].

2.2.4.2. Energy dispersive spectroscopic analysis

In order to perform the elementary analysis of the samples, an energy dispersive spectroscopic (EDS) technique was used. The different samples were placed on aluminum stubs, and then analyzed using a XFlash Detector 5010 (Bruker Nano, Germany).

2.2.4.3. Characterization of the mechanical properties of the scaffolds

The mechanical behavior of the scaffolds, in wet and dry conditions, was evaluated through compression assays as previously described elsewhere [76]. All the measurements were performed at RT using a Shimadzu AG-X Tensile Testing Machine (Tokyo, Japan), with a crosshead speed of 2 mm/min and a load cell of 10 kN. Five specimens of each sample, in the dry and wet state, were used in each assay [76-78].

The compressive strength (Cs) of the scaffolds was calculated according to equation (1).

$$C_s = \frac{F}{w \times l} \quad (1)$$

Where F corresponds to the load at the time of fracture, w and l represent the width and length of the scaffold, respectively.

The Young Modulus (YM) was calculated through equation (2).

$$YM = \frac{C_s}{H_d} \quad (2)$$

Where H_d stands for the height deformation at maximum load, and C_s is the scaffold compressive strength obtained from equation 1.

2.2.4.4. Evaluation of scaffolds' porosity

The porosity of the different scaffolds was determined using a liquid displacement method, adapted from Torres and collaborators [78]. Briefly, 3 specimens of each formulation were weighed, immersed in absolute ethanol (EtOH) for 48 h and then, weighed again. Finally,

scaffold's porosity was calculated by determining the amount of EtOH absorbed by the scaffolds, through equation:

$$\text{Porosity (\%)} = \left(\frac{W_w - W_d}{D_{ethanol} \times V_{Scaffold}}\right) \times 100 \quad (3)$$

Where W_w and W_d are the wet and dry weights of the scaffolds, respectively, $D_{ethanol}$ represents the density of EtOH at RT and $V_{scaffold}$ the volume of the wet scaffold.

2.2.4.5. Characterization of the swelling profile of the scaffolds

Four samples of each scaffold formulation, with a known dry weight, were placed in Eppendorfs containing 2 mL of DMEM-F12 cell culture medium (pH=7.4) and kept at 37°C under stirring. Then, scaffolds were retrieved from the solution at predetermined intervals, and their weight was determined after removing the excess of medium with a filter paper [56, 76]. Subsequently, samples were re-immersed in the culture medium. Equation (4) was used to calculate the swelling ratio of the samples.

$$\text{Swelling ratio (\%)} = \left(\frac{W_t - W_0}{W_0}\right) \times 100 \quad (4)$$

Where W_0 represents the initial dry weight of the scaffolds and W_t is the final weight of scaffolds.

2.2.4.6. *In vitro* analysis of the biodegradation profile of the samples

Three samples of each scaffold formulation were weighed (W_i), placed in 6-well plates and fully immersed in DMEM-F12, at 37°C, during 7 days accordingly to the method previously used by Fradique and colleagues [56, 76]. The DMEM-F12 medium was changed every 3 days and the weight of the samples was determined after 1, 4 and 7 days of incubation. To do so, scaffolds were washed with deionised water in order to remove the ions adsorbed on their surface and then they were lyophilized. The dry weight was noted as W_t. The degradation profile of the scaffold was calculated using equation (5) at three time points:

$$\text{Weight loss (\%)} = \left(\frac{W_i - W_t}{W_i}\right) \times 100 \quad (5)$$

Where W_i corresponds to the initial weight of the sample and W_t to the weight of the sample at time t.

2.2.4.7. Characterization of scaffold biomineralization activity *in vitro*

The *in vitro* formation of apatite layers on scaffold's surface was studied in a protein-free and acellular simulated body fluid (SBF). SBF solution had a similar ionic composition to that found in human blood plasma (142.0 mM Na^+, 5 mM K^+, 1.5 mM Mg^{2+}, 2.5 mM Ca^{2+}, 147.8 mM Cl^-, 4.2 mM HCO_3^-, 1.0 mM HPO_4^{2-} and 0.5 mM SO_4^{2-}), and a pH of 7.4 [79, 80]. Five scaffolds with equal weight and shape were immersed in a SBF (that was prepared as previously described elsewhere [79], followed by samples incubation at 37°C for 4, 7 and 14 days. After each specific period, the

scaffolds were removed and rinsed three times with deionized water. The biomineralization on the surface of the scaffolds was characterized through Scanning Electron Microscopy (SEM) and EDS analysis.

2.2.5. Characterization of the biological properties of the scaffolds

2.2.5.1. Evaluation of cell viability and proliferation in the presence of the scaffolds

The cytotoxic profile of 3D scaffolds was characterized according to the guidelines set for ISO 10993-5 standard. Briefly, scaffolds were cut into pieces with appropriate sizes and placed into 96-well plates to be sterilized by UV irradiation, for 120 min. Then, cells were seeded at a density of $10x10^3$ cells per well, to characterize cell viability and proliferation in contact with samples after 1, 3 and 7 days. The culture medium was replaced every two days until the end of the assay. Then, the medium was removed and 50 µL of MTT (5 mg/mL PBS) were added to each sample, followed by their incubation for 4 h, at 37°C, in a 5% CO_2 atmosphere. Then, cells were treated with 200 µL of DMSO (0.04N) for 30 min. A microplate reader (Biorad xMark microplate spectrophotometer) was used to determine the absorbance of each well at 570 nm. Cells cultured without materials were used as a negative control (K–), whereas cells cultured with EtOH (90%) were used as positive control (K+).

2.2.5.2. Evaluation of the bactericidal activity of the scaffolds

S. aureus, a gram-positive bacterium obtained from the clinic was used to study the bactericidal activity of the hybrid scaffolds produced. Antibacterial performance of the different scaffolds was evaluated the modified Kirby-Bauer technique (32). Briefly, 200 µL of bacteria medium (with a concentration of 1×10^8 colony forming units (CFU)/ mL *S. aureus*) were dispensed onto an agar plate, then the scaffolds disks (n=3) were placed on the agar plate and incubated for 5 days, at 37 °C. After that, the inhibitory halos around the samples were measured using ImageJ software and bacterial growth was further confirmed by SEM analysis.

2.2.5.3. Characterization of the morphology and biological performance of the scaffolds

SEM analysis was performed to characterize the morphology, biomineralization activity, cellular adhesion and also to evaluate the presence of bacteria on scaffold's surface. Samples were initially fixed for 4 h with 2.5% (v/v) glutaraldehyde, and then washed three times with PBS and dehydrated with growing concentrations of EtOH (50, 60, 70, 80, 90 and 99.9%). Subsequently, scaffolds were frozen using liquid nitrogen and freeze-dried for 3 h. Finally, all the samples were mounted onto aluminum stubs with Araldite glue and sputter-coated with gold using a Quorum Q150R ES sputter coater. SEM images were then acquired with different magnifications, at an acceleration voltage of 20 kV, using a Hitachi S-3400N Scanning Electron Microscope.

Transmission electron microscopy (TEM) images were also acquired with a Hitachi–HT7700 microscope using an accelerating voltage of 80 kV, to characterize the internal morphology of the electrospun mesh used for coating the hybrid scaffold's surface. The polymer fibers were electrospun directly onto copper grids.

2.3. Statistical Analysis

The statistical analysis of the obtained results was performed using one-way analysis of variance (ANOVA), with the Newman-Keuls post hoc test. A p value lower than 0.05 ($p<0.05$) was considered statistically significant.

Chapter III - Results and Discussion

3. Results and Discussion

3.1. Morphological characterization of the produced scaffolds

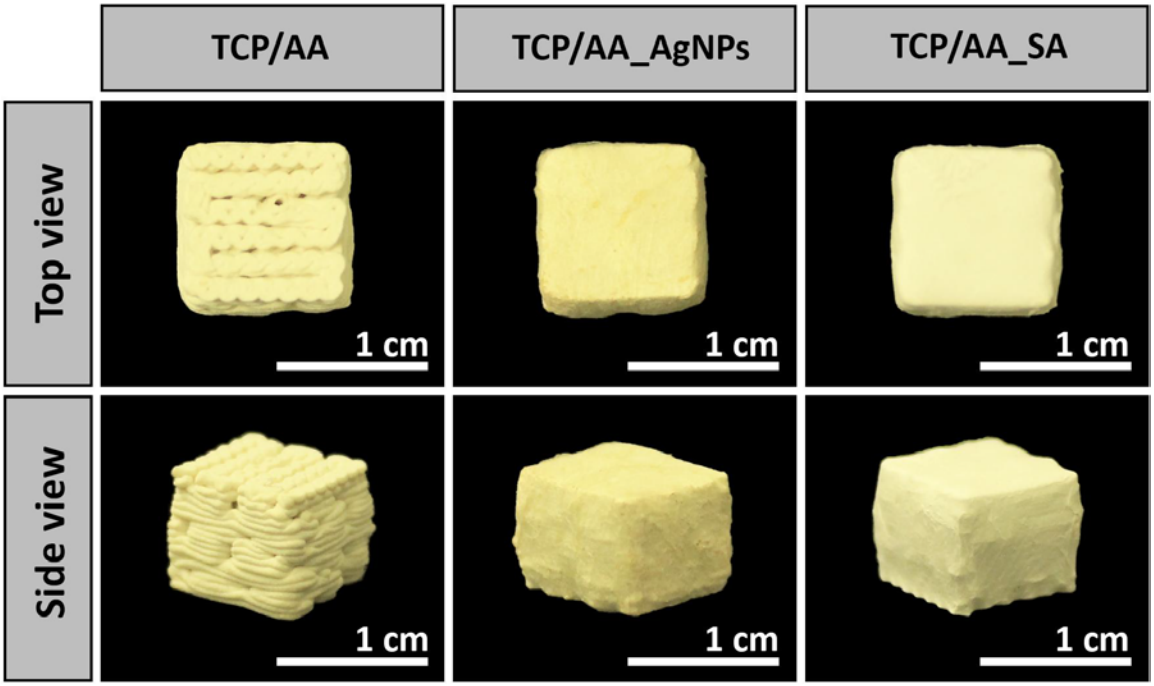

Figure 11. Macroscopic images of uncoated (TCP/AA) and coated (TCP/AA_AgNPs and TCP/AA_SA) scaffolds.

Herein, RP and ES techniques were used to produce scaffolds with the required properties to be used for improving bone tissue regeneration and simultaneously avoid biofilm formation at scaffolds' surface. While ES nanofibrous mesh acts as a support for enhancing cellular adhesion and also avoid biofilm formation, the scaffold produced by RP is responsible for assuring an appropriate structural support during bone regeneration [81]. Figure 11 presents the macroscopic images of coated and uncoated scaffolds. Through the analysis of these images, the morphologic variations between the control scaffold and the ES-coated scaffolds can be visualized. The uncoated scaffolds show an irregular and rough surface while those coated with nanofibers have a smooth surface. Moreover, the presence of silver ions in the constructs is emphasized by the yellow color present on the nanofibrous coating of TCP/AA_AgNPS (TEM images presented on figure 13), while TCP/AA_SA scaffolds present a white color.

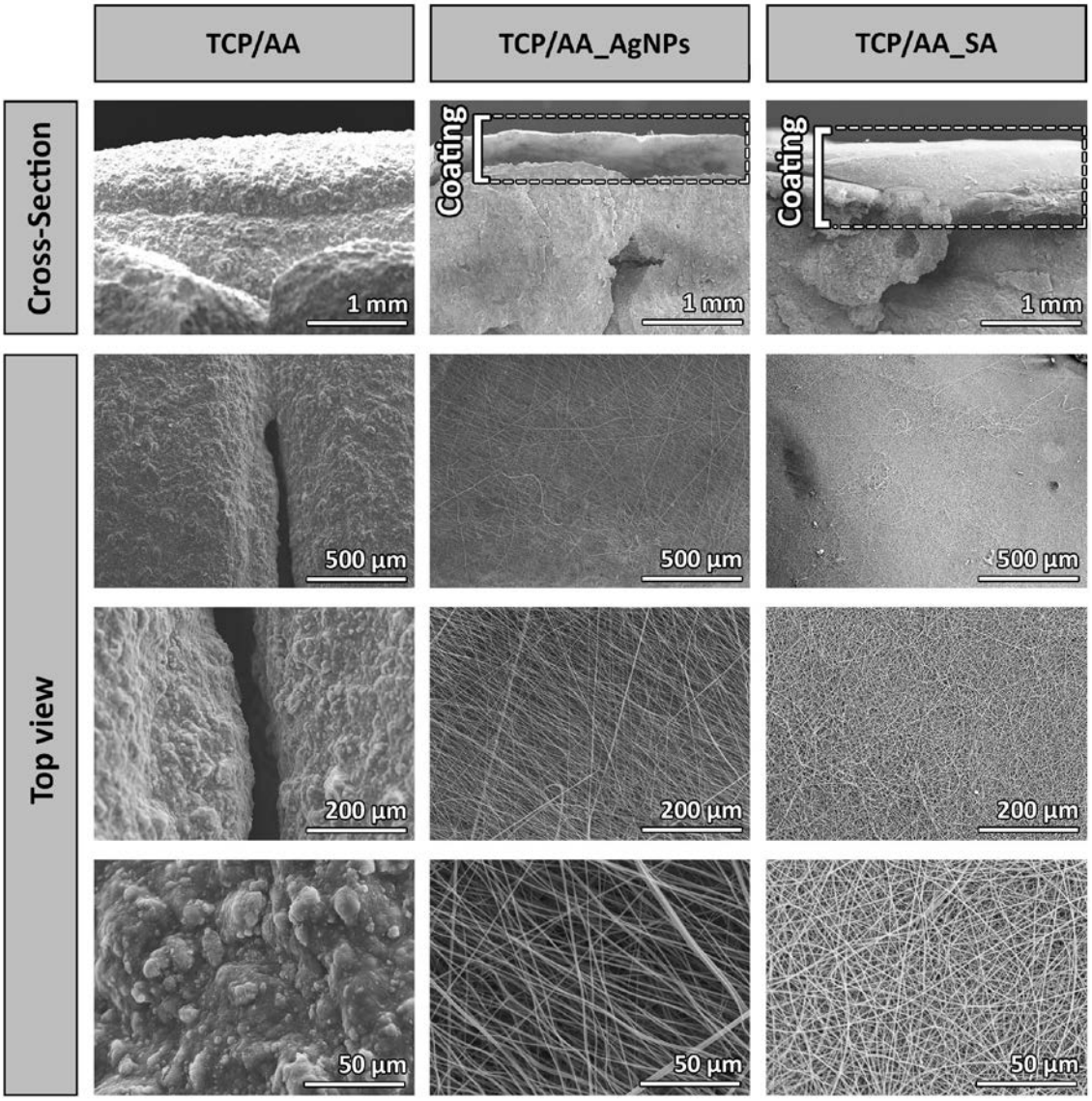

Figure 12. SEM images showing the morphology of uncoated (TCP/AA) and coated (TCP/AA_AgNPs and TCP/AA_SA) scaffolds using different magnifications.

The SEM images of the cross-sections of the produced scaffolds show two different layers, the outer sheet is comprised of an electrospun nanofibrous mesh and the inner one is composed of the RP produced structure (Figure 12). The average diameter of fibers that compose the TCP/AA_AgNPs nanofibrous coating was 604.9 ± 167.6 nm while those used to coat TCP/AA_SA scaffolds displayed an average diameter of 291.5 ± 77.2 nm. It is noteworthy that the diameters of the produced nanofibers are within the range of those of collagen fibrils found in natural ECM, which have average diameters of 50-500 nm [82]. These results clearly demonstrate that the produced 3D scaffolds present features that are compatible with cellular adhesion and proliferation, which are fundamental for their application in bone regeneration [83].

The presence of the AgNPs on the Gel/PCL coating of hybrid scaffolds was characterized by TEM (figure 13). The acquired images reveal that the AgNPs were successfully incorporated into the

GEL/PCL nanofibers without affecting fibers morphology. The size of the AgNPs was evaluated by DLS (figure 13) and an average size of 33.92 ± 0.393 nm was determined. Such results are in agreement with the data previously reported in the literature [74].

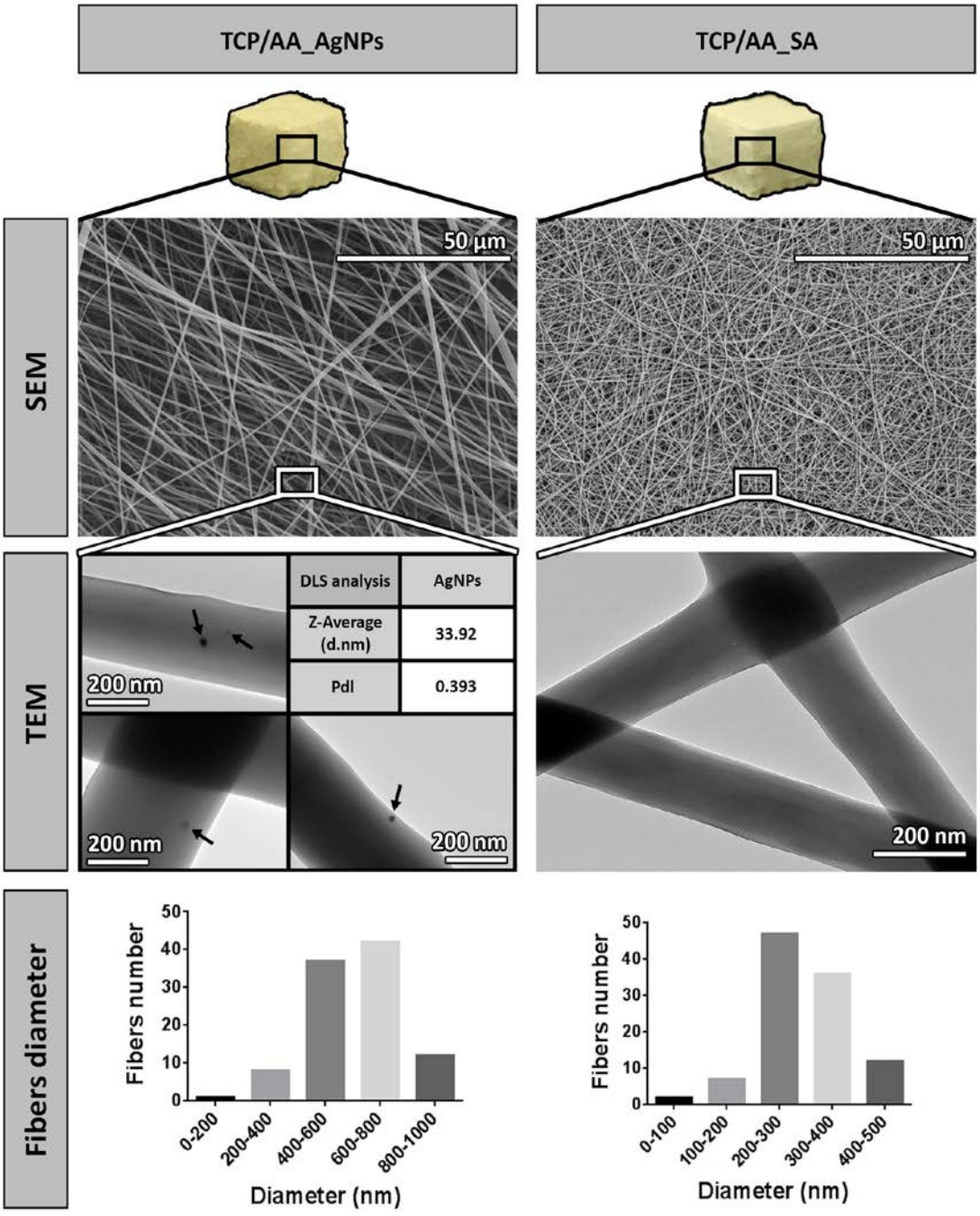

Figure 13. SEM and TEM analysis of the nanofibrous meshes present ate the surface of the scaffolds; AgNPs were noticed in the interior of GEL/PCL/AgNPs nanofibers; The nanofiber diameters distribution of TCP/AA_AgNPs and TCP/AA_SA nanofibrous mesh is also determined and displayed in the figure.

3.2. Characterization of the physicochemical properties of the scaffolds

3.2.1. ATR-FTIR analysis

ATR-FTIR analysis was performed to evaluate the composition of the different hybrid scaffolds. Figure 14A and B shows the ATR-FTIR spectra of raw materials and of the scaffolds produced by RP and then coated with nanofibrous meshes. The spectrum of the scaffold produced by RP contains, as expected, the typical bands of TCP and AA. The spectrum of TCP/AA scaffolds displays an intense absorption band at 1020 cm^{-1}, that was assigned to P=O stretch vibration, thus revealing the presence of the inorganic phosphate components from TCP [84]. Additionally, this spectrum also displays two major peaks between 1400 and 1600 cm^{-1}, belonging to the C=O stretching of the carboxylate group of pure AA. A stretching vibration that results from the O-H bonds of alginate is also observed in the range of 3000-3600 cm^{-1} [85].

On the other hand, ATR-FTIR spectra of GEL/PCL/AgNPs and GEL/PCL/SA nanofibers samples showed that both pre- and post-electrospun GEL presented the same peaks with only slight variations in their relative intensities. Such result shows that the TFE concentration used to produce the ES meshes did not affect GEL integrity [86]. Both GEL/PCL/AgNPs and GEL/PCL/SA spectra have bands at 1650 cm^{-1} (amide I), corresponding to the stretching vibrations of C-O bond, and at 1540 cm^{-1} (amide II), corresponding to the bending of N–H bond and the stretching of C–N bonds [87]. The amide I band at 1650 cm^{-1} can be attributed to a random coil and to a α-helix conformation of GEL [88]. In both nanofibrous membranes (GEL/PCL/AgNPs and GEL/PCL/SA) spectra, the characteristic peaks of PCL are observed at 2949 cm^{-1} (asymmetric CH_2 stretching), 2865 cm^{-1} (symmetric CH_2 stretching), 1727 cm^{-1} (carbonyl stretching), 1293 cm^{-1} (C-O and C-C stretching), 1240 cm^{-1} (asymmetric C-O-C stretching) and 1170 cm^{-1} (symmetric C-O-C stretching) [89].

In GEL/PCL/AgNPs scaffold spectrum, the major peaks of $AgNO_3$ are not visible due to the concentration of AgNPs used for ES membrane production. Nevertheless, the peak at 1334 cm^{-1} found in the GEL/PCL/AgNPs spectrum (characteristic of the NO_3^- ion in its free form) confirms the separation of NO_3^- from the Ag^+ ion, and thus the presence of the AgNPs in this electrospun coating [90].

Moreover, GEL/PCL/SA scaffold spectrum reveals that the relative intensity SA peaks were attenuated in comparison to the raw material. However, in the gathered spectrum it is possible to visualize C-H stretching vibrations in the range of 3037 and 3019 cm^{-1}, and a band at 1248 cm^{-1} assigned to O-H vibrations that are characteristic of SA. Further, the band observed between 1830 and 1750 cm^{-1} in the same spectrum can be assigned to the C=O vibration of SA. The C-C-C stretching of SA is assigned to the bands appearing at 1583, 1526, 1441, 1324, 1294, 1191, 1155 and 1030 cm^{-1} [91].

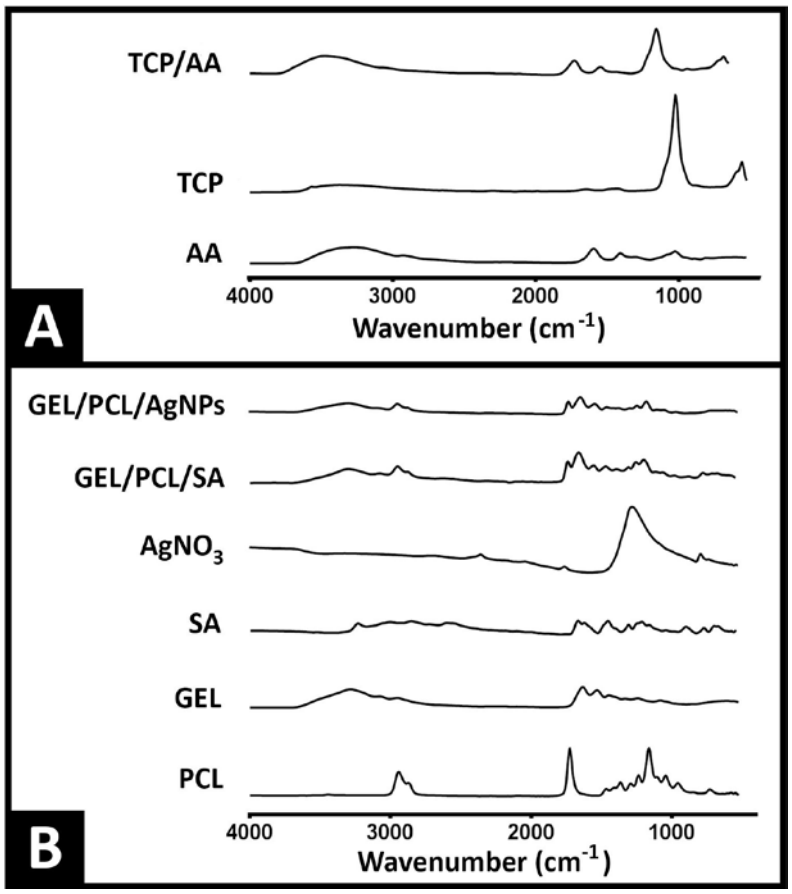

Figure 14. ATR-FTIR analysis of the produced 3D scaffolds and nanofibrous meshes. ATR-FTIR analysis of TCP/AA scaffolds (A); ATR-FTIR analysis of the TCP/AA_AgNPs and TCP/AA_SA nanofibrous meshes (B).

3.2.2. Energy dispersive spectroscopy analysis

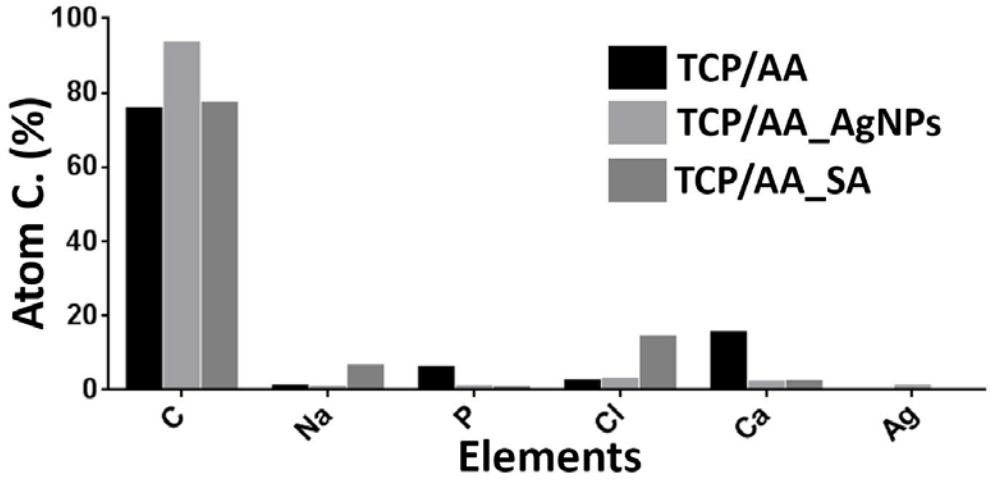

Figure 15. EDS analysis of the produced 3D scaffolds.

The elemental composition of the scaffolds was assessed also by EDS analysis as presented in figure 15. The control scaffold (TCP/AA) produced by RP shows the highest percentage of phosphorus and calcium ions since the TCP is its main component [76]. In turn, TCP/AA_AgNPs and

TCP/AA_SA scaffolds presented a lower concentration of these ions. This pattern is explained by the coating added to scaffolds' surface. TCP/AA_AgNPs and TCP/AA_SA scaffolds do not present TCP at their surface but an electrospun membrane of GEL/PCL, which is essentially composed of carbon elements. Additionally, despite the low concentrations of AgNPs used, the EDS analysis showed the presence of silver ions at the surface of TCP/AA_AgNPs hybrid scaffolds. Such confirm the results previously obtained through TEM analysis (figure 13).

3.2.3. Characterization of the mechanical properties of the produced scaffold

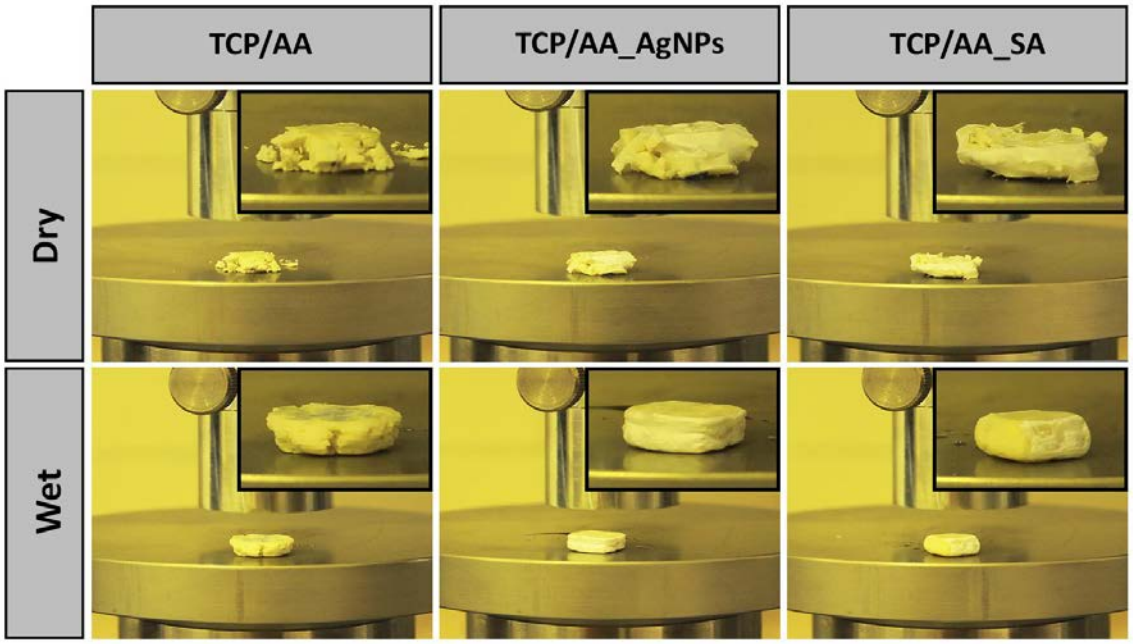

Figure 16. Macroscopic images of 3D hybrid scaffolds in dry and wet conditions during compression assay.

Scaffolds aimed for bone tissue engineering must have appropriate mechanical properties that are compatible with bone tissue regeneration at the site of implantation and also be able to support new tissue formation [92-94]. Herein, the mechanical behavior of the scaffolds was evaluated through compression assays as previously described elsewhere [76]. The resistance to compression and the Young's Modulus were determined in dry and wet conditions in order to mimic the physiological environment found *in vivo* (figure 17). The macroscopic images (figure 16) acquired at the end of the compressive strength test clearly show that the dry scaffolds when yield became more brittle, whereas the wet scaffolds do not crack and remain cohesive. In a dry state, the scaffolds showed a compressive strength of 60 MPa, while the Young Modulus was about 600 MPa. In wet conditions, all the produced scaffolds exhibited a compressive strength of ~15 MPa and a Young Modulus below 100 MPa. Since trabecular bone has a compressive strength comprehended between 2-20 MPa and a Young Modulus of 100-200 MPa it can be concluded that the produced scaffolds have suitable mechanical properties for bone regeneration [40]. Furthermore, it was possible to verify that the mechanical properties of the

two hybrid scaffolds produced were not significantly different among them, neither with the scaffolds used as a control. In addition, it was also verified that the presence of an electrospun polymeric mesh, at the surface of the 3D structures, did not affect scaffolds' mechanical properties. Therefore, both TCP/AA_AgNPs and TCP/AA_SA scaffolds are capable of reproducing the native bone matrix composition, mimicking the fine balance between the strength and elasticity found in trabecular bone tissue.

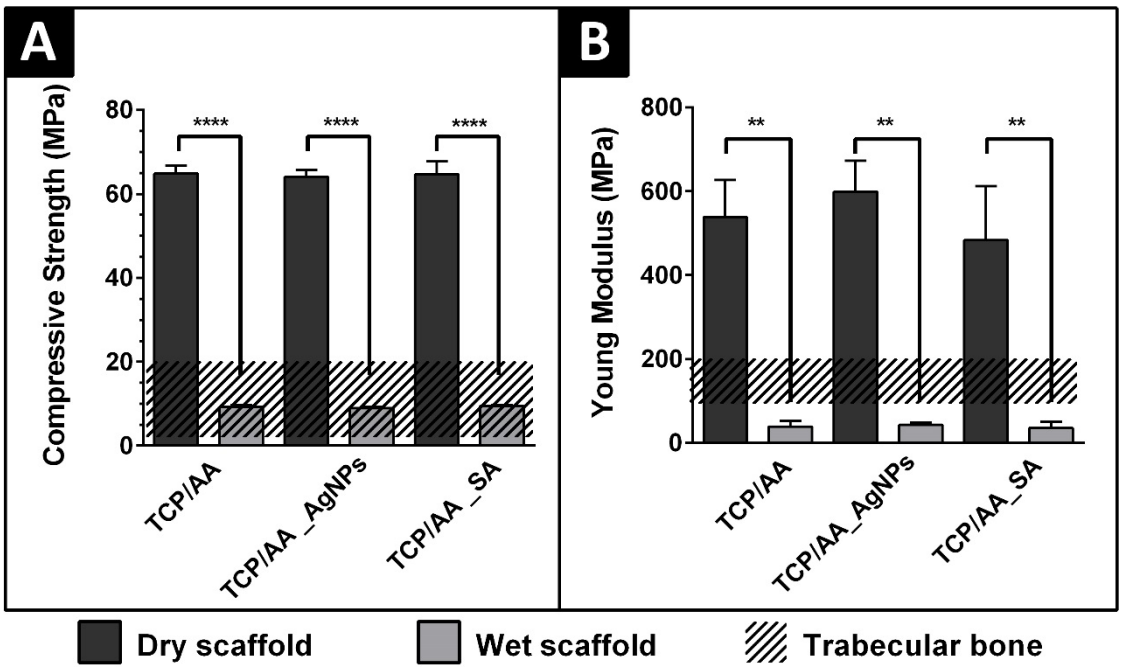

Figure 17. Characterization of the mechanical properties of the produced scaffolds. Characterization of the compressive strength (A) and young modulus (B) of the scaffolds, in dry and wet conditions. Statistical analysis of the results was performed using one-way ANOVA with Newman-Keuls post hoc test (**** $p \leq 0.0001$).

3.2.4. Evaluation of porosity of the scaffolds

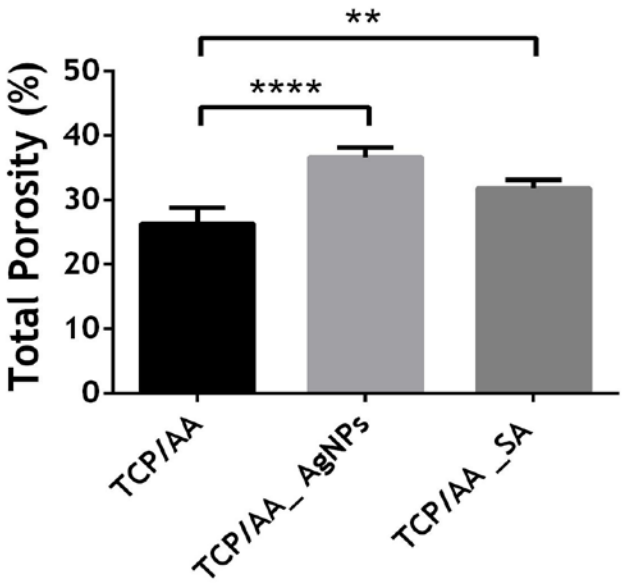

Figure 18. Characterization of the total porosity of the produced scaffolds. Statistical analysis of the results was performed using one-way ANOVA with Newman-Keuls post hoc test (** $p \leq 0.01$, **** $p \leq 0.0001$).

Scaffolds with a porous and interconnected structure, are highly desired to promote cellular attachment, proliferation as well as the exchange of nutrients and gases, features that are crucial for bone tissue engineering applications [95]. Figure 18 presents the data obtained in the porosity assays. As previously described in the literature, the scaffolds coated with nanofibrous meshes have higher values of porosity in comparison to the TCP/AA scaffolds used as control [96]. The TCP/AA_AgNPs scaffolds showed the highest values of porosity among all the produced scaffolds, which is in agreement with the higher number of void spaces available between nanofibers as observed in SEM images (figure 13). These high values of porosity allow cells to adhere and to migrate into the nanofibrous mesh (figure 24). Moreover, the total porosity of TCP/AA_AgNPs is around 40%, a value that is similar to that displayed by trabecular bone (50-90%). Based on total porosity results, it is possible to infer that the TCP/AA_AgNPs scaffolds are the most suitable to allow cell migration, proliferation as well as vascularization and gas exchange.

3.2.5. Evaluation of swelling profile of the scaffolds

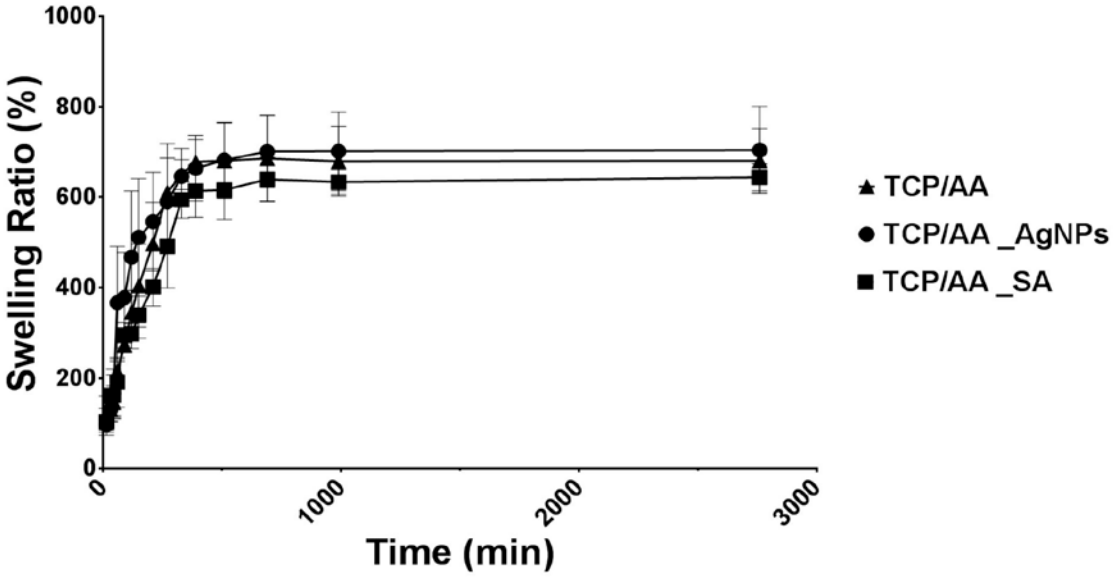

Figure 19. Characterization of the swelling profile of the produced scaffolds.

The swelling behavior and structural stability of scaffolds are critical properties for their application in tissue engineering area since the swelling profile affects both nutrients and cellular infiltration into the 3D scaffolds [97]. Samples showing a higher degree of swelling have a larger surface area/volume ratio, allowing a higher rate of cell growth and nutrients/gases exchanges. However, a controlled swelling behavior is fundamental for tissue engineering applications, since the continuous swelling would lead to the loss of mechanical integrity and will result in compressive strength to the surrounding tissue, causing pain to the patient [98]. The swelling profile of the produced scaffolds is presented in figure 19, and no noticeable differences were found between the swelling behavior of TCP/AA scaffolds and coated scaffolds (TCP/AA_AgNPS and TCP/AA_SA), after 2 days of immersion in culture medium at 37°C, no variation in the swelling state was noticed. Such demonstrates the structural stability of the produced scaffolds. As reported by others authors, AA is capable of absorbing large amounts of water by filling the void regions which can explain the obtained results [56] since the same amount of AA was used for scaffolds production.

3.2.6. Characterization of the biodegradation profile of the scaffolds

The biodegradation profile displayed by scaffolds is crucial for a long-term application of tissue-engineered cell-material constructs [99]. It is highly desired that materials present a degradation rate that is compatible with the period required for bone regeneration [99, 100]. Figure 20 shows that all the produced scaffolds presented a very similar degradation profile, along 7 days. Specifically, none of the scaffolds produced here lost more than 15% of its mass between day 4 and 7 of the assay, assuring the suitability of these scaffolds to be used in biomedical applications [31].

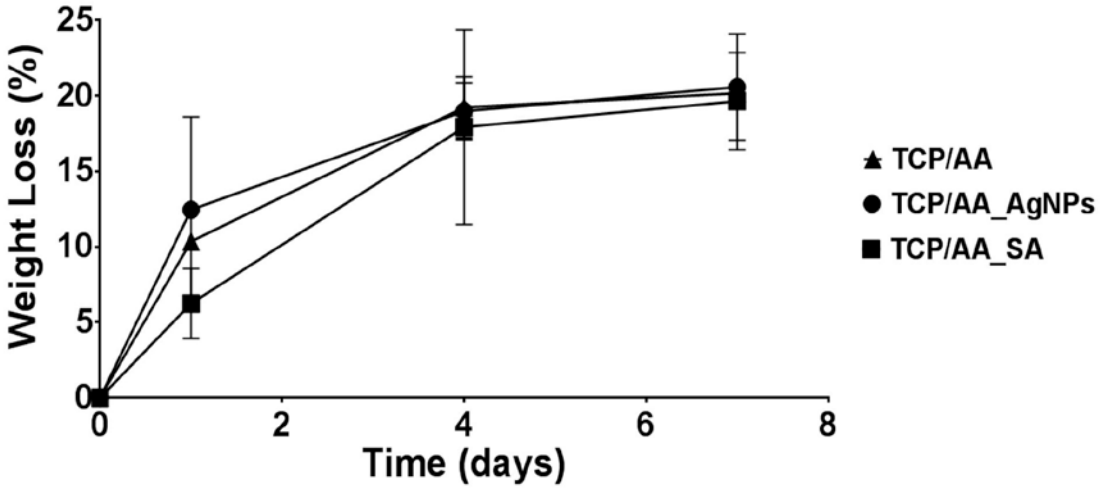

Figure 20. Characterization of the degradation profile of the produced scaffolds.

The degradation profile displayed by scaffolds is dependent on AA depolymerization, that occurs spontaneously through a process that involves the alkaline degradation of its glycosidic linkages [101]. In addition, TCP can also suffer cell-mediated degradation, being solubilized in contact with body fluids, while new bone tissue formation occurs [102]. On the other hand, the coating of TCP/AA_AgNPs and TCP/AA_SA scaffolds can suffer some degradation since GEL chains can be hydrolysed in contact with aqueous solutions [103, 104].

Among the two types of scaffolds produced here, the most porous TCP/AA_AgNPs scaffolds present the highest weight loss (Figure 20). Xu and colleagues have previously shown that metallic nanoparticles induce a thermal conductivity in the nanocomposites that enhance their degradation rate [105].

3.2.7. Biomineralization studies

The biomaterials biomineralization is a crucial event during bone regeneration. The hydroxyapatite crystals present in bone tissue are formed through a process known as biomineralization, that involves minerals nucleation and assembly in an organized fashion under the control of collagen fibers available in bone ECM [106]. Herein, the *in vitro* mineralization capacity of the composite scaffolds was studied by incubating them in SBF fluid during 4, 7 and 14 days. As can be observed in figure 21, the Ca/P ratio increased along time for all formulations. These results can be explained by the presence of TCP, known as a bioactive ceramic that is capable of inducing mineralization at the surface of the scaffolds, increase scaffolds biointegration, enhance their mechanical properties and ultimately the bone healing process [107]. Fradique *et al.* have previously reported that 3D scaffolds with higher content of TCP have an enhanced ability to become biomineralized [76]. Moreover, TCP/AA_AgNPs scaffolds revealed an increased biomineralization activity in comparison to other formulations (TCP/AA and TCP/AA_SA). Such behavior was already described in a previous study performed by Vulpoi

et al., where the silver-containing composite showed a higher percentage of calcium and phosphate ions deposition after their incubation for 21 days in SBF [108].

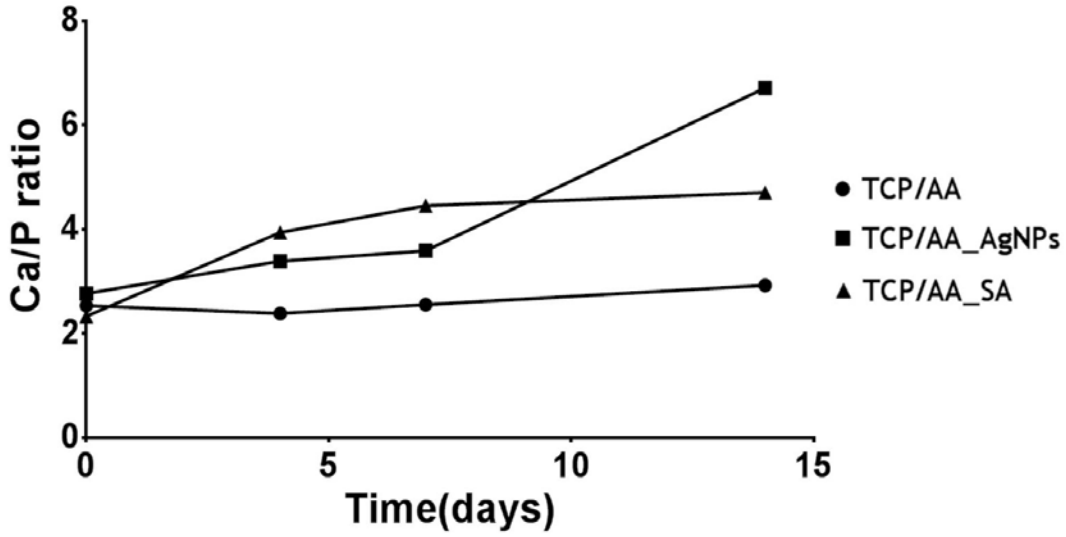

Figure 21. EDS analysis of the scaffolds after 4, 7 and 14 days in SBF.

3.3. Characterization of the biological properties of the scaffolds

3.3.1. Evaluation of cell viability and proliferation in contact with the scaffolds

Scaffolds aimed for bone regeneration cannot trigger any adverse effect on the host, specifically at the implantation site. Herein, the scaffolds cytotoxic profile was characterized through an MTT assay. It is known that the metabolic conversion of MTT, a yellow tetrazolium salt, to purple formazan crystals occurs in living cells and this conversion is proportional to the number of viable cells present in each well [109]. Due to their role in bone regeneration, human osteoblast (hOB) cells were used as a model to perform this assay [110].

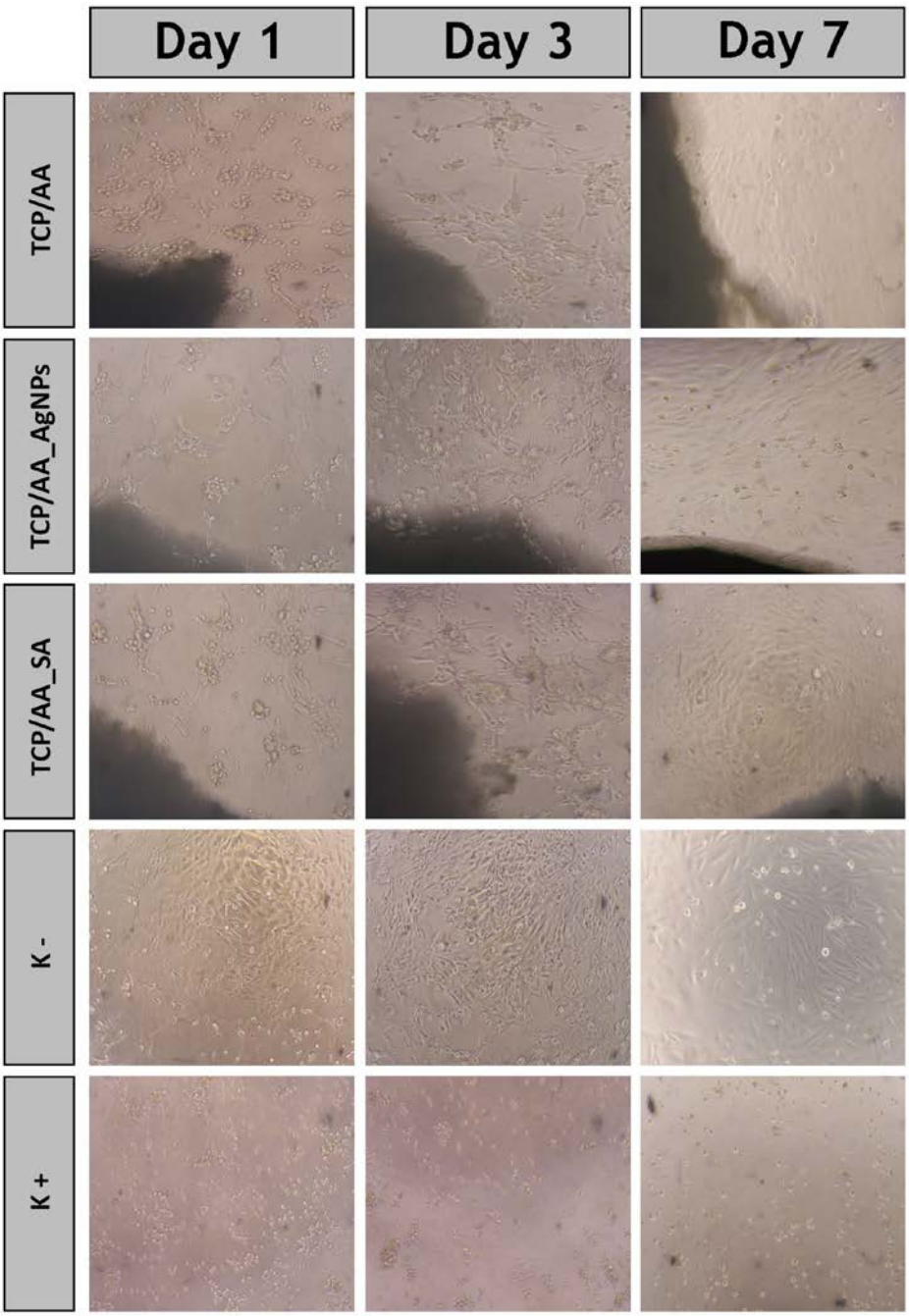

Figure 22. Microscopic images of human osteoblast cells seeded in the presence of scaffolds acquired after 1, 3 and 7 days. K- (negative control); K+ (positive control).

To further characterize cell behavior, optical microscopic images of the hOB cells in contact with scaffolds were collected after 1, 3 and 7 days of cells being seeded (figure 22). The data obtained from MTT assay (figure 23) revealed that the metabolic activity of hOB cells is similar to those of the negative control (where cells were grown in the absence of scaffolds) during the 7 days of analysis. Such result emphasizes the biocompatibility of the produced scaffolds. These results are in agreement with those obtained by Fradique and collaborators, who previously reported that scaffolds composed by TCP and sodium alginate provided an appropriate environment for cell adhesion and proliferation [76]. Moreover, other studies reported that

electrospun membranes composed of PCL and GEL are biocompatible and also promote cell adhesion and proliferation [111, 112].

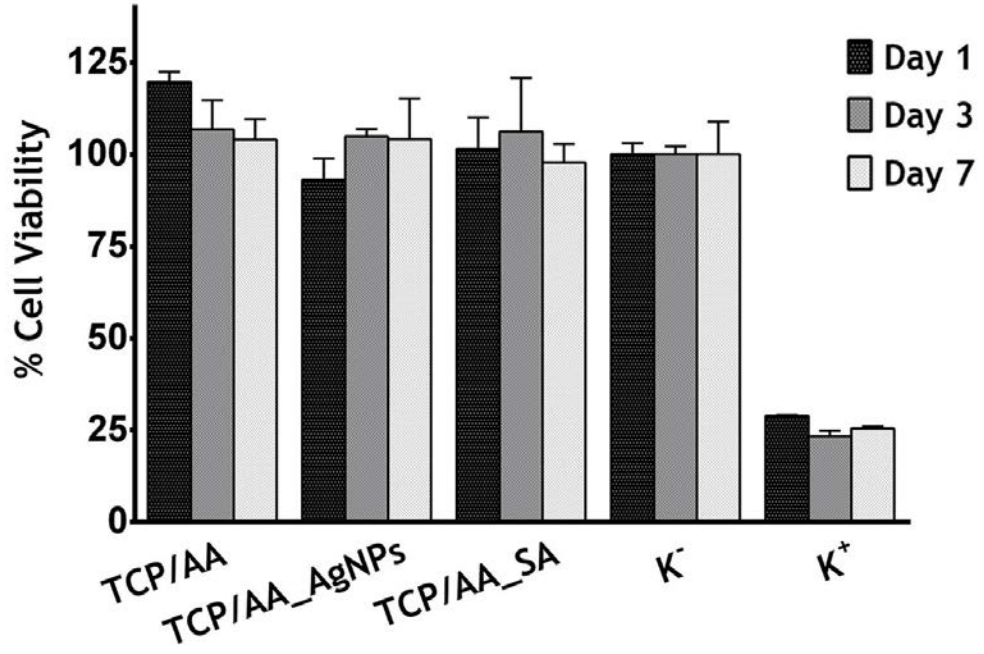

Figure 23. Evaluation of human osteoblasts cell viability when they cultured in the presence of scaffolds. Cultures were evaluated for 1, 3 and 7 days. (K+) positive control and (K–) negative control indicate dead and viable cells, respectively. Statistical analysis was performed using one-way ANOVA with Newman–Keuls test.

In order to characterize cellular adhesion and morphology scaffolds' surface, SEM images were also acquired (figure 24). Here, the initial cellular adhesion can be observed through the elongation of cells over the materials' surface. Such phenomenon can be attributed to the bioadhesive properties of ES nanofibrous meshes present at 3D scaffolds surface [113]. Also, the similarity between the nanofiber networks produced here and the collagen fibrils present at bone ECM may contribute for cellular attachment [114]. After 3 days of cell proliferation, it is possible to verify that cells are able to grow and spread over the 3D scaffolds surface. Among the formulations tested, it is clearly that the ones coated with the nanofiber meshes allowed the formation of a continuous cell layer.

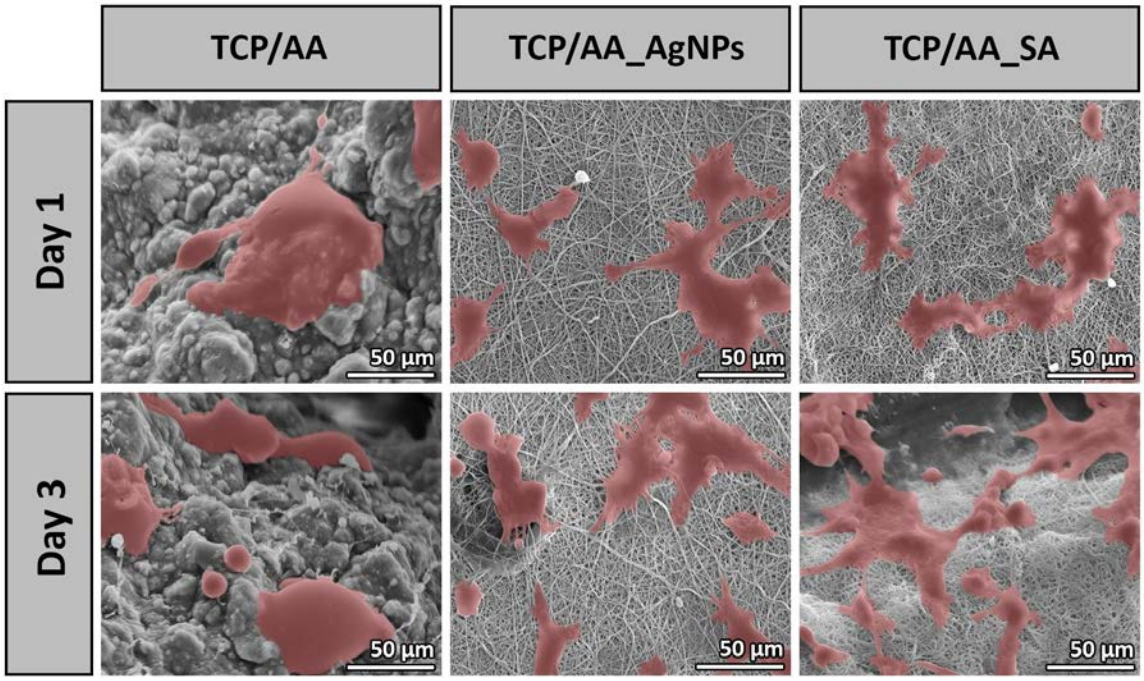

Figure 24. SEM micrographs images of osteoblasts morphology in the presence of the different scaffolds for 1 and 3 days.

3.3.2. Characterization of the bactericidal activity of the scaffolds

The majority of bone implants failure is associated with postoperative complications that have a high morbidity associated [115]. Nowadays, it is estimated that 65-80% of bacterial infections are caused by organisms that form biofilms on implants' surface, compromising their successful application [48]. To avoid such health problems, new approaches that involve scaffolds surface charge variation[116], addition/incorporation of metallic nanoparticles with bactericidal activity [90, 117], antibiotics or drugs [118], quaternary ammonium compounds [119, 120], and halogens, are currently being used (e.g. iodine) [121].

Herein, two different antibacterial agents, metallic nanoparticles (AgNPs) and SA, were loaded in the electrospun coatings to prevent the occurrence of bacterial contaminations at the implantation site.

S. aureus strain was used as a model bacterium to evaluate the bactericidal activity of the produced scaffolds. This strain was selected based on the reported cases where this microorganism has been associated with the biomaterial-related infections. *S. aureus* bacteraemias are found in 34% of prosthetic joints and in 7% of other orthopedic prostheses [46]. To determine the antimicrobial activity of the scaffolds the diameter of the inhibitory halos was measured and biofilm formation on scaffold's surface was evaluated by SEM analysis.

The TCP/AA_AgNPs hybrid scaffolds presented inhibitory halos of 8.53 mm ± 0.83 (figure 25A and B) and the absence of biofilm formation on their surface, for at least 5 days, was confirmed by SEM analysis (figure 26).

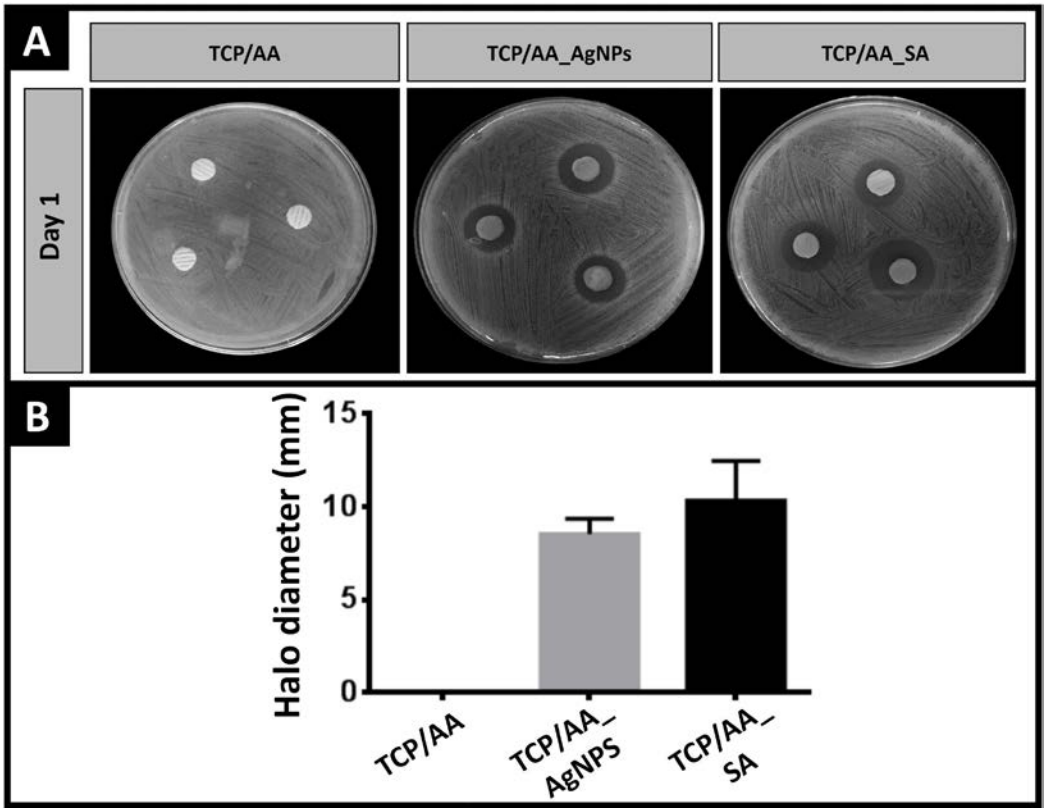

Figure 25. Evaluation of the antibacterial properties of the produced scaffolds. Macroscopic images of the inhibitory halo (A); Analysis of diameter of inhibitory halo obtained when scaffolds were in contact with S.aureus strain (B).

As previously reported in the literature, AgNPs have an enhanced activity against *S. aureus* strain, and can be used to promote a long-term antibacterial effect [90]. So far, the mechanism of action of AgNPs is not completely understood, however, it is believed that silver, mainly in its oxidized form (Ag^+), released from AgNPs, leads to the inactivation of DNA replication process [122]. In addition, silver ions have also the ability to interact with a variety of biomolecules within the cell, bacteria cell wall components and sulfhydryl groups of metabolic active enzymes [74, 123]. Such interactions can affect bacterial membrane permeability and different metabolic pathways of the microorganism.

On the other hand, the TCP/AA_SA hybrid scaffold displayed an inhibitory halo with a diameter of 10.34 mm ± 2.13 (figure 25A and B). Moreover, the SEM images showed no biofilm formation during 5 days (figure 26). Such results can be explained by the presence of SA which is a phenolic compound produced by plants that play an important role in several physiological processes, such as the induction of plant defense responses against pathogen attacks [63]. Furthermore, it is also responsible for the inhibition of cyclooxygenase (COX), known to be a key player in body's inflammatory response [124]. The antimicrobial activity of SA is not yet widely described in the literature, but there are some authors that have already demonstrated the effect of SA against the formation and growth of biofilms [125]. Lee *et al.* proposed that the free phenolic hydroxyl group of SA is able to kill bacteria, through a mechanism where the proton gradient present in

cells is destroyed [126]. Kupferwasser and collaborators showed that the treatment of infections caused by *S. aureus* with aspirin resulted in a significant reduction in bacterial densities at the target tissues [127]. Later, the same author clarified that SA interacts with important structural genes of S. aureus, namely alpha-hemolysin gene promoter (hla) and the fibronectin gene promoter, (fnbA). As a result, the transcriptional process is interrupted which decreases the staphylococcal malignancy [128].

Furthermore, the antimicrobial agents used in this study do not induce any microbial resistance, a common feature displayed by bacteria to other antimicrobial substances, such as methicillin and vancomycin [129].

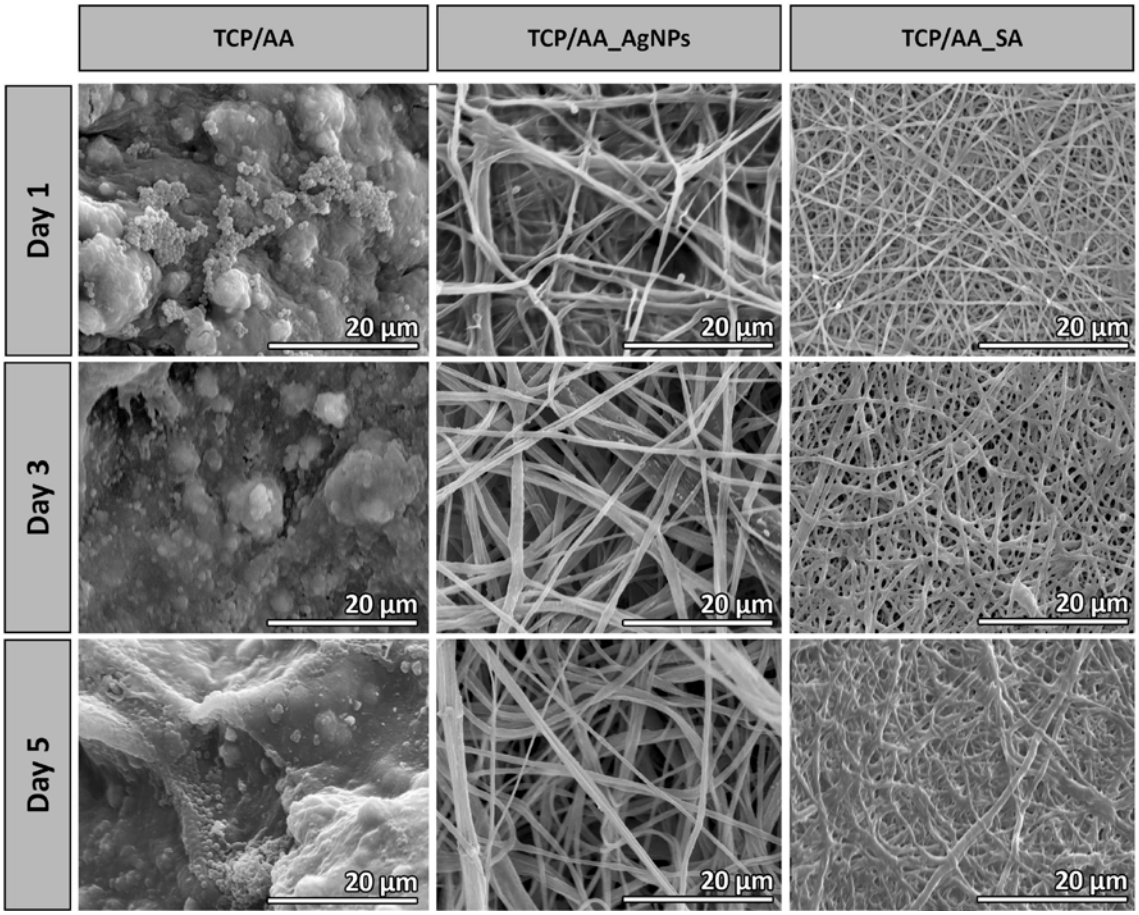

Figure 26. SEM images of scaffolds in contact with S.aureus after 1, 3 and 5 days.

Chapter IV - Conclusion and Future Trends

4. Conclusion and Future Perspectives

Bone tissue engineering has emerged as a promising area for the development of new therapeutic approaches to treat bone injuries that occur as a consequence of fractures, malformation, osteoporosis and tumors. Once bone tissue represents a biological nanocomposite composed of organic and inorganic components with a hierarchical structure ranging from the micro to the nanoscale. Various approaches have been used to produce 3D structures that are able to reproduce bone native properties. Therefore, in this study, two types of 3D hybrid scaffolds produced by RP and coated with nanofibrous meshes (loaded with antimicrobial agents) were developed in order to enhance the cellular adhesion, migration as well as assure antimicrobial properties to the final scaffold.

As expected, coated and uncoated scaffolds displayed similar swelling, biodegradation profiles and biomineralization activity. Besides, in wet state, all the produced scaffolds exhibited a compressive strength of ~15 MPa and a Young Modulus below 100 MPa. Such values are compatible with their application in trabecular bone regeneration, since trabecular bone has a compressive strength comprehended between 0.5-15 MPa and a Young Modulus of 100-200 MPa.

On the other hand, TCP/AA_AgNPs and TCP/AA_SA hybrid scaffolds promoted an effective cell adhesion at their surfaces, which is fundamental for triggering the synthesis of new bone tissue. In addition, the scaffolds were also able to prevent biofilm formation on their surface. Furthermore, the antimicrobial agents used in this study do not induce any antimicrobial resistance, which is crucial for long-term applications.

Hereafter, these hybrid scaffolds will be implanted in animal models in order to evaluate scaffolds performance in bone regeneration. Furthermore, the incorporation of bioactive molecules, such as bone morphogenic proteins can also be hypothesized as a future perspective of this work. Both techniques adopted here are simple, effective and cheap. Therefore, the translation of the production method developed here to an industrial level can be envisioned.

Chapter V - Bibliography

5. Bibliography

1. D. Sommerfeldt and C. Rubin, *European Spine Journal*, 2001, **10**, S86-S95.
2. J. R. Porter, T. T. Ruckh and K. C. Popat, *Biotechnology Progress*, 2009, **25**, 1539-1560.
3. J.-H. Jang, O. Castano and H.-W. Kim, *Advanced drug delivery reviews*, 2009, **61**, 1065-1083.
4. A. Oryan, S. Monazzah and A. Bigham-Sadegh, *Biomedical and environmental sciences*, 2015, **28**, 57-71.
5. M. Doblaré, J. Garcıa and M. Gómez, *Engineering Fracture Mechanics*, 2004, **71**, 1809-1840.
6. A. J. Salgado, O. P. Coutinho and R. L. Reis, *Macromolecular bioscience*, 2004, **4**, 743-765.
7. J. Kular, J. Tickner, S. M. Chim and J. Xu, *Clinical biochemistry*, 2012, **45**, 863-873.
8. B. Clarke, *Clinical journal of the American Society of Nephrology*, 2008, **3**, S131-S139.
9. A. R. Costa-Pinto, R. L. Reis and N. M. Neves, *Tissue Engineering Part B: Reviews*, 2011, **17**, 331-347.
10. E. Mackie, *The international journal of biochemistry & cell biology*, 2003, **35**, 1301-1305.
11. S. H. Ralston, *Medicine*, 2005, **33**, 58-60.
12. S. J. Morrison and D. T. Scadden, *Nature*, 2014, **505**, 327-334.
13. X. Li, L. Wang, Y. Fan, Q. Feng, F. Z. Cui and F. Watari, *Journal of Biomedical Materials Research Part A*, 2013, **101**, 2424-2435.
14. P. Jayakumar and L. Di Silvio, *Proceedings of the Institution of Mechanical Engineers, Part H: Journal of Engineering in Medicine*, 2010, **224**, 1415-1440.
15. P. A. Downey and M. I. Siegel, *Physical therapy*, 2006, **86**, 77-91.
16. G. E. Sroga and D. Vashishth, *Current osteoporosis reports*, 2012, **10**, 141-150.
17. S. Viguet-Carrin, P. Garnero and P. Delmas, *Osteoporosis International*, 2006, **17**, 319-336.
18. M. J. Olszta, X. Cheng, S. S. Jee, R. Kumar, Y.-Y. Kim, M. J. Kaufman, E. P. Douglas and L. B. Gower, *Materials Science and Engineering: R: Reports*, 2007, **58**, 77-116.
19. A. R. Shrivats, M. C. McDermott and J. O. Hollinger, *Drug discovery today*, 2014, **19**, 781-786.
20. J. Klein-Nulend, P. J. Nijweide and E. H. Burger, *Current osteoporosis reports*, 2003, **1**, 5-10.
21. C. J. Damien and J. R. Parsons, *Journal of Applied Biomaterials*, 1991, **2**, 187-208.
22. M. M. Cohen Jr, *American journal of medical genetics part A*, 2006, **140**, 2646-2706.
23. L. J. Raggatt and N. C. Partridge, *Journal of Biological Chemistry*, 2010, **285**, 25103-25108.
24. N. Rucci, *Clinical cases in mineral and bone metabolism*, 2008, **5**, 49-56.
25. V. I. Sikavitsas, J. S. Temenoff and A. G. Mikos, *Biomaterials*, 2001, **22**, 2581-2593.
26. P. J. Marie, *Cellular and Molecular Life Sciences*, 2015, **72**, 1347-1361.
27. D. P. Lew and F. A. Waldvogel, *The Lancet*, 2004, **364**, 369-379.
28. F. Shapiro, in *Pediatric Orthopedic Deformities, Volume 1*, Springer, 2016, pp. 411-504.

29. S. L. Teitelbaum, *Science*, 2000, **289**, 1504-1508.
30. T. Willson, S. D. Nelson, J. Newbold, R. E. Nelson and J. LaFleur, *Clinical epidemiology*, 2015, **7**, 65.
31. L. Claes, S. Recknagel and A. Ignatius, *Nature reviews. Rheumatology*, 2012, **8**, 133-143.
32. G. A. Rodan and T. J. Martin, *Science*, 2000, **289**, 1508-1514.
33. S. H. Ralston, *New England Journal of Medicine*, 2013, **368**, 644-650.
34. N. H. Mast and D. Horwitz, *Operative Techniques in Orthopaedics*, 2002, **12**, 232-241.
35. M. Fröhlich, W. L. Grayson, D. Marolt, J. M. Gimble, N. Kregar-Velikonja and G. Vunjak-Novakovic, *Tissue Engineering Part A*, 2009, **16**, 179-189.
36. U. Kneser, D. Schaefer, E. Polykandriotis and R. Horch, *Journal of cellular and molecular medicine*, 2006, **10**, 7-19.
37. J. R. Woodard, A. J. Hilldore, S. K. Lan, C. Park, A. W. Morgan, J. A. C. Eurell, S. G. Clark, M. B. Wheeler, R. D. Jamison and A. J. W. Johnson, *Biomaterials*, 2007, **28**, 45-54.
38. X. Liu and P. X. Ma, *Annals of biomedical engineering*, 2004, **32**, 477-486.
39. M. N. Collins and C. Birkinshaw, *Carbohydrate Polymers*, 2013, **92**, 1262-1279.
40. S. Bose, M. Roy and A. Bandyopadhyay, *Trends in biotechnology*, 2012, **30**, 546-554.
41. T. Dvir, B. P. Timko, D. S. Kohane and R. Langer, *Nature nanotechnology*, 2011, **6**, 13-22.
42. F. J. O'brien, *Materials Today*, 2011, **14**, 88-95.
43. M. Castilho, J. Rodrigues, I. Pires, B. Gouveia, M. Pereira, C. Moseke, J. Groll, A. Ewald and E. Vorndran, *Biofabrication*, 2015, **7**, 015004.
44. J. Henkel, M. A. Woodruff, D. R. Epari, R. Steck, V. Glatt, I. C. Dickinson, P. F. M. Choong, M. A. Schuetz and D. W. Hutmacher, *Bone Res*, 2013, **3**, 216-248.
45. R. Murugan and S. Ramakrishna, *Tissue engineering*, 2006, **12**, 435-447.
46. D. Campoccia, L. Montanaro and C. R. Arciola, *Biomaterials*, 2013, **34**, 8018-8029.
47. R. Kargupta, S. Bok, C. M. Darr, B. D. Crist, K. Gangopadhyay, S. Gangopadhyay and S. Sengupta, *Wiley Interdisciplinary Reviews: Nanomedicine and Nanobiotechnology*, 2014, **6**, 475-495.
48. C. A. Fux, P. Stoodley, L. Hall-Stoodley and J. W. Costerton, *Expert review of anti-infective therapy*, 2003, **1**, 667-683.
49. B. Narasimhan, D. Belsare, D. Pharande, V. Mourya and A. Dhake, *European journal of medicinal chemistry*, 2004, **39**, 827-834.
50. M. Schieker, H. Seitz, I. Drosse, S. Seitz and W. Mutschler, *European journal of trauma*, 2006, **32**, 114-124.
51. S. C. Cox, J. A. Thornby, G. J. Gibbons, M. A. Williams and K. K. Mallick, *Materials Science and Engineering: C*, 2015, **47**, 237-247.
52. G. Chiara, F. Letizia, F. Lorenzo, S. Edoardo, S. Diego, S. Stefano, B. Eriberto and Z. Barbara, *International journal of molecular sciences*, 2012, **13**, 737-757.
53. H. A. Awad, M. Q. Wickham, H. A. Leddy, J. M. Gimble and F. Guilak, *Biomaterials*, 2004, **25**, 3211-3222.
54. U. Wegst and M. Ashby, *Philosophical Magazine*, 2004, **84**, 2167-2186.

55. M. P. Carvalho, E. C. Costa, S. P. Miguel and I. J. Correia, *Carbohydrate Polymers*, 2016.
56. J. Valente, T. Valente, P. Alves, P. Ferreira, A. Silva and I. Correia, *Materials science & engineering. C, Materials for biological applications*, 2012, **32**, 2596-2603.
57. B. M. Holzapfel, J. C. Reichert, J.-T. Schantz, U. Gbureck, L. Rackwitz, U. Nöth, F. Jakob, M. Rudert, J. Groll and D. W. Hutmacher, *Advanced drug delivery reviews*, 2013, **65**, 581-603.
58. B. E. Christensen, *Carbohydrate Chemistry: Chemical and Biological Approaches*, 2011, **37**, 227-258.
59. A. D. Augst, H. J. Kong and D. J. Mooney, *Macromolecular bioscience*, 2006, **6**, 623-633.
60. L. Polo-Corrales, M. Latorre-Esteves and J. E. Ramirez-Vick, *Journal of nanoscience and nanotechnology*, 2014, **14**, 15.
61. V. Karageorgiou and D. Kaplan, *Biomaterials*, 2005, **26**, 5474-5491.
62. L. Estevinho, A. P. Pereira, L. Moreira, L. G. Dias and E. Pereira, *Food and Chemical Toxicology*, 2008, **46**, 3774-3779.
63. B. Prithiviraj, H. Bais, T. Weir, B. Suresh, E. Najarro, B. Dayakar, H. Schweizer and J. Vivanco, *Infection and immunity*, 2005, **73**, 5319-5328.
64. M. C. Verberne, N. Brouwer, F. Delbianco, H. J. Linthorst, J. F. Bol and R. Verpoorte, *Phytochemical Analysis*, 2002, **13**, 45-50.
65. J. Griffin, R. Delgado-Rivera, S. Meiners and K. E. Uhrich, *Journal of Biomedical Materials Research Part A*, 2011, **97**, 230-242.
66. J. R. Morones, J. L. Elechiguerra, A. Camacho, K. Holt, J. B. Kouri, J. T. Ramirez and M. J. Yacaman, *Nanotechnology*, 2005, **16**, 2346-2353.
67. V. Singh and A. Tiwari, *International Journal of Current Microbiology and Applied Sciences*, 2015, **4**, 5-10.
68. A. Martins, S. Chung, A. J. Pedro, R. A. Sousa, A. P. Marques, R. L. Reis and N. M. Neves, *Journal of tissue engineering and regenerative medicine*, 2009, **3**, 37-42.
69. W. Teo and S. Ramakrishna, *Nanotechnology*, 2006, **17**, R89.
70. Z.-M. Huang, Y.-Z. Zhang, M. Kotaki and S. Ramakrishna, *Composites science and technology*, 2003, **63**, 2223-2253.
71. Q. P. Pham, U. Sharma and A. G. Mikos, *Tissue engineering*, 2006, **12**, 1197-1211.
72. M. E. Frohbergh, A. Katsman, G. R. Botta, P. Lazarovici, C. L. Schauer, U. G. K. Wegst and P. I. Lelkes, *Biomaterials*, 2012, **33**, 9167-9178.
73. M. G. Yeo and G. H. Kim, *Chemistry of Materials*, 2011, **24**, 903-913.
74. E. Silva, S. M. Saraiva, S. P. Miguel and I. J. Correia, *Journal of Nanoparticle Research*, 2014, **16**, 1-13.
75. F. Yang, S. Xia, C. Tan and X. Zhang, *European Food Research and Technology*, 2013, **237**, 467-479.
76. R. Fradique, T. R. Correia, S. P. Miguel, K. D. de Sa, D. R. Figueira, A. G. Mendonça and I. J. Correia, *Journal of Materials Science-Materials in Medicine*, 2016, **27**, 1-14.

77. G. S. Diogo, V. M. Gaspar, I. R. Serra, R. Fradique and I. J. Correia, *Biofabrication*, 2014, **6**, 025001.
78. A. L. Torres, V. M. Gaspar, I. R. Serra, G. S. Diogo, R. Fradique, A. P. Silva and I. J. Correia, *Materials science & engineering. C, Materials for biological applications*, 2013, **33**, 4460-4469.
79. S. Jalota, S. B. Bhaduri and A. C. Tas, *Materials Science and Engineering: C*, 2008, **28**, 129-140.
80. T. Kokubo and H. Takadama, *Biomaterials*, 2006, **27**, 2907-2915.
81. G. Kim, J. Son, S. Park and W. Kim, *Macromol Rapid Comm*, 2008, **29**, 1577-1581.
82. J. Zhao, W. Han, H. Chen, M. Tu, R. Zeng, Y. Shi, Z. Cha and C. Zhou, *Carbohydrate Polymers*, 2011, **83**, 1541-1546.
83. D. Han and P.-I. Gouma, *Nanomedicine: Nanotechnology, Biology and Medicine*, 2006, **2**, 37-41.
84. C. F. Santos, A. P. Silva, L. Lopes, I. Pires and I. J. Correia, *Materials science & engineering. C, Materials for biological applications*, 2012, **32**, 1293-1298.
85. H. Daemi and M. Barikani, *Sci Iran*, 2012, **19**, 2023-2028.
86. S. Panzavolta, M. Gioffre, M. L. Focarete, C. Gualandi, L. Foroni and A. Bigi, *Acta biomaterialia*, 2011, **7**, 1702-1709.
87. D. M. Hashim, Y. B. C. Man, R. Norakasha, M. Shuhaimi, Y. Salmah and Z. A. Syahariza, *Food Chem*, 2010, **118**, 856-860.
88. K. Sisson, C. Zhang, M. C. Farach-Carson, D. B. Chase and J. F. Rabolt, *Biomacromolecules*, 2009, **10**, 1675-1680.
89. T. R. Correia, B. P. Antunes, P. H. Castilho, J. C. Nunes, M. T. P. de Amorim, I. C. Escobar, J. A. Queiroz, I. J. Correia and A. M. Morao, *Separation and Purification Technology*, 2013, **112**, 20-25.
90. E. Marsich, F. Bellomo, G. Turco, A. Travan, I. Donati and S. Paoletti, *Journal of Materials Science-Materials in Medicine*, 2013, **24**, 1799-1807.
91. S. Suresh, S. Gunasekaran and S. Srinivasan, *Spectrochimica acta. Part A, Molecular and biomolecular spectroscopy*, 2014, **132**, 130-141.
92. A. S. Mistry and A. G. Mikos, *Advances in biochemical engineering/biotechnology*, 2005, **94**, 1-22.
93. B. D. Porter, J. B. Oldham, S. L. He, M. E. Zobitz, R. G. Payne, K. N. An, B. L. Currier, A. G. Mikos and M. J. Yaszemski, *Journal of biomechanical engineering*, 2000, **122**, 286-288.
94. R. C. Thomson, M. J. Yaszemski, J. M. Powers and A. G. Mikos, *Journal of biomaterials science. Polymer edition*, 1995, **7**, 23-38.
95. I. R. Serra, R. Fradique, M. C. Vallejo, T. R. Correia, S. P. Miguel and I. J. Correia, *Materials Science and Engineering C: Materials for Biological Applications*, 2015, **55**, 592-604.
96. S. H. Park, T. G. Kim, H. C. Kim, D. Y. Yang and T. G. Park, *Acta biomaterialia*, 2008, **4**, 1198-1207.

97. N. Shanmugasundaram, P. Ravichandran, P. N. Reddy, N. Ramamurty, S. Pal and K. P. Rao, *Biomaterials*, 2001, **22**, 1943-1951.
98. Z. Li, H. R. Ramay, K. D. Hauch, D. Xiao and M. Zhang, *Biomaterials*, 2005, **26**, 3919-3928.
99. J. E. Dumas, E. M. Prieto, K. J. Zienkiewicz, T. Guda, J. C. Wenke, J. Bible, G. E. Holt and S. A. Guelcher, *Tissue Engineering Part A*, 2014, **20**, 115-129.
100. A. R. Amini, C. T. Laurencin and S. P. Nukavarapu, *Critical reviews in biomedical engineering*, 2012, **40**, 363-408.
101. B. E. Christensen, in *Carbohydrate Chemistry: Chemical and Biological Approaches*, 2011, vol. 37, pp. 227-258.
102. M. Kamitakahara, C. Ohtsuki and T. Miyazaki, *Journal of biomaterials applications*, 2008, **23**, 197-212.
103. V. G. Kadajji and G. V. Betageri, *Polymers-Basel*, 2011, **3**, 1972-2009.
104. J. Zhu and R. E. Marchant, *Expert review of medical devices*, 2011, **8**, 607-626.
105. X. Xu, Q. Yang, Y. Wang, H. Yu, X. Chen and X. Jing, *European polymer journal*, 2006, **42**, 2081-2087.
106. M. Yang, G. Zhou, H. Castano-Izquierdo, Y. Zhu and C. Mao, *Journal of Biomedical Nanotechnology*, 2015, **11**, 447-456.
107. J. Franco, P. Hunger, M. E. Launey, A. P. Tomsia and E. Saiz, *Acta biomaterialia*, 2010, **6**, 218-228.
108. A. Vulpoi, V. Simon, H. Ylänen and S. Simon, *Journal of Composite Materials*, 2014, **48**, 63-70.
109. J. van Meerloo, G. J. Kaspers and J. Cloos, *Methods in molecular biology*, 2011, **731**, 237-245.
110. D. W. Dempster and L. G. Raisz, in *Nutrition and Bone Health*, Springer, 2015, pp. 37-56.
111. S. Gautam, A. K. Dinda and N. C. Mishra, *Materials science & engineering. C, Materials for biological applications*, 2013, **33**, 1228-1235.
112. J. Xue, M. He, H. Liu, Y. Niu, A. Crawford, P. D. Coates, D. Chen, R. Shi and L. Zhang, *Biomaterials*, 2014, **35**, 9395-9405.
113. Y. Wang, W. Zhang, J. Yuan and J. Shen, *Materials science & engineering. C, Materials for biological applications*, 2016, **59**, 30-34.
114. D. R. Nisbet, J. S. Forsythe, W. Shen, D. I. Finkelstein and M. K. Horne, *Journal of biomaterials applications*, 2009, **24**, 7-29.
115. D. Campoccia, L. Montanaro and C. R. Arciola, *Biomaterials*, 2006, **27**, 2331-2339.
116. B. P. Antunes, A. F. Moreira, V. M. Gaspar and I. J. Correia, *Carbohydrate Polymers*, 2015, **130**, 104-112.
117. M. Yazdimamaghani, D. Vashaee, S. Assefa, K. J. Walker, S. V. Madihally, G. A. Kohler and L. Tayebi, *Journal of Biomedical Nanotechnology*, 2014, **10**, 911-931.
118. W. Li, P. Nooeaid, J. A. Roether, D. W. Schubert and A. R. Boccaccini, *Journal of the European Ceramic Society*, 2014, **34**, 505-514.

119. C. Yao, X. Li, K. Neoh, Z. Shi and E. Kang, *Journal of Membrane Science*, 2008, **320**, 259-267.
120. L. Cheng, M. D. Weir, P. Limkangwalmongkol, G. D. Hack, H. H. Xu, Q. Chen and X. Zhou, *Journal of biomedical materials research. Part B, Applied biomaterials*, 2012, **100**, 726-734.
121. M. Shin, H. Abukawa, M. J. Troulis and J. P. Vacanti, *Journal of biomedical materials research. Part A*, 2008, **84**, 702-709.
122. I. Sondi and B. Salopek-Sondi, *Journal of colloid and interface science*, 2004, **275**, 177-182.
123. J. S. Kim, E. Kuk, K. N. Yu, J. H. Kim, S. J. Park, H. J. Lee, S. H. Kim, Y. K. Park, Y. H. Park, C. Y. Hwang, Y. K. Kim, Y. S. Lee, D. H. Jeong and M. H. Cho, *Nanomedicine: Nanotechnology, Biology and Medicine*, 2007, **3**, 95-101.
124. C. L. Romanò, M. Toscano, D. Romanò and L. Drago, *Journal of Chemotherapy*, 2013, **25**, 67-80.
125. M. A. Alem and L. J. Douglas, *Antimicrobial agents and chemotherapy*, 2004, **48**, 41-47.
126. I. Y. Lee, T. D. Gruber, A. Samuels, M. Yun, B. Nam, M. Kang, K. Crowley, B. Winterroth, H. I. Boshoff and C. E. Barry, 3rd, *Bioorganic & medicinal chemistry*, 2013, **21**, 114-126.
127. L. I. Kupferwasser, M. R. Yeaman, S. M. Shapiro, C. C. Nast, P. M. Sullam, S. G. Filler and A. S. Bayer, *Circulation*, 1999, **99**, 2791-2797.
128. L. I. Kupferwasser, M. R. Yeaman, C. C. Nast, D. Kupferwasser, Y. Q. Xiong, M. Palma, A. L. Cheung and A. S. Bayer, *The Journal of clinical investigation*, 2003, **112**, 222-233.
129. S. Gardete and A. Tomasz, *The Journal of clinical investigation*, 2014, **124**, 2836-2840.

Appendix

- Fradique, R., Correia, T. R., Miguel, S. P., *de Sá, K. D.*, Figueira, D. R., Mendonça, A. G., & Correia, I. J. (2016). Production of new 3D scaffolds for bone tissue regeneration by rapid prototyping. *Journal of Materials Science: Materials in Medicine*, *27*(4), 1-14. doi: 10.1007/s10856-016-5681-x.

J Mater Sci: Mater Med (2016)27:69
DOI 10.1007/s10856-016-5681-x

BIOMATERIALS SYNTHESIS AND CHARACTERIZATION

Original Research

Production of new 3D scaffolds for bone tissue regeneration by rapid prototyping

R. Fradique[1] · T. R. Correia[1] · S. P. Miguel[1] · K. D. de Sá[1] · D. R. Figueira[1] · A. G. Mendonça[1,2] · I. J. Correia[1]

Received: 5 August 2015 / Accepted: 27 January 2016

Abstract The incidence of bone disorders, whether due to trauma or pathology, has been trending upward with the aging of the worldwide population. The currently available treatments for bone injuries are rather limited, involving mainly bone grafts and implants. A particularly promising approach for bone regeneration uses rapid prototyping (RP) technologies to produce 3D scaffolds with highly controlled structure and orientation, based on computer-aided design models or medical data. Herein, tricalcium phosphate (TCP)/alginate scaffolds were produced using RP and subsequently their physicochemical, mechanical and biological properties were characterized. The results showed that 60/40 of TCP and alginate formulation was able to match the compression and present a similar Young modulus to that of trabecular bone while presenting an adequate biocompatibility. Moreover, the biomineralization ability, roughness and macro and microporosity of scaffolds allowed cell anchoring and proliferation at their surface, as well as cell migration to its interior, processes that are fundamental for osteointegration and bone regeneration.

R. Fradique and T. R. Correia have contributed equally to this work.

Electronic supplementary material The online version of this article (doi:10.1007/s10856-016-5681-x) contains supplementary material, which is available to authorized users.

✉ I. J. Correia
icorreia@fcsaude.ubi.pt; icorreia@ubi.pt

[1] CICS-UBI—Health Sciences Research Centre, University of Beira Interior, Av. Infante D. Henrique, 6200-506 Covilhã, Portugal

[2] Department of Chemistry, University of Beira Interior, R. Marquês d'Ávila e Bolama, 6201-001 Covilhã, Portugal

1 Introduction

Apart from traumatic events, the aging of the worldwide population has led to an increased prevalence of bone tissue diseases, with up to 2.2 million people needing surgery every year [1]. The currently available treatments for bone defects involve the use of bone grafts, particularly autografts, which present serious restrictions such as limited availability, induction of chronic pain and the inability to promote the complete recovery of the patient. To overcome this healthcare problem, a huge effort has been made on the topic of bone tissue engineering in order to create new therapeutic approaches [2]. Artificial bone implants produced from metals, ceramics, polymers and composites have been widely used in bone reconstruction and regeneration [3–10]. Three dimensional (3D) structures, known as scaffolds, constitute one example of these artificial implants and have been produced with materials such as hydroxyapatite (HA), tricalcium phosphate (TCP), poly(lactic-co-glycolic acid) (PLGA) or sodium alginate. Furthermore, scaffolds surfaces can be modified (surface coating, chemical treatment and polymerization) to improve bone healing [11], with some types of scaffolds being used for cell and growth factor delivery to the damaged tissues, while providing mechanical support during the tissue regeneration process [12].

Nowadays, the development of a bone substitute involves the optimization of several parameters, such as biocompatibility, manufacturing simplicity, mechanical requirements, osteoconductivity, osteoinductivity and, depending on the type of implant to be produced (permanent or temporary), its degradation rate, that in some cases must be synchronized with the rate of tissue regeneration [2, 12–17].

Several techniques have been described in literature as being suitable for producing bone replacements. Fiber

Published online: 17 February 2016

bonding [18, 19], freeze drying [20, 21], melting [22, 23], phase inversion [24, 25] and solvent casting [26, 27] are the most employed techniques for scaffolds production. However, some of them present several disadvantages, such as the use of toxic solvents, inability to create large structures with appropriate mechanical properties, absence of pore size control and a limited number of usable materials [28].

The latest advances in the area of computer technology allowed the development of rapid prototyping (RP) techniques that recently started to be used in the design of new 3D constructs aimed to be applied in the area of tissue engineering [29, 30]. So far, computer assisted design (CAD) models supported the manufacturing of highly reproducible 3D scaffolds [31]. To accomplish that, the 3D CAD models are replicated in a layer-by-layer routine, allowing scaffolds to be printed with different conformations and geometries, that may contribute for a significant improvement of scaffold's mechanical properties according to the demands of the damaged bone [32]. As an alternative, other researchers adapted a different strategy based on data collected from routine medical examinations, where the produced scaffolds were specifically tailored, i.e. produced with high anatomic accuracy, to fulfil the particular demands of the injured bone tissue [33–35]. Santos et al. used a 3D printer (Zprinter 310 Plus) to produce scaffolds that replicated the computer tomography data of a human hand [35].

Recently, our group used a Fab@Home plotter to produce TCP/alginate scaffolds with high accuracy, that were previously designed with CAD software [36]. This procedure was adopted taking into account the plotter's cost, versatility and capacity to replicate CAD models with control and reproducibility, in a short period of time [36, 37].

In this study, alginate and TCP were selected to reproduce the organic and inorganic components of the native bone matrix. TCP was used to mimic the mineral phase of the bone, due to its composition, high biocompatibility, bioactivity, great compressive strength osteoconductivity, and also by presenting an in vivo bio-resorption rate that fulfills bone regeneration demands [14, 38, 39]. However, as other ceramics, it possesses a brittle behavior. To overcome this bottleneck, two strategies were selected to improve the mechanical properties of the scaffolds: various ratios of TCP/alginate were used and scaffolds with different geometries were designed using CAD software.

Alginate is a natural polysaccharide derived from brown seaweeds composed of 1,4-linked D-mannuronic acid (M) and α-L-guluronic acid (G) residues [40–42], and is known by its ability to form stable hydrogels when ionically crosslinked with divalent cations (e.g. Ca^{2+},$Sr^{2+}$and Ba^{2+}) [40, 43]. In previous studies it has already been described the successful application of alginate in bone regeneration, either alone or in combination with other polymers and ceramics [36, 43–46].

2 Materials and methods

2.1 Materials

Amphotericin B, bovine serum albumin (BSA), cacodylate buffer (MW = 214.03 g/mol), calcein, calcium chloride, Dulbecco's modified Eagle medium: nutrient mixture F12 (DMEM-F12), ethylenediaminetetraacetic acid (EDTA), gentamicin, glutaraldehyde 25 % (v/v), L-glutamine, sodium alginate (MW = 120–190 kDa), trypan blue and trypsin were purchased from Sigma-Aldrich (Sintra, Portugal). Tricalcium phosphate (TCP) powder (MW = 310.20 g/mol) was obtained from Panreac® (Barcelona, Spain). 3-(4,5-dimethylthiazol-2-yl)-5-(3-carboxymethoxyphenyl)-2-(4-sulfophenyl)-2H tetrazolium reagent, inner salt (MTS) was bought from Promega (Madison, USA). Fetal bovine serum (FBS) was purchased from Biochrom AG (Berlin, Germany). Human osteoblast cells (406-05f) were obtained from Cell Applications, Inc. (San Diego, CA). 24 and 96-well plates were acquired from Orange Scientific (Braine L'Alleud, Belgium). Tris Base was obtained from Fischer Scientific (Lisbon, Portugal). Hoechst 33342® was acquired from Invitrogen (Carlsbad, CA).

2.2 Production of TCP/alginate composite scaffolds by RP

The 3D scaffolds were produced by RP using a Fab@Home plotter, as previously described [36]. TCP/alginate scaffolds were produced using prepared solutions of each compound in a proportion of 60/40 % (w/w), 70/30 % (w/w) and 80/20 % (w/w). Briefly, a 15 % (w/v) alginate solution was prepared by dissolving the polymer in double deionized and filtered water (obtained using a Milli-Q Advantage A10 ultrapure Water Purification System; resistivity = 18.2 MΩ/cm at 25 °C), with overnight agitation. The solution was then homogenized using an X10/25 Ultra-turrax (Ystral, Germany) for 30 min. Finally, TCP powder was added to the alginate solutions to obtain the specific ratios described above, and subsequently the samples were homogenized. Then, a 5 % $CaCl_2$ solution was added to the composite sample (in a 0.14:1 volume ratio of $CaCl_2$ to alginate), and alginate polymer chains got crosslinked leading to an increase of the solution's viscosity that is fundamental for scaffolds production [36]. The used 3D model was designed using CAD/CAM software (OpenSCAD version 2014.3, ©2009–2014 Marius Kintel and Clifford Wolf). The developed 3D model was composed of several layers angled at 45° with the underlying layer (0°–45°–90°–135°), as shown in Fig. 1. Briefly,

the file containing the scaffold model was converted and exported to STL format. Following, a syringe (10 cc Luer Lock) was filled with the composite solution for posterior extrusion. After the extrusion process, the scaffolds were maintained in a 5 % $CaCl_2$ bath for 24 h to achieve a complete crosslinking. Afterwards, the scaffolds were air-dried at RT and subsequently freeze-dried for 24 h.

2.3 Scanning electron microscopy analysis

Scanning electron microscopy (SEM) analysis of the scaffolds was performed in order to characterize the morphology, porosity and surface of the scaffolds. Samples were mounted onto aluminum stubs with Araldite glue and sputter-coated with gold using a Quorum Q150R ES sputter coater (Quorum Technologies, UK). The SEM images were then captured with different magnifications, at an acceleration voltage of 20 kV, using a Hitachi S-3400 N scanning electron microscope (Hitachi, Japan).

2.4 Attenuated total reflectance—fourier transform infrared spectroscopy analysis

To characterize the chemical composition of the scaffolds, Attenuated total reflectance-Fourier transform infrared spectroscopy (ATR-FTIR) was used. The spectra obtained for the samples represent the average of 128 scans, between 400 and 4000 cm^{-1}, with a spectral resolution of 4 cm^{-1}. All the samples were crushed to a powder, mounted on a diamond window, and the spectra were recorded with a Nicolet iS10 FTIR spectrophotometer (Thermo Scientific, Waltham, MA, USA). All the components used for scaffold production were also analyzed in pure state for a comparison to be made with the prepared samples [47].

2.5 Energy dispersive spectroscopic analysis

Energy dispersive spectroscopy (EDS) was used to perform the elemental composition analysis of the various scaffolds. The samples were placed on aluminum stubs, air-dried at RT and examined in an XFlash Detector 5010 (Bruker Nano, Germany).

2.6 Mechanical characterization of the scaffolds

In order to mimic the native environment found in vivo, all specimens of each sample were pre-soaked in culture medium for 4 h. Scaffold's dimensions were determined and then compression assays were performed to characterize the mechanical properties of the scaffolds using a Zwick® 1435 Material Prüfung (Ulm, Germany). A crosshead speed of 3 mm/min and a load cell of 5kN were used for analyzing five specimens of the different formulations in each assay.

The compressive strength (C_s) of each scaffold was calculated according to Eq. (1) [48].

$$C_s = \frac{F}{w * l} \tag{1}$$

where F is the load at the time of fracture, and w and l represent the width and length of the scaffold, respectively.

The Young modulus (YM) of each scaffold was calculated from the stress–strain relation, calculated by applying Eq. (2).

$$YM = \frac{C_s}{H_d} \tag{2}$$

where H_d stands for the height deformation at maximum load and C_s is the scaffold compressive strength. Average

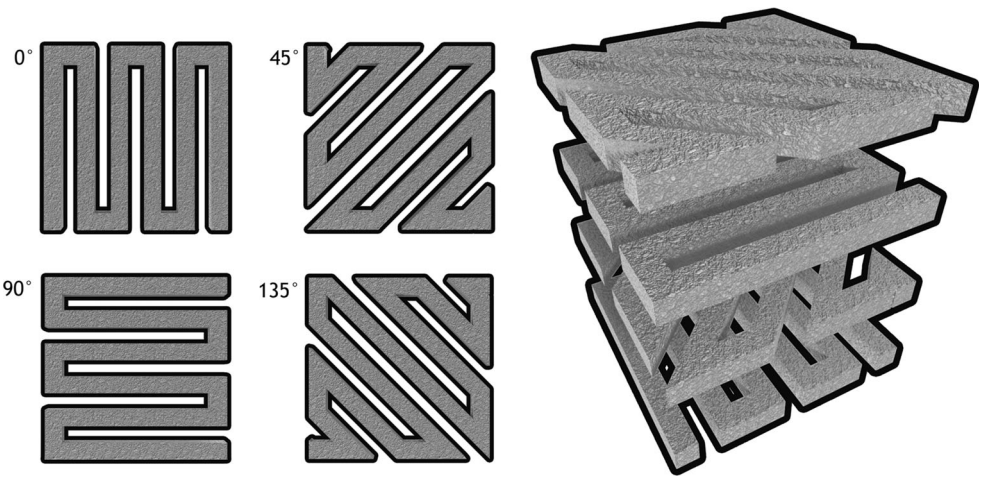

Fig. 1 Schematic overview of the layered structure of the model

values and standard deviations (S.D.) were determined for each sample.

2.7 Swelling studies

The swelling capacity of the scaffolds was determined through a method adapted from literature [43]. In brief, samples were immersed in Tris buffer (1 M, Ph 7.4), at 37 °C, for 2 days (n = 3). After absorbing the excess of Tris with filter paper, scaffolds were removed from the solution at predetermined intervals and weighed. Following this process, the samples were re-immersed in the swelling solution. The swelling ratio of the scaffolds was evaluated using Eq. (3).

$$Swelling\ ratio\ (\%) = \frac{W_t - W_0}{W_0} * 100 \quad (3)$$

where W_t is the final weight of the scaffolds and W_0 their initial weight.

2.8 Contact angle measurements

Contact angle measurements were performed using a OCAH 200 Contact Angle System (DataPhysics Instruments, Germany), operated in static mode at RT. This assay was performed using water as reference fluid [36]. For each sample, water drops were placed at various locations of the surface of the scaffold. The reported contact angles are the average of at least three measurements.

2.9 Evaluation of the porosity of the scaffolds

To determine the microporosity of the different scaffolds a liquid displacement method was used, according to the procedure previously reported [48]. In brief, scaffolds were weighed, immersed in absolute ethanol (EtOH) for 48 h, and weighed again. EtOH was chosen for its ability to penetrate throughout the scaffolds without causing shrinking or swelling of the matrix [49]. The porosity was then calculated by determining the amount of EtOH absorbed, through Eq. (4):

$$Porosity(\%) = \frac{W_w - W_d}{D_{ethanol} * V_{Scaffold}} * 100 \quad (4)$$

where W_w and W_d are the wet and dry weights of the scaffolds, respectively, $D_{ethanol}$ represents the density of EtOH at RT and $V_{scaffold}$ the volume of the wet scaffold. Five replicates of each scaffold were used, and the data represents the average values obtained.

2.10 Characterization of the degradation profile of the scaffolds

The degradation profile of the composite scaffolds was investigated through a method previously published. [50, 51] In brief, scaffolds were placed in 24-well plates, fully immersed in DMEM-F12 at 37 °C. At predetermined intervals, samples were removed, completely dried and weighted. The degradation percentage at each point was calculated through Eq. (5):

$$Weight\ loss\ (\%) = (\frac{W_i - W_t}{W_i}) * 100 \quad (5)$$

where *Wi* corresponds to the initial weight of the sample and *Wt* to the weight of the sample at time t.

2.11 In vitro biomineralization assay

The in vitro bioactivity of each scaffold was evaluated by submerging them in standard simulated body fluid (SBF), followed by incubation at 37 °C for 7, 14, and 21 days, according to a method previously described in literature [52]. The SBF solution had a similar ionic concentration to that found in human blood plasma (142.0 mM Na^+, 5 mM K^+, 1.5 mM Mg^{2+}, 2.5 mM Ca^{2+}, 147.8 mM Cl^-, 4.2 mM HCO_3^-, 1.0 mM HPO_4^{2-}, and 0.5 mM SO_4^{2-}), and a pH of 7.4 at 37 °C [53]. Three scaffolds of equal weight and shape were used. After each period of incubation, the scaffolds were removed and rinsed three times with deionised water to remove soluble inorganic ions. The deposition of calcium and phosphate ions on the composite surface was characterized by EDS.

2.12 Characterization of the biological properties of the scaffolds

2.12.1 Evaluation of cell viability and proliferation in the presence of the scaffolds

Human osteoblasts cells (hOB) were cultured in DMEM-F12, supplemented with 10 % heat inactivated FBS, amphotericin B (100 µg/mL) and gentamicin (100 µg/mL) in 75 cm^2 T-flasks. Cells were maintained in a humidified environment at 37 °C, with 5 % CO_2, until confluence was attained. Subsequently, cells were trypsinized with 0.18 % trypsin (1:250) and 5 mM EDTA, and centrifuged for 5 min. Prior to cell seeding, scaffolds were cut into pieces with appropriate sizes and placed into 96-well plates to be sterilized by UV irradiation for 30 min. Following, cells were seeded at a density of 10×10^3 cells per well, in order to evaluate cell viability and proliferation. The culture medium was replaced every 2 days until the end of the assay.

To evaluate the cytotoxic character of the 3D scaffolds, an MTS assay was performed at day 4 and 7 [36]. The metabolic activity of the cells was assessed by quantifying the metabolic conversion of MTS to formazan. Briefly, the medium in each well was replaced with a mixture of

100 µL of fresh culture medium and 20 µL of MTS/phenazine methosulfate (PMS) reagent solution, and then the plate was incubated for 4 h at 37 °C. Following the incubation period, the supernatant was transferred into a 96-well microplate and the fluorescence intensity measured at 492 nm, using a microplate reader (Anthos 2020, Biochrom, UK). Five replicates of each sample were used for each experimental condition. Cells cultured without materials were used as negative control (K^-) and cells cultured with EtOH (70 %) were used as positive control (K^+).

2.12.2 Scanning electron microscopy analysis

In order to evaluate the cellular behavior in the presence of the scaffolds, SEM analysis was performed according to the method previously described by Lee and Chow [54]. Briefly, the samples were washed at RT with sodium cacodylate buffer solution (0.1 M, pH 7.4), and then fixed for 30 min in a 2.5 % (v/v) glutaraldehyde in 0.1 M sodium cacodylate solution. Subsequently, samples were frozen in liquid nitrogen for 2 min and then freeze-dried for 2 h. SEM analysis was performed as described in Sect. 2.3.

2.12.3 Confocal laser scanning microscopy analysis

Confocal laser scanning microscopy (CLSM) was used to characterize the cell distribution within the 60/40 scaffold. This formulation was selected based on the results obtained herein. hOB nucleus were labelled with Hoescht 33342 (5 µg/mL) and seeded in the presence of the scaffolds (10×10^3 cells/scaffold), in µ-Slide 8-well Ibidi imaging plates (Ibidi GmbH, Germany). After 24 h, the scaffold was labelled with calcein (20 µg/mL) and confocal images were acquired. Imaging experiments were performed in a Zeiss LSM 710 laser scanning confocal microscope (Carl Zeiss AG, Germany), where consecutive z-stacks were acquired. The 3D reconstruction and image analysis were performed using Zeiss Zen 2010 software [36].

2.13 Statistical analysis

One-way analysis of variance (ANOVA), with the Newman–Keuls post hoc test was used for comparison of the different test groups. A p value lower than 0.05 ($p < 0.05$) was considered statistically significant. Data analysis was performed in GraphPad Prism v.6.0 software (Trial version, GraphPadSoftware, CA, USA).

3 Results and discussion

3.1 Morphological characterization of the produced scaffolds

Different approaches have been used in the area of regenerative medicine to answer the limitations of the currently available therapeutics. Among them, RP technologies have proven to be a precious tool in every stage of development, greatly improving the design decision process and the scaffold's mechanical properties.

In this work, composite scaffolds constituted by TCP and alginate were produced by RP, for mimicking the natural bone matrix properties (20–30 % organic, 70–80 % inorganic) [14, 17]. To do so, an optimization of the scaffold's production parameters was done. Figure 2 presents the CAD model used, as well as one of the scaffolds printed by RP. The designed model is a 13 mm × 13 mm × 13 mm cube, with a porous structure. As described, it is composed by layers rotated 45° in relation to the underlying layer (0°–45°–90°–135°), in order to increase its mechanical resistance.

Alginate was selected for scaffolds production due to its capacity to act as temporary extracellular matrix (ECM) for bone cells. In addition, the possibility of controlling the degradation rate of this polymer is of great importance for tailoring the properties of the scaffold [40, 41]. On the other hand, TCP was chosen due to its resemblance with the natural ceramic component of bone tissue, increased biocompatibility, low cost, osteoconductivity and enhanced mechanical resistance [2, 38, 55]. Furthermore, the combination of these materials has already been shown to improve cell adhesion and proliferation, with the potential to allow cell growth and differentiation before implantation [36, 56]. Macroscopic images of the produced scaffolds are presented in Fig. 3.

Through the analysis of the images shown in Fig. 3 it is possible to observe that the TCP content had a direct effect on the scaffold's structure, namely on the scaffold's dimensions, decreasing the shrinking endured. It was previously described that alginate gels and scaffolds suffer shrinkage during the drying process [57]. Other researchers have also reported that the presence of solid fillers, such as ceramic particles, in an alginate solution has a direct effect on the volume loss during the drying process [58]. It was noticed that the compression of the polymeric matrix leads to the compression of the TCP particles against each other. Herein, it was verified that the scaffolds containing the highest percentage of TCP suffered less shrinkage, since the amount of incompressible ceramic particles limits the shrinking that

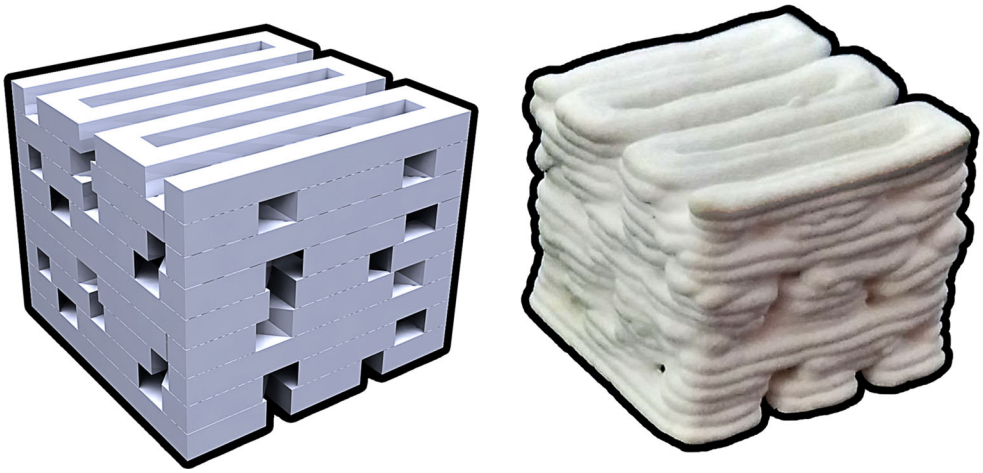

Fig. 2 Images of the CAD model used (*left*) and of the final printed model (*right*)

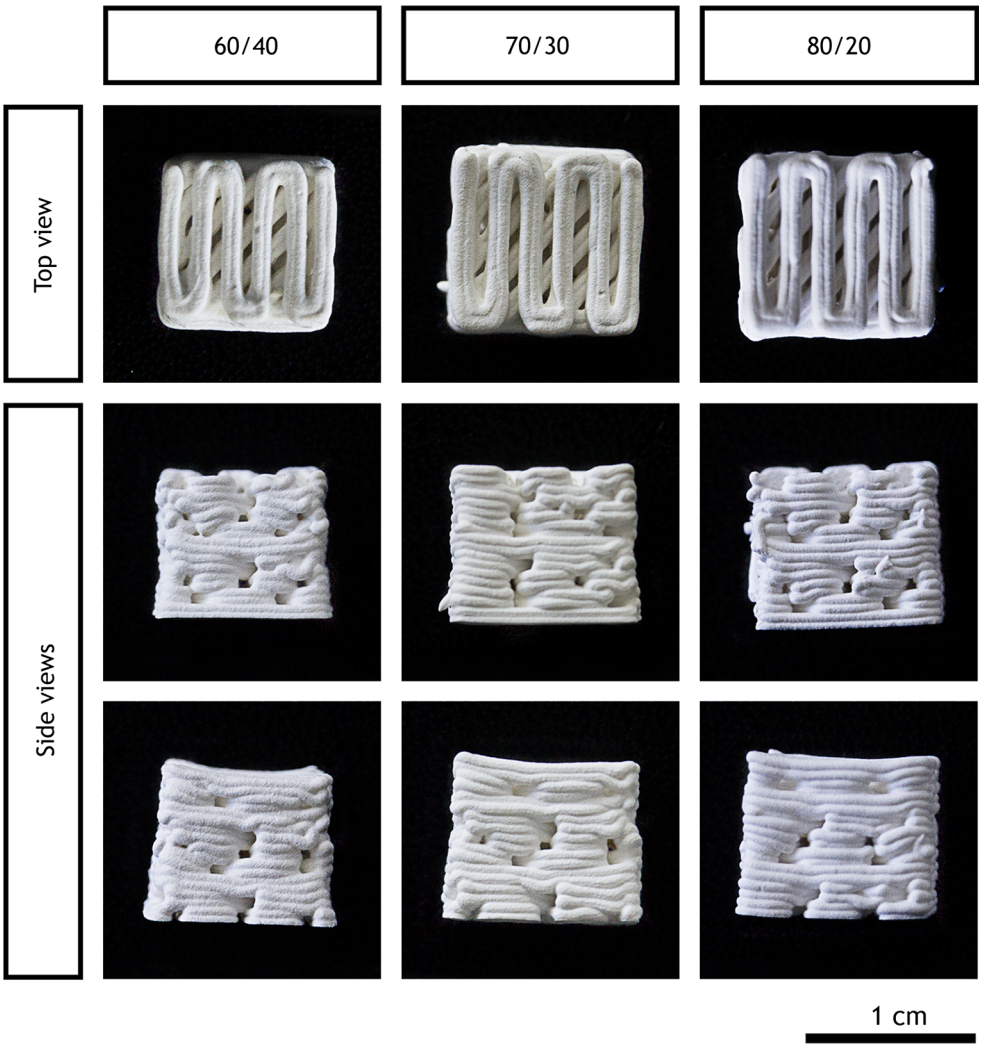

Fig. 3 Representative macroscopic images of the different produced scaffolds

scaffolds can suffer. This is important, since an excess shrinking can greatly affect the scaffold's porosity and its mechanical properties.

Furthermore, the scaffolds surface morphology has a great effect on cell adhesion and, consequently, on the successful material implantation. Figure 4 shows SEM

images acquired to characterize the surface morphology of the produced scaffolds.

Through the analysis of Fig. 4 it is possible to verify that all the scaffolds presented similar surface characteristics, with high roughness and irregularities. It has been previously described that the surface roughness of a scaffold has a great effect on protein adsorption and cell adhesion, upon scaffold implantation [59, 60]. On irregular surfaces, human osteoblasts present increased metabolism and ECM production, due to an increased contact surface available for promoting adhesion contact points [6].

3.2 Characterization of the physicochemical properties of the scaffolds

3.2.1 ATR-FTIR analysis

An ATR-FTIR analysis was performed to evaluate the chemical composition of the scaffolds. The ATR-FTIR spectra of the raw materials and of the produced scaffolds are presented in Fig. 5.

The ATR-FTIR spectrum of TCP presents a peak at 1020 cm^{-1} (I), that is characteristic of a P=O stretch vibration, thus revealing the presence of the inorganic phosphate components of TCP [35]. This peak is also present on the spectra of the produced scaffolds, with an intensity that is proportional to the ceramic content present in each sample. The ATR-FTIR spectrum of sodium alginate powder presented two peaks at 1400 and 1600 cm^{-1} (II), corresponding to the C=O stretching of the carboxylate group [61]. In addition, a stretching vibration correspondent to the O–H bonds of alginate appeared in the range 3000–3600 cm^{-1} (III) [62]. These peaks were also present in the spectra of the different scaffolds, without perceptible variations among them.

3.2.2 Energy dispersive spectroscopy analysis

The elemental composition of the scaffolds was also characterized through EDS analysis, to elucidate the chemical composition of the scaffolds. Table 1 shows that samples with a higher amount of ceramic component have a greater percentage of phosphate and calcium. Such results are in agreement with the expectations, since these are the

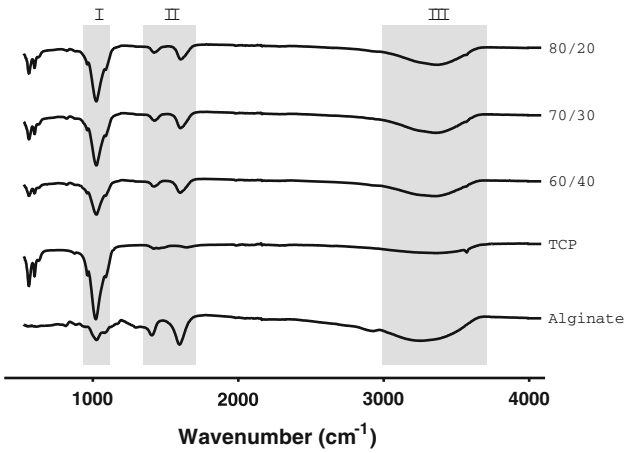

Fig. 5 ATR-FTIR analysis of the alginate, TCP and TCP/alginate scaffolds (80/20, 70/30, and 60/40)

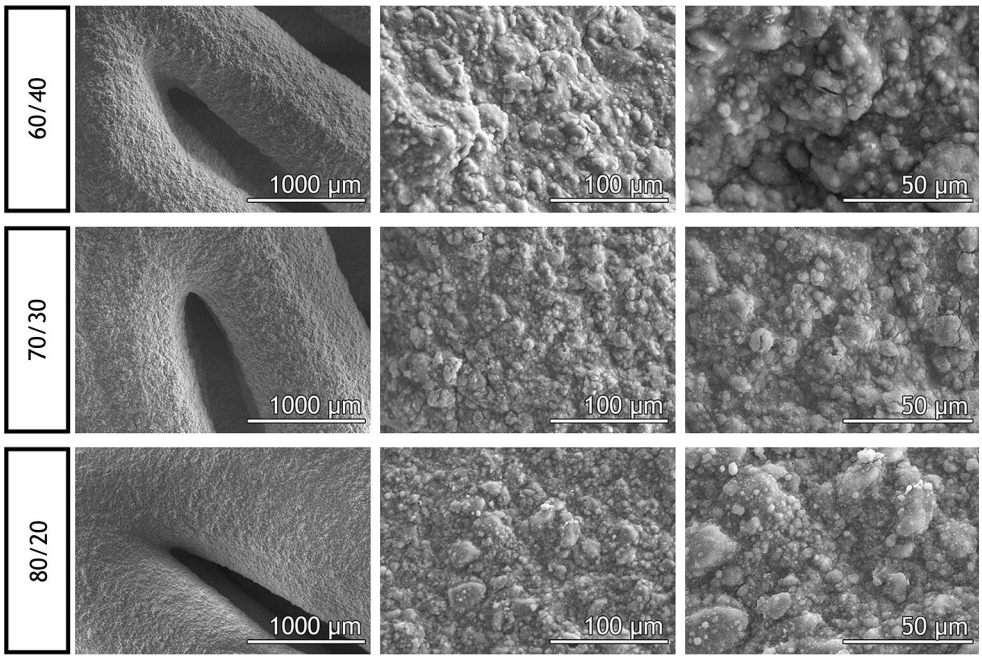

Fig. 4 SEM images showing the morphology of the different produced scaffolds at different magnifications

Table 1 EDS analysis of the produced TCP/alginate scaffolds (60/40, 70/30 and 80/20) and the Ca/P ratios determined for the produced scaffolds

	P	Ca	Ca/P ratio
60/40	2.89	8.48	2.93
70/30	4.35	9.42	2.17
80/20	4.71	10.28	2.18

main components of TCP. In addition, the Ca/P ratios of the produced scaffolds are within the range described for native trabecular bone (2.33 ± 0.34) [63].

3.2.3 *Characterization of the mechanical properties of the scaffolds*

A scaffold to be used in bone tissue regeneration must present adequate resistance and flexibility. The mechanical behavior of the produced scaffolds was analyzed by determining the resistance to compression and the Young's modulus (Fig. 6).

Previous studies described that 3D constructs with an increased ceramic content have an increased brittleness and, consequently, a lower mechanical resistance [64, 65]. The high TCP content of the 70/30 and 80/20 scaffolds produced here led to an increased brittleness and fragility, characteristic of pure ceramic scaffolds [65]. Furthermore, in a biphasic solution, the polymeric component (alginate in this case) creates a bone like structure by trapping the ceramic particles [66].

In this study, to simulate the mechanical performance of the scaffolds under in vivo conditions, their mechanical properties were evaluated in wet conditions. Figure 6 shows the results obtained for the different samples in the compression strength and modulus young assays. The 60/40 sample showed a compressive strength of 20 MPa, the 70/30 a value of ~10 MPa and the 80/20 a value of 2 MPa. Such results are agreement with previous studies [65], where an increase in ceramic content leads to a lower compressive strength. Although, all the produced specimens presented a compressive strength similar to that displayed by trabecular bone (0.5–15 MPa). Based on the collected data it can be inferred that these type of scaffolds have the required mechanical properties to be applied in non-load bearing sites.

Moreover, a large mismatch of the elastic modulus of the implant and that of the native bone tissue can be responsible for stress shielding, and consequently, result in a limited scaffold osteointegration [67]. In this context, the Young modulus of the three specimens was also investigated in wet conditions, showing that the scaffolds with the lowest ceramic content (60/40) presented the highest modulus (70 MPa), while the 70/30 and 80/20 formulations presented 40 and 9 MPa, respectively. In comparison with the Young modulus characteristic of cancellous bone(100–200 MPa [15]), the 60/40 scaffolds had the closest value.

Therefore, taking into account these results the 60/40 scaffolds are the most promising candidates to be applied in bone regeneration, since they closely reproduce the native bone matrix structure, while they are able to present mechanical properties similar to those of trabecular bone tissue.

3.2.4 *Swelling studies*

The swelling capacity of a scaffold can have a deep impact on its biocompatibility and biologic performance. In fact, scaffolds with an increased capacity to absorb water promote protein adsorption and cell adhesion, leading to a reduced immune response from the host [68]. The swelling profiles obtained for the produced scaffolds are presented in Fig. 7a. All scaffolds presented a rapid swelling in the first minutes and then stabilized after about 10 h of immersion in Tris buffer (1 M, pH 7.4).

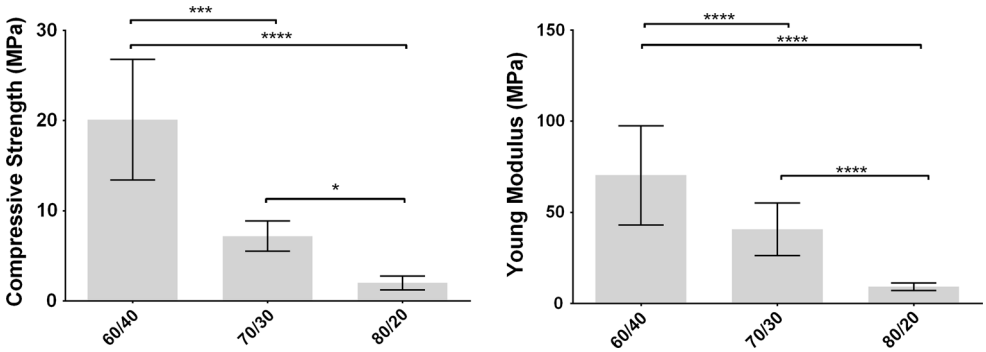

Fig. 6 Characterization of the compressive strength (*left*) and young modulus (*right*) of the scaffolds. Statistical analysis of the results was performed using one-way ANOVA with Newman–Keuls post hoc test (****$p \leq 0.0001$)

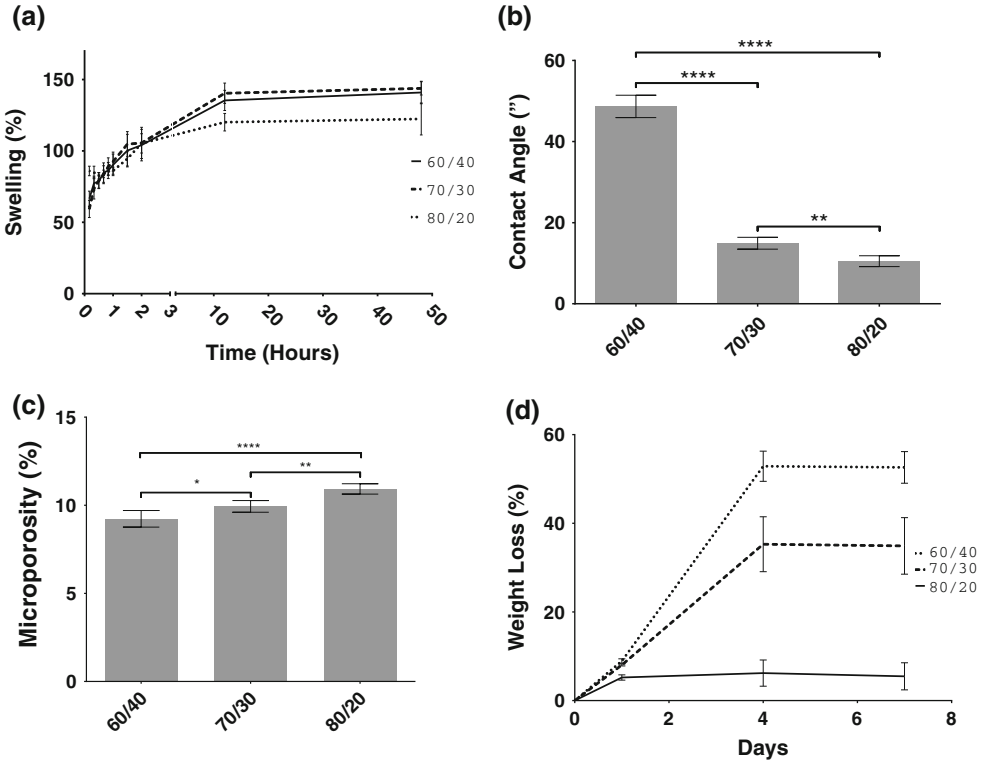

Fig. 7 Characterization of the swelling profile of the scaffolds (**a**); contact angle of the different produced scaffolds (**b**); statistical analysis of the results was performed using one-way ANOVA with a Newman–Keuls test (**$p \leq 0.01$, ****$p \leq 0.0001$); scaffold's microporosity (**c**); Statistical analysis of the data was performed using one-way ANOVA with a Newman–Keuls test (*$p \leq 0.05$, **$p \leq 0.01$, ****$p \leq 0.0001$, n = 5); and degradation profile of the scaffolds (**d**)

Valente et al. have already reported that a polymeric network composed of alginate is capable of absorbing large quantities of water by filling its void regions [43]. This effect was also confirmed in this study, where the scaffolds containing higher amounts of alginate presented a higher swelling ratio.

3.2.5 *Contact angle analysis*

In order to evaluate the hydrophilic character of the scaffolds, the contact angles were determined, as can be observed in Fig. 7b. It is possible to perceive that all the scaffolds presented a hydrophilic character, with contact angles below 70°. The 60/40 scaffolds showed a moderated hydrophilic character ($\approx$50°) while the 70/30 and 80/20 presented an almost superhydrophilic character ($\approx$20°). Hu et al. previously reported a direct correlation between the increase in the TCP content of the scaffolds and its hydrophilic character [69]. Scaffolds with moderate wettability improve cell attachment and growth, since their surfaces have preferential adsorption of cell-adhesive proteins [69, 70].

3.2.6 *Scaffolds porosity evaluation*

The microporosity of the scaffolds was determined by a liquid displacement method, using ethanol as displacement fluid. Figure 7c shows that the scaffolds with highest TCP content presented the highest porosity values (>10 % porosity). During the drying process the scaffolds suffer shrinking, which is responsible for the compression of the polymeric matrix. In this stage, the scaffolds with high ceramic content present more incompressible particles, thus limiting the amount of shrinkage that they can suffer, and consequently displaying an increased porosity [35, 36].

These results corroborate the mechanical resistance data obtained. Porosity and density are inversely proportional, and are closely related to the mechanical resistance of a scaffold [71]. Therefore, the most resistant scaffolds are the denser, as can be observed in Fig. 7c.

The porosity values obtained for the produced scaffolds are more similar to that of compact bone (3 %), than those displayed by trabecular bone (80 %) [72]. However, this lack of microporosity is balanced by a regular and sufficient macroporosity, as can be observed in Fig. 4. This macroporosity allows tissue ingrowth and osteointegration, and also facilitates the exchange of nutrients and metabolites from the interior of the scaffolds.

3.2.7 *Characterization of the degradation profile of the scaffolds*

The degradation rate of the scaffolds should be compatible with the time needed to occur new bone formation, in order for the scaffold be replaced during the regeneration process without affecting the mechanical stability of the tissue, at

the injured site [73]. The degradation profile of the produced scaffolds is presented in Fig. 7d. The results obtained showed that the scaffolds present a degradation profile dependent on its relative alginate content, with those containing a higher percentage of the polymer enduring a greater loss of mass. Under in vivo conditions, alginate depolymerizes by spontaneous alkaline elimination of its glycosidic linkages. Moreover, this polymer can also suffer disintegration by gradual exchange of calcium ions with sodium, reversing the gelling process [40]. On the other hand, TCP can suffer cell-mediated degradation when implanted in vivo, being solubilized while new tissue formation occurs [74].

Nonetheless, none of the scaffolds produced here lost more than 60 % of its mass, and all of them stabilized after 4 days, which is compatible with their application in bone tissue regeneration.

3.3 In vitro biomineralization assay

The in vitro mineralization ability of the composite scaffolds was studied using an SBF assay (Fig. 8). The obtained results revealed that calcium and phosphate content of the scaffolds increased along time. In addition, this increase was more pronounced for the formulations with higher TCP content. As previously described, TCP is a bioactive ceramic capable of inducing mineralization at the surface of the scaffolds, increasing their biointegration [52, 75], and consequently the bone regeneration process [75].

3.4 Characterization of the biological properties of the scaffolds

In vitro studies were performed to study the cytotoxic profile of the scaffolds. Human osteoblast cells were cultured in contact with the scaffolds for up to 7 days, and their viability assessed at days 4 and 7. The optical images acquired at the mentioned time points demonstrated that cells were able to proliferate in the presence of the composite scaffolds (please see Figure S1 for further details) and in the negative control. In the positive control, dead cells with their characteristic spherical shape were observed. To further characterize the cellular adhesion on the surface of the scaffolds, SEM images were also acquired (Fig. 9a).

As previously demonstrated, scaffolds showed a surface with high roughness, irregularities and a hydrophilic character that allowed cell adhesion. In fact, it is possible to observe that the cells were able to adhere to the surface of the material after 24 h of being seeded. Moreover, after 7 days, most cells had spread throughout the entire surface of the scaffold, and a cell layer was observed, demonstrating that all the scaffolds presented a suitable surface for cell adhesion and proliferation.

The biocompatibility of the scaffolds was further evaluated through an MTS assay (Fig. 9b). The results obtained in the MTS assay show that the cells remained viable after 4 and 7 days in the presence of all the produced scaffolds, indicating that all scaffolds provide an appropriate environment for cell adhesion and proliferation. The 60/40 formulation presented the highest cellular viability, which may be explained by their increased alginate content [43, 45]. Moreover, this formulation is the one that better reproduce the bone native constitution, further enhancing cell proliferation. These results can also be attributed to the osteogenic potential of TCP, which creates a layer that is similar to apatite on the surface of the material, due to its interaction with the surrounding medium [76].

CLSM analysis was performed 24 h after osteoblasts being seeded in contact with the 60/40 scaffold (Fig. 9c). This formulation was selected based on the previously achieved results. A 3D reconstruction image is presented in Fig. 9c_1, c_2, showing that the osteoblasts were able to adhere and proliferate in the tested formulation. Such highlights its biocompatibility and appropriate physicochemical properties. Moreover, the analysis of the orthogonal slices (Fig. 9c_3) and colour coded depth analysis (Fig. 9c_4) of 60/40 scaffold showed that osteoblasts migrate to the interior of the scaffold, with some cells being observed between 5 and 20 μm within the structure

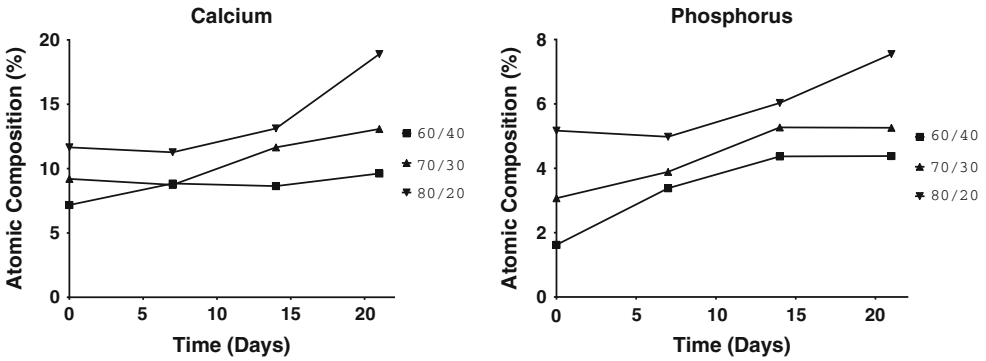

Fig. 8 EDS analysis of the different scaffolds after 7, 14 and 21 days in SBF

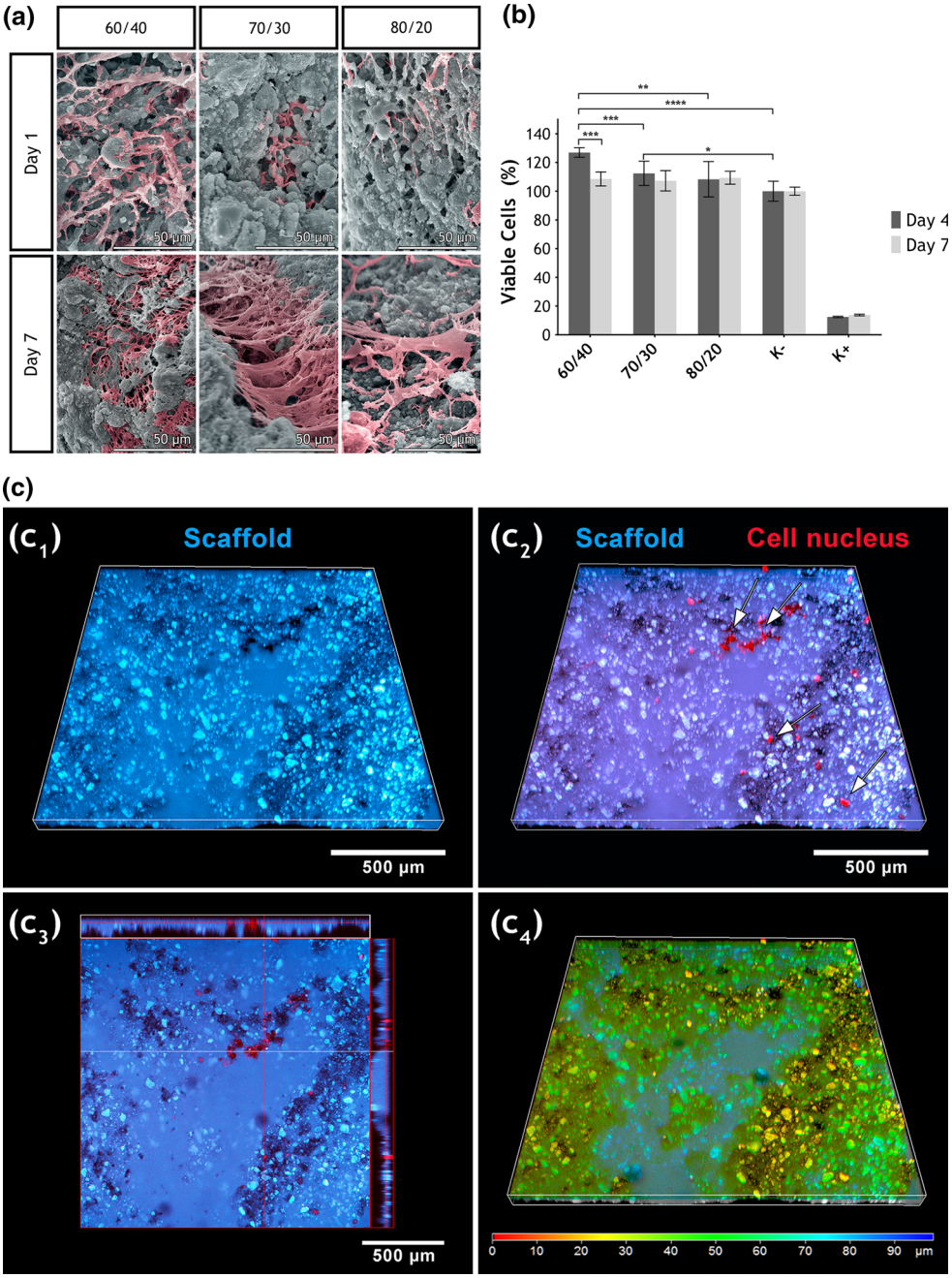

Fig. 9 Characterization of the biological properties of the scaffolds. **a** SEM images of hOB in the presence of the scaffolds; **b** evaluation of hOB viability when cultured in contact with the different scaffolds after 4 and 7 days; live cells (K−); dead cells (K+). Each result is the mean ± standard deviation of the mean of at least three independent experiments. Statistical analysis was performed using one-way ANOVA with Newman–Keuls post hoc test (*$p < 0.05$, **$p \leq 0.01$, ***$p \leq 0.001$, ****$p \leq 0.0001$); **c** 3D reconstruction images (*c1* and *c2*), orthogonal projections (*c3*), and colour coded depth analysis (*c4*) of cells in contact with the 60/40 TCP/alginate scaffold (*red* 0 µm, *blue* 90 µm). *Arrows* show the presence of cells (Color figure online)

of the scaffold. This cellular colonization of the structure will eventually allow the filling of the bone defect with new bone matrix, while the scaffold is biodegraded, thus leading to the restoring of the structure and functions of the native tissue.

4 Conclusion

The huge demand of new therapeutic approaches for bone regeneration triggered the development of different studies. Herein, scaffolds with different ratios of TCP and alginate were successfully produced using a Fab@Home. Besides optimizing the ratios of TCP/alginate for scaffolds manufacture, authors also used CAD software to further improve the mechanical characteristics of the 3D constructs. The compression and young modulus of the different produced scaffolds were characterized and those with 60/40 of TCP and alginate were selected as the best formulation. The results obtained revealed that the properties of these scaffolds matched the standard values for compression and have a similar Young modulus of the trabecular bone. In addition, the hydrophilic character of the produced scaffolds was also investigated. The 60/40 formulation showed

a moderately hydrophilic character ($\approx 50°$) while the others presented a superhydrophilic character ($\approx 20°$). The moderately hydrophilic behaviour displayed by the 60/40 structures allows protein adhesion at the surface of the materials, which is essential for cell adhesion and proliferation. Moreover, the biomineralization ability, roughness and macro and microporosity of scaffolds also contributed for cell anchoring and proliferation at their surface, as well as cell migration to its interior. These processes are fundamental for osteointegration and bone regeneration. Furthermore, the application of RP technologies for the production of the scaffolds can provide a great contribution to personalized therapy, since CAD tools can be used to design 3D structures that fulfil patient requirements and contribute to decrease the healing time. Encapsulation of cells and bioactive molecules in the produced scaffolds can also be hypothesized in a future of work, since no hazard agent is used during the scaffolds manufacture.

Acknowledgments Authors would like to acknowledge funding from FEDER (POCI-COMPETE 2020, project number 007491), Portuguese Science Foundation (FCT) (UID/Multi/00709) and QREN (Programa Mais Centro) (CENTRO-07-0224-FEDER-002014).

References

1. Giannoudis PV, Dinopoulos H, Tsiridis E. Bone substitutes: an update. Injury. 2005;36(Suppl 3):S20–7. doi:10.1016/j.injury.2005.07.029.
2. O'Brien FJ. Biomaterials & scaffolds for tissue engineering. Mater Today. 2011;14(3):88–95. doi:10.1016/S1369-7021(11)70058-X.
3. Bobe K, Willbold E, Morgenthal I, Andersen O, Studnitzky T, Nellesen J, et al. In vitro and in vivo evaluation of biodegradable, open-porous scaffolds made of sintered magnesium W4 short fibres. Acta Biomater. 2013;9(10):8611–23.
4. Rai R, Keshavarz T, Roether JA, Boccaccini AR, Roy I. Medium chain length polyhydroxyalkanoates, promising new biomedical materials for the future. Mater Sci Eng, R. 2011;72(3):29–47.
5. He J, Huang T, Gan L, Zhou Z, Jiang B, Wu Y, et al. Collagen-infiltrated porous hydroxyapatite coating and its osteogenic properties: in vitro and in vivo study. J Biomed Mater Res Part A. 2012;100(A(7)):1706–15.
6. Chiara G, Letizia F, Lorenzo F, Edoardo S, Diego S, Stefano S, et al. Nanostructured biomaterials for tissue engineered bone tissue reconstruction. Int J Mol Sci. 2012;13(1):737–57.
7. Xie M, Olderøy MO, Zhang Z, Andreassen JP, Strand BL, Sikorski P. Biocomposites prepared by alkaline phosphatase mediated mineralization of alginate microbeads. RSC Adv. 2012;2(4):1457–65.
8. Wu S, Liu X, Yeung KWK, Hu T, Xu Z, Chung JCY, et al. Hydrogen release from titanium hydride in foaming of orthopedic NiTi scaffolds. Acta Biomater. 2011;7(3):1387–97.
9. Alvarez K, Nakajima H. Metallic Scaffolds for Bone Regeneration. Materials. 2009;2(3):790–832.
10. Li Z, Gu X, Lou S, Zheng Y. The development of binary Mg-Ca alloys for use as biodegradable materials within bone. Biomaterials. 2008;29(10):1329–44.
11. Wu S, Liu X, Yeung KW, Liu C, Yang X. Biomimetic porous scaffolds for bone tissue engineering. Mater Sci Eng. 2014;80:1–36.
12. Malda J, Visser J, Melchels FP, Jüngst T, Hennink WE, Dhert WJA, et al. 25th anniversary article: engineering hydrogels for biofabrication. Adv Mater. 2013;25(36):5011–28. doi:10.1002/adma.201302042.
13. Frohlich M, Grayson W, Wan L, Marolt D, Drobnic M, Vunjak-Novakovic G. Tissue engineered bone grafts: biological requirements, tissue culture and clinical relevance. Curr Stem Cell Res Ther. 2008;3(4):254–64. doi:10.2174/157488808786733962.
14. Gaalen SV, Kruyt M, Meijer G, Mistry A, Mikos A, Beucken JVD, et al. Tissue engineering of bone. In: Blitterswijk CV, Thomsen P, Lindahl A, Hubbell J, Williams DF, Cancedda R, et al., editors. Tissue engineering. Burlington: Academic Press; 2008. p. 559–610.
15. Bose S, Roy M, Bandyopadhyay A. Recent advances in bone tissue engineering scaffolds. Trends Biotechnol. 2012;30(10):546–54.
16. Ma PX. Biomimetic materials for tissue engineering. Adv Drug Deliv Rev. 2008;60(2):184–98. doi:10.1016/j.addr.2007.08.041.
17. Kneser U, Schaefer DJ, Polykandriotis E, Horch RE. Tissue engineering of bone: the reconstructive surgeon's point of view. J Cell Mol Med. 2006;10(1):7–19. doi:10.1111/j.1582-4934.2006.tb00287.x.
18. Mikos AG, Bao Y, Cima LG, Ingber DE, Vacanti JP, Langer R. Preparation of poly(glycolic acid) bonded fiber structures for cell attachment and transplantation. J Biomed Mater Res. 1993;27(2):183–9. doi:10.1002/jbm.820270207.
19. Tuzlakoglu K, Bolgen N, Salgado AJ, Gomes ME, Piskin E, Reis RL. Nano- and micro-fiber combined scaffolds: a new architecture for bone tissue engineering. J Mater Sci. 2005;16(12):1099–104. doi:10.1007/s10856-005-4713-8.
20. Deville S, Saiz E, Tomsia AP. Freeze casting of hydroxyapatite scaffolds for bone tissue engineering. Biomaterials. 2006;27(32):5480–9. doi:10.1016/j.biomaterials.2006.06.028.
21. Kim H-W, Knowles JC, Kim H-E. Hydroxyapatite and gelatin composite foams processed via novel freeze-drying and crosslinking for use as temporary hard tissue scaffolds. J Biomed Mater Res, Part A. 2005;72A(2):136–45. doi:10.1002/jbm.a.30168.
22. Gomes ME, Ribeiro AS, Malafaya PB, Reis RL, Cunha AM. A new approach based on injection moulding to produce biodegradable starch-based polymeric scaffolds: morphology, mechanical and degradation behaviour. Biomaterials. 2001;22(9):883–9. doi:10.1016/S0142-9612(00)00211-8.
23. Mondrinos MJ, Dembzynski R, Lu L, Byrapogu VKC, Wootton DM, Lelkes PI, et al. Porogen-based solid freeform fabrication of polycaprolactone–calcium phosphate scaffolds for tissue engineering. Biomaterials. 2006;27(25):4399–408. doi:10.1016/j.biomaterials.2006.03.049.
24. Duarte ARC, Mano JF, Reis RL. Dexamethasone-loaded scaffolds prepared by supercritical-assisted phase inversion. Acta Biomater. 2009;5(6):2054–62. doi:10.1016/j.actbio.2009.01.047.
25. Tsivintzelis I, Pavlidou E, Panayiotou C. Porous scaffolds prepared by phase inversion using supercritical CO2 as antisolvent: i. Poly(l-lactic acid). J Supercrit Fluids. 2007;40(2):317–22. doi:10.1016/j.supflu.2006.06.001.
26. Suh SW, Shin JY, Kim J, Kim J, Beak CH, Kim DI, et al. Effect of different particles on cell proliferation in polymer scaffolds using a solvent-casting and particulate leaching technique. ASAIO J. 2002;48(5):460–4.
27. Sin D, Miao X, Liu G, Wei F, Chadwick G, Yan C, et al. Polyurethane (PU) scaffolds prepared by solvent casting/particulate leaching (SCPL) combined with centrifugation. Mater Sci Eng C. 2010;30(1):78–85. doi:10.1016/j.msec.2009.09.002.
28. Salgado AJ, Coutinho OP, Reis RL. Bone tissue engineering: state of the art and future trends. Macromol Biosci. 2004;4(8):743–65. doi:10.1002/mabi.200400026.

29. Daniel LC, Jeffrey IL, Lawrence JB, Hod L. Additive manufacturing for in situ repair of osteochondral defects. Biofabrication. 2010;2(3):035004.
30. Malone E, Lipson H. Fab@Home: the personal desktop fabricator kit. Rapid Prototyp J. 2007;13(4):245–55. doi:10.1108/13552540710776197.
31. Fedorovich NE, Schuurman W, Wijnberg HM, Prins H-J, van Weeren PR, Malda J, et al. Biofabrication of osteochondral tissue equivalents by printing topologically defined, cell-laden hydrogel scaffolds. Tissue Eng Part C. 2011;18(1):33–44. doi:10.1089/ten.tec.2011.0060.
32. Shaffer S, Yang K, Vargas J, Di Prima MA, Voit W. On reducing anisotropy in 3D printed polymers via ionizing radiation. Polymer. 2014;55(23):5969–79.
33. Martínez-Vázquez FJ, Perera FH, Miranda P, Pajares A, Guiberteau F. Improving the compressive strength of bioceramic robocast scaffolds by polymer infiltration. Acta Biomater. 2010;6(11):4361–8. doi:10.1016/j.actbio.2010.05.024.
34. Hockaday LA, Kang KH, Colangelo NW, Cheung PYC, Duan B, Malone E, et al. Rapid 3D printing of anatomically accurate and mechanically heterogeneous aortic valve hydrogel scaffolds. Biofabrication. 2012;4(3):035005.
35. Santos CFL, Silva AP, Lopes L, Pires I, Correia IJ. Design and production of sintered β-tricalcium phosphate 3D scaffolds for bone tissue regeneration. Mater Sci Eng. 2012;32(5):1293–8. doi:10.1016/j.msec.2012.04.010.
36. Diogo GS, Gaspar VM, Serra IR, Fradique R, Correia IJ. Manufacture of β-TCP/alginate scaffolds through a Fab@home model for application in bone tissue engineering. Biofabrication. 2014;6(2):025001. doi:10.1088/1758-5082/6/2/025001.
37. Kang KH, Hockaday LA, Butcher JT. Quantitative optimization of solid freeform deposition of aqueous hydrogels. Biofabrication. 2013;5(3):035001.
38. Rezwan K, Chen QZ, Blaker JJ, Boccaccini AR. Biodegradable and bioactive porous polymer/inorganic composite scaffolds for bone tissue engineering. Biomaterials. 2006;27(18):3413–31. doi:10.1016/j.biomaterials.2006.01.039.
39. Choi D, Kumta PN. Mechano-chemical synthesis and characterization of nanostructured β-TCP powder. Mater Sci Eng C. 2007;27(3):377–81. doi:10.1016/j.msec.2006.05.035.
40. Andersen T, Strand BL, Formo K, Alsberg E, Christensen BE. Chapter 9 Alginates as biomaterials in tissue engineering. Carbohydrate chemistry, vol. 37. Cambridge: The Royal Society of Chemistry; 2012. p. 227–58.
41. Augst AD, Kong HJ, Mooney DJ. Alginate hydrogels as biomaterials. Macromol Biosci. 2006;6(8):623–33. doi:10.1002/mabi.200600069.
42. Bonino CA, Krebs MD, Saquing CD, Jeong SI, Shearer KL, Alsberg E, et al. Electrospinning alginate-based nanofibers: from blends to crosslinked low molecular weight alginate-only systems. Carbohydr Polym. 2011;85(1):111–9. doi:10.1016/j.carbpol.2011.02.002.
43. Valente JFA, Valente TAM, Alves P, Ferreira P, Silva A, Correia IJ. Alginate based scaffolds for bone tissue engineering. Mater Sci Eng C. 2012;32(8):2596–603. doi:10.1016/j.msec.2012.08.001.
44. Lima AC, Batista P, Valente TA, Silva AS, Correia IJ, Mano JF. Novel methodology based on biomimetic superhydrophobic substrates to immobilize cells and proteins in hydrogel spheres for applications in bone regeneration. Tissue Eng Part A. 2013;19(9–10):1175–87.
45. Li Z, Ramay HR, Hauch KD, Xiao D, Zhang M. Chitosan–alginate hybrid scaffolds for bone tissue engineering. Biomaterials. 2005;26(18):3919–28. doi:10.1016/j.biomaterials.2004.09.062.
46. Lin H-R, Yeh Y-J. Porous alginate/hydroxyapatite composite scaffolds for bone tissue engineering: preparation, characterization, and in vitro studies. J Biomed Mater Res, Part B. 2004;71B(1):52–65. doi:10.1002/jbm.b.30065.
47. Yang F, Xia S, Tan C, Zhang X. Preparation and evaluation of chitosan-calcium-gellan gum beads for controlled release of protein. Eur Food Res Technol. 2013;237(4):467–79. doi:10.1007/s00217-013-2021-y.
48. Torres AL, Gaspar VM, Serra IR, Diogo GS, Fradique R, Silva AP, et al. Bioactive polymeric–ceramic hybrid 3D scaffold for application in bone tissue regeneration. Mater Sci Eng C. 2013;33(7):4460–9. doi:10.1016/j.msec.2013.07.003.
49. Jiankang H, Dichen L, Yaxiong L, Bo Y, Bingheng L, Qin L. Fabrication and characterization of chitosan/gelatin porous scaffolds with predefined internal microstructures. Polymer. 2007;48(15):4578–88. doi:10.1016/j.polymer.2007.05.048.
50. Jeong SI, Jeon O, Krebs MD, Hill MC, Alsberg E. Biodegradable photo-crosslinked alginate nanofibre scaffolds with tuneable physical properties, cell adhesivity and growth factor release. Eur cells Mater. 2012;24:331–43.
51. Freed LE, Vunjak-Novakovic G, Biron RJ, Eagles DB, Lesnoy DC, Barlow SK, et al. Biodegradable polymer scaffolds for tissue engineering. Nat Biotechnol. 1994;12(7):689–93.
52. Kokubo T, Takadama H. How useful is SBF in predicting in vivo bone bioactivity? Biomaterials. 2006;27(15):2907–15. doi:10.1016/j.biomaterials.2006.01.017.
53. Jalota S, Bhaduri SB, Tas AC. Using a synthetic body fluid (SBF) solution of 27 mM HCO3 − to make bone substitutes more osteointegrative. Mater Sci Eng C. 2008;28(1):129–40. doi:10.1016/j.msec.2007.10.058.
54. Lee JTY, Chow KL. SEM sample preparation for cells on 3D scaffolds by freeze-drying and HMDS. Scanning. 2012;34(1):12–25. doi:10.1002/sca.20271.
55. Schieker M, Seitz H, Drosse I, Seitz S, Mutschler W. Biomaterials as scaffold for bone tissue engineering. Eur J Trauma. 2006;32(2):114–24. doi:10.1007/s00068-006-6047-8.
56. Lawson MA, Barralet JE, Wang L, Shelton RM, Triffitt JT. Adhesion and growth of bone marrow stromal cells on modified alginate hydrogels. Tissue Eng. 2004;10(9–10):1480–91. doi:10.1089/ten.2004.10.1480.
57. Dittrich R, Tomandl G, Despang F, Bernhardt A, Hanke T, Pompe W, et al. Scaffolds for hard tissue engineering by ionotropic gelation of alginate-influence of selected preparation parameters. J Am Ceram Soc. 2007;90(6):1703–8. doi:10.1111/j.1551-2916.2007.01598.x.
58. Rassis DK, Saguy IS, Nussinovitch A. Collapse, shrinkage and structural changes in dried alginate gels containing fillers. Food Hydrocoll. 2002;16(2):139–51. doi:10.1016/S0268-005X(01)00071-6.
59. Deligianni DD, Katsala ND, Koutsoukos PG, Missirlis YF. Effect of surface roughness of hydroxyapatite on human bone marrow cell adhesion, proliferation, differentiation and detachment strength. Biomaterials. 2000;22(1):87–96. doi:10.1016/S0142-9612(00)00174-5.
60. Rechendorff K, Hovgaard MB, Foss M, Zhdanov VP, Besenbacher F. Enhancement of protein adsorption induced by surface roughness. Langmuir. 2006;22(26):10885–8. doi:10.1021/la0621923.
61. Lawrie G, Keen I, Drew B, Chandler-Temple A, Rintoul L, Fredericks P, et al. Interactions between Alginate and chitosan biopolymers characterized using FTIR and XPS. Biomacromolecules. 2007;8(8):2533–41. doi:10.1021/bm070014y.
62. Daemi H, Barikani M. Synthesis and characterization of calcium alginate nanoparticles, sodium homopolymannuronate salt and its calcium nanoparticles. Sci Iran. 2012;19(6):2023–8. doi:10.1016/j.scient.2012.10.005.
63. Tzaphlidou M, Zaichick V. Calcium, Phosphorus, calcium-phosphorus ratio in rib bone of healthy humans. Biol Trace Elem Res. 2003;93(1–3):63–74. doi:10.1385/BTER:93:1-3:63.

64. Mansur HS, Costa HS. Nanostructured poly(vinyl alcohol)/bioactive glass and poly(vinyl alcohol)/chitosan/bioactive glass hybrid scaffolds for biomedical applications. Chem Eng J. 2008;137(1):72–83. doi:10.1016/j.cej.2007.09.036.
65. Wei G, Ma PX. Structure and properties of nano-hydroxyapatite/polymer composite scaffolds for bone tissue engineering. Biomaterials. 2004;25(19):4749–57. doi:10.1016/j.biomaterials.2003.12.005.
66. Román J, Cabañas MV, Peña J, Doadrio JC, Vallet-Regí M. An optimized β-tricalcium phosphate and agarose scaffold fabrication technique. J Biomed Mater Res, Part A. 2008;84A(1):99–107. doi:10.1002/jbm.a.31394.
67. Shi L, Shi L, Wang L, Duan Y, Lei W, Wang Z, et al. The improved biological performance of a novel low elastic modulus implant. PLoS ONE. 2013;8(2):e55015. doi:10.1371/journal.pone.0055015.
68. Tam SK, Dusseault J, Bilodeau S, Langlois G, Hallé J-P, Yahia LH. Factors influencing alginate gel biocompatibility. J Biomed Mater Res, Part A. 2011;98A(1):40–52. doi:10.1002/jbm.a.33047.
69. Hu Y, Wang J, Xing W, Cao L, Liu C. Surface-modified pliable PDLLA/PCL/β-TCP scaffolds as a promising delivery system for bone regeneration. J Appl Polym Sci. 2014;. doi:10.1002/app.40951.
70. Dowling DP, Miller IS, Ardhaoui M, Gallagher WM. Effect of surface wettability and topography on the adhesion of osteosarcoma cells on plasma-modified polystyrene. J Biomater Appl. 2011;26(3):327–47. doi:10.1177/0885328210372148.
71. Karageorgiou V, Kaplan D. Porosity of 3D biomaterial scaffolds and osteogenesis. Biomaterials. 2005;26(27):5474–91. doi:10.1016/j.biomaterials.2005.02.002.
72. Renders GAP, Mulder L, Van Ruijven LJ, Van Eijden TMGJ. Porosity of human mandibular condylar bone. J Anat. 2007;210(3):239–48. doi:10.1111/j.1469-7580.2007.00693.x.
73. Dumas JE, Prieto EM, Zienkiewicz KJ, Guda T, Wenke JC, Bible J, et al. Balancing the rates of new bone formation and polymer degradation enhances healing of weight-bearing allograft/polyurethane composites in rabbit femoral defects. Tissue Eng Part A. 2014;20(1–2):115–29. doi:10.1089/ten.TEA.2012.0762.
74. Kamitakahara M, Ohtsuki C, Miyazaki T. Review paper: behavior of ceramic biomaterials derived from tricalcium phosphate in physiological condition. J Biomater Appl. 2008;23(3):197–212. doi:10.1177/0885328208096798.
75. Franco J, Hunger P, Launey ME, Tomsia AP, Saiz E. Direct write assembly of calcium phosphate scaffolds using a water-based hydrogel. Acta Biomater. 2010;6(1):218–28. doi:10.1016/j.actbio.2009.06.031.
76. Yin Y, Ye F, Cui J, Zhang F, Li X, Yao K. Preparation and characterization of macroporous chitosan–gelatin/β-tricalcium phosphate composite scaffolds for bone tissue engineering. J Biomed Mater Res, Part A. 2003;67A(3):844–55. doi:10.1002/jbm.a.10153.